In situ transmission electron microscopy studies of mechanical properties of InAs nanowires

Master thesis
of
Marat Mukhametshin
from Ulyanovsk

at the Physics department
of the University Duisburg-Essen

March 2011

Contents

List of Abbreviations

AFM	Atomic force microscopy
FD-plot	Force-displacement plot
HR-TEM	High-resolution TEM
MOVPE	Metal-organic vapor phase epitaxy
NEMS	Nano-electromechanical systems
SEM	Scanning electron microscopy
SPM	Scanning probe microscopy
STM	Scanning tunnel microscopy
TEM	Transmission electron microscopy
VLS-technique	Vapor-liquid-solid technique
WZ	Wurtzite
ZB	Zink-blende

Abstract

Quasi-one-dimensional semiconductor nanostructures are very promising for future electronics and nanoelectromechanics. A wide range of methods was engineered for mechanical characterization of these structures like Atomic Force Microscopy (AFM) or nanoindentation. The characteristic elastic quantities have already been determined by several methods, such as electromechanical resonance and tensile stress testing. The "AFM-bending method" used in this work allows mechanical property measurement on an individual nanowires and simultaneous detailed atomic structure observation in transmission electron microscopy (TEM). This gives unique possibilities to study the correlation of mechanical properties of the nanowires with their atomic structure. In this work this method is used to obtain the Young's modulus of InAs nanowires grown by metal-organic vapour phase epitaxy (MOVPE) on bulk InAs (100)B substrate. It was found that there are three different types of the nanowires in the same sample. They have different growth direction and crystal and defect structure. Nanowires dispersed in solution were prealigned using dielectrophoresis to prepare a sample suitable for *in situ* AFM characterization combined with atomistic study in TEM. As a result, the Young's modulus for two types of nanowires (with $\langle 111\rangle$ growth direction and stacking faults perpendicular to the growth axis and with $\langle 121\rangle$ growth direction and stacking faults parallel to growth axis) were measured.

The nanowires with $\langle 121\rangle$ growth direction and stacking faults along the growth direction have a higher Young's modulus ($80\,GPa$ for $84\,nm$ wire and $109\,GPa$ for $55\,nm$ wire) then the one for bulk InAs ($73\,GPa$ in $\langle 112\rangle$ direction). The enhancement of Young's modulus can be explained by the presence of stacking faults. The maximum of Young's modulus is observed for wires of diameter around $50\,nm$ where the density of stacking faults is expected to be the highest. Electron diffraction was studied for loaded nanowires. A peculiar broadening of diffraction spots was observed. Based on the analysis of electron diffraction patterns recorded during the bending of nanowires at different loads, an atomistic model of wire deformation is discussed. Tensile and contractive strains leads to a radial broadening

of diffraction spots. Axial shifts of atoms which are non-uniform in radial direction in bent nanowire manifest themselves in angular broadening of diffraction spots.

It is shown that the results for nanowires with $\langle 111 \rangle$ growth direction are very sensitive to uncertainties in the diameter determination. One finds too large Young's modulus values (app. $600 - 1700\, GPa$) in comparison to the bulk value ($93\, GPa$ in $\langle 111 \rangle$ direction). Ideas of improve the experimental procedure are intensively discussed. Implying all recommendations established in this work one should be able to perform an experiment of high reliability and obtain Young's modulus values with a small error.

Abstrakt

Quasi-Eindimensionale Halbleiternanostrukturen sind vielversprechende Baumaterialien für zukünftige elektronische und nanoelektromechanische Bauelemente. Zahlreiche Methoden wurden für die mechanische Charakterisierung der Nanostrukturen entwickelt, z.B. Rasterkraftmikroskopie- (AFM) und Nanoindentation-basierte Methoden. Einige Methoden wie elektromechanische Resonanz oder Zugversuche wurden schon für die Analyse der charakteristischen elastischen Grössen eingesetzt. Die in dieser Arbeit verwendete "AFM-Biegemethode" ermöglicht die Messung der mechanischen Eigenschaften von einzelnen Nanodrähten mit gleichzeitiger Analyse in einem Transmissionselektronenmikroskop. Damit ist es möglich die mechanischen Eigenschaften von Nanostrukturen mit ihren atomaren Strukturen zu korrelieren. Die "AFM-Biegemethode" ist hier verwendet worden, um den Elastizitätsmodul mit Hilfe von metalorganischer Gasphasenepitaxie (MOVPE) auf dem volumenartigen InAs (100)B Substrat gezüchteten InAs Nanodrähten zu ermitteln. Dabei wurden drei unterschiedliche Typen von Nanodrähten auf derselber Probe gefunden. Diese sind von unterschiedlicher Wachstumsrichtung und atomarer Struktur. Mithilfe von Dielektrophorese wurden die in einer Lösung suspensierten Nanodrähte auf einem Substrat ausgerichtet, um sie für *in situ* AFM Messungen in Kombination mit TEM-Untersuchung zu präparieren. Diese Präparation ermöglichte es, dass der Elastizitätsmodul von zwei Typen der Nanodrähte (mit $\langle 111 \rangle$ Wachstumsrichtung, Stapelfehler normal zur Wachstumsrichtung und mit $\langle 112 \rangle$ Wachstumsrichtung, Stapelfehler parallel zur Wachstumsrichtung) gemessen werden konnten.

Die zuerste genannten Nanodrähte mit $\langle 111 \rangle$ Wachstumsrichtung und Stapelfehler normal zur Wachstumsrichtung besitzen einen grösseren Elastizitätsmodul ($80\,GPa$ für das Durchmesser $84\,nm$ und $109\,GPa$ für $55\,nm$ Durchmesser) im Vergleich zu volumenartigem InAs ($73\,GPa$ in Richtung $\langle 112 \rangle$). Die Steigerung des Elastizitätsmodules lässt sich durch die Präsenz der Stapelfehler erklären. Das Maximum des Elastizitätsmodules wird für Nanodrähte von einem Durchmesser von ca. $50\,nm$ beobachtet, für die maximale Stapelfehlerdichte erwartet wird. Elektronenbeugung wurde an den belasteten Nanodrähten durchgeführt, bei der eine unerwartete eige-

nartige Reflexenverbreiterung beobachtet wurde. Beruhend auf der Analyse des während der Nanodrahtenverbiegung aufgenommenen Beugungsdiagramms wurde ein atomistisches Model der Nanodrahtverformung berücksichtigt. Die Zug- und kontrahierende Dehnung führt zur radialen Verbreiterung der Beugungsreflexen. Die axialen Atomversetzungen, die ungleichförmig in radiale Richtung sind, tragen zur Reflexenverbreiterung bei.

Es wurde gezeigt, dass die Ergebnisse für die Nanodrähte mit $\langle 111 \rangle$ Wachstumsrichtung sehr empfindlich auf die Bestimmung des Durchmessers reagieren. Im Vergleich zum Volumenmaterial ($93\,GPa$ in Richtung $\langle 111 \rangle$) wurden enorme Elastizitätsmodule ($600 - 1700\,GPa$) ermittelt. Des Weiteren wurden Verbesserungen der experimentellen Methoden ausführlich diskutiert. Mit diesen Verbesserungen ist es möglich den Elastizitätsmodulus mit höher Genauigkeit.

1 Preface and motivation

Nanotechnology implicates the synthesis, study, and subsequent handling of nanoscale objects such as nanoparticles, nanowires, nanotubes, nanobelts etc. Semiconductor nanostructures hold much promise for future technology. Their peculiar physical properties, for instance such as stiffness different from bulk materials, or ballistic electron conductance, make them more useful in comparison with corresponding bulk material. The quasi-one-dimensional objects like nanowires instantly draw the attention due to their morphological distinction, namely they pervade in one dimension and are constrained in others. More important, these new building blocks with their specific properties open possibilities for the engineering of various devices: field-effect-transistors [13], logic gates [19][14], photodetectors, light-emitting diodes and lasers [36][14], NEMS [32], etc. The latter term transcribed as nano-electro-mechanical systems implicates further miniaturization of sensors, actuators, oscillators. Technological applications based on the nanostructures require the comprehensive understanding of their material parameters. For instance, the knowledge of mechanical parameters of nanostructures is needed for the implementation of NEMS.

Evaluation of characteristic mechanical quantities of nanoscale objects is often not a trivial challenge because of their dimensions. However, up to now a large number of experimental techniques was developed for this purpose [37], [16]. Thus, the mechanical testing of quasi-one-dimensional structures allows researchers to extract key mechanical properties, such as Young's modulus, bending and shear moduli. So far, the methods used for mechanical characterization of nanowires can be divided into two groups [37]:

1. Nanoindentation/AFM-testing. These methods imply the usage of stand-alone instruments. The nanoindenter instruments allow independent measuring of the load and the displacement. Depending on the feedback control, both load controlled and displacement controlled measurements are possible. By nanoindentation one measures mechanical properties directly. Thus, in case of nanowires, the indentation implicates the hardness measuring by indenting

the nanoindenter tip in the nanowire, which lies sidelong on the substrate [25]. The second technique of this type is atomic force microscopy (AFM). AFM, being originally designed for high-resolution topographical imaging of the surface, can be applied to the purpose of mechanical testing. The AFM-tip, placed on a piezo-driven cantilever, is pressed against the sample. The testing is possible in various modes: force microscopy mode, lateral force mode, contact mode. The deflections of the cantilever can be precisely measured for example by means of laser beam reflection. If the cantilever stiffness is known, its deflection gives the applied force, that may be further used to estimate the mechanical properties of the sample.

2. *In situ* electron microscopy techniques, are the next step forward of the foregoing family. These methods are the scanning-probe microscopy (SPM) techniques, such as AFM or scanning tunnel microscopy (STM), combined with scanning electron microscopy (SEM) or transmission electron microscopy (TEM). The great advantage of these techniques is the possibility of simultaneous sample imaging and performing a SPM-test. *In situ* SEM techniques provide mechanical testing on the nanoscale but without revealing the atomic structure of the sample. The problem of size limitation of samples and *in situ* mechanical testing setups is not essential in SEM. Hence, different *in situ* SEM setups were developed [37]. On the contrary, the operational space inside a TEM is limited typically by several millimeters but TEM allows atomically resolved imaging of the sample. In the recent years, however, commercialized solutions were developed, that are represented by specially designed sample holders [6]. These *in situ* TEM methods combine the inherent high spatial resolution of TEM with the potential of AFM (or STM) by virtue of miniaturized sensors [28], [6]. Thus, experimentators get unique possibility to study the correlation of mechanical properties of nanoobjects with their atomic structure.

   It is worthwhile noting, that there are also straightforward techniques, such as electromechanical resonance, which use electrostatic fields to excite vibrations of the sample *in situ* in SEM or TEM [27] to evaluate the mechanical properties of the sample.

By virtue of the *in situ* TEM techniques it is possible to study the quasi-one-dimensional nanostructures as models providing an insight into physical phenomena on the atomic scale. Planar defects, such as twinning boundaries, stacking faults, are typical inherent properties of nanostructures grown by particular methods [13].

For these reasons their influence on mechanical properties of the nanowires should be studied and understood. In this work InAs nanowires of two crystallographic orientations: $\langle 111\rangle$ and $\langle 121\rangle$, posessing twinning defects of different orientation with respect to the growth direction [26] were investigated. The dependence of Young's modulus on the diameter of wires and on the planar defects was previously noted for these structures [27],[24]. Up to now, however, it is not clear, whether the Young's modulus increases or decreases with the wire diameter, because of controversial results obtained by different groups [24],[27].

Last but not least, the morphology of the (1D)-structures is of importance for understanding the mechanical properties. For instance, revealing the three-dimensional shape of the nanowires by means of electron tomography [26] is required for better evaluation of the characteristic mechanical quantities. It is important to understand, how nanowires will response to applied forces. Thus, the lack of knowledge of the cross-section of the wire may cause the mistaken determination of the elasticity properties. These aspects were in the focus of attention during this study. The analysis of our AFM *in situ* TEM testing of InAs nanowires reinforced by structure determination by means of the electron diffraction and high resolution TEM (HR-TEM), may contribute to better understanding of the effect of atomic structure and particularly planar defects on elasticity of the nanowires.

I apply the AFM *in situ* in TEM technique to perform InAs NW bending with an AFM-tip. The applicability of this technique is another aspect of this work. Due to occurrence of significant error sources, there are still questions in the literature concerning the correct evaluation of the measured data [12]. The importance of this question must not be underestimated. The number of novel structures reported every year requires to be analyzed properly by means of reliable methods. In this work I discuss the advantages and drawbacks of our technique. Besides that, the ways for improvement of the technique will be pointed out.

2 Fundamentals

2.1 Transmission electron microscopy

Nowadays, TEM is a well-established indispensable instrument to characterize a structure of materials down to the atomic scale. The application field of TEM may be widely extended using a set of combined instruments and techniques. In this work, TEM analysis was used for the determination of the sample structure and for performing atomic force microscopy (AFM) experiments inside TEM. In this section, the fundamentals of TEM instrument will be explained in reference to only two basic modes of TEM: bright field imaging and electron diffraction, which I have used for structural and morphological characterization of my samples. Further information about TEM may be found, for example, in [2], [35].

2.1.1 TEM resolution

As it is clear from the name, this type of electron microscopy is associated with a beam of electrons, which passes through a sample to be analyzed. As they pass through the sample, electrons interact in different ways with atoms, resulting in elastic and inelastic scattering of electrons. Scattered electrons are deflected in a certain manner by means of an electron lens system, yielding a magnified image of the sample.

Let us estimate the resolution of the ideal TEM. Resolution of the optical instrument is defined as the minimal spacing between two points that can be distinguished. According to de Broglie theory, one can use the Rayleigh-criteria for the electron optics, which states for the resolution:

$$\delta = 0.61\frac{\lambda}{NA} = 0.61\frac{\lambda}{n\sin\beta}, \tag{2.1}$$

where NA is a numeric aperture of the lens system, calculated as the product of refraction index n of the medium (here vacuum) and sine of the semi-angle β. λ is the de Broglie wavelength of the electron:

$$\lambda = \frac{h}{p}, \tag{2.2}$$

where h is the Planck's constant and p is the electron impulse. As consistent with energy conservation one writes:

$$eU = \frac{m_0 v^2}{2}. \tag{2.3}$$

Here v and m_0 is the electron velocity and mass respectively, and U is the acceleration voltage. Hereafter the expansion of the electron impulse $p = m_0 v$ from above equation after transposition into the wavelength results:

$$\lambda = \frac{h}{\sqrt{2 m_0 e U}}. \tag{2.4}$$

Knowing that these electrons travel with relativistic velocities one should rewrite the equation 2.2 as followed [35]:

$$\lambda = \frac{h}{\sqrt{2 m_0 e U \left(1 + \frac{eU}{2 m_0 c^2}\right)}}, \tag{2.5}$$

where c is the speed of light. The estimation of the resolution gives $\delta \approx 1.3\,pm$ for the acceleration voltage $200\,kV$. Unfortunately, due to non-ideality of the electron optic the real achievable resolution of state-of-the-art instruments is about $0.08\,nm$.

2.1.2 TEM instrument and its operation modes

A simplified schematic drawing of TEM set-up with a ray diagram of the electron beam is shown in figure 2.1. The TEM-setup typically consists of illumination system, imaging formation system, and projection system. The illumination system is composed of an electron source, high voltage accelerator, and condenser lenses (not shown in schematic). Three types of cathodes: thermal tungsten tip, LaB_6 crystal emitter, and field emission gun (FEG), can be used as electron sources. First two types are used in older TEM instruments while FEG is used in modern ones. The functionality of two former electron sources is based on the fact, that

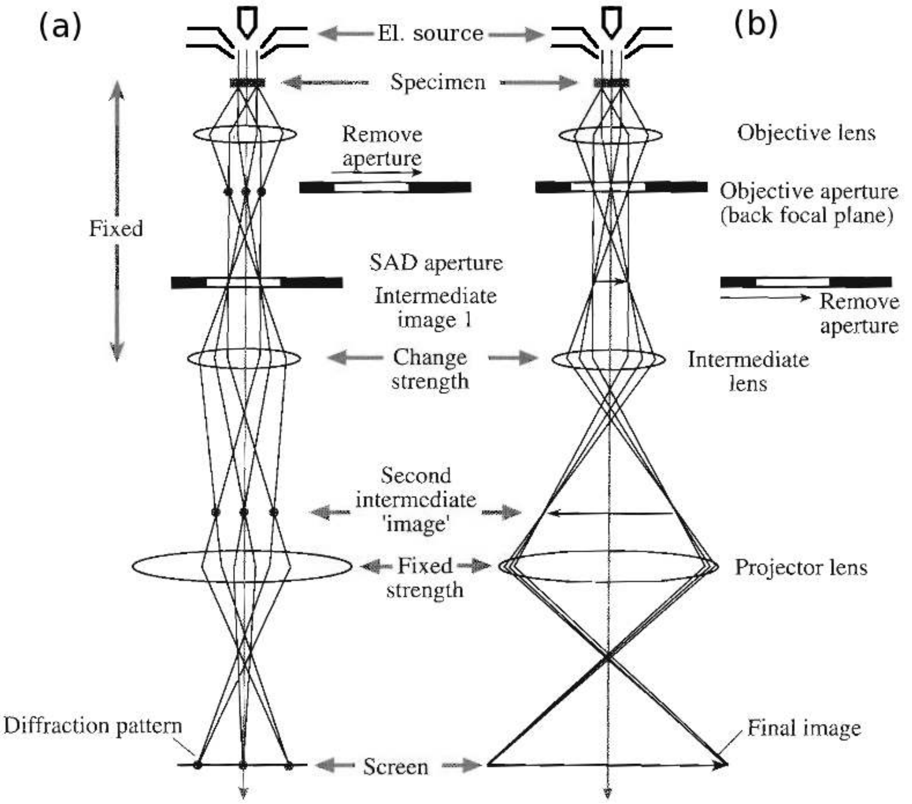

Figure 2.1: Schematic TEM setup. Electron paths are depicted by a ray diagram. The back focal plane of the objective lens coincides with front focal plane of the intermediate lens, that is the selected area diffraction configuration (a). The first image plane of the objective lens lies on the focal plane of the intermediate lens (b). This configuration is indicative for imaging mode. Adopted from [35] with modifications.

electrons are emitted out from a surface over energy barrier, when thermal energy of electrons overcomes work function of material (thermionic emission). For this kind of electron gun materials of low work function are used. The third type of electron source, FEG, relies on the extraction of electrons by using the effect of field emission with simultaneously slightly heating of the source. Under the extraction of electrodes one means the application of high potential between the source and electrodes of extraction system, so that the energy barrier on the filament (typically a tungsten needle with a sharp tip) is reduced. Due to the fact, that in this case the field emission but not thermionic emission is the dominant mechanism, this type of gun assembly is more stable, long-living, and, what is more important, the energy spread of electrons is narrow in comparison with hot filament gun. The emitted electrons are further accelerated by the high-voltage (typically several hundreds of kV) system of anodes. The accelerated high energy electrons propagate through series of condenser lenses, by which electron beams are formed. Changing the strength of condenser lenses governs the convergent angle of the beam, i.e. how is the sample illuminated with the electron beam. Thus, parallel or convergent electron beam can be obtained. The parallel illumination of the sample by electron beam is preferred for high resolution TEM (HR-TEM) while convergent electron beam is needed for scanning single points of the sample in scanning TEM (STEM) mode. It is worth to note, that there is also the set of apertures in each lens system, which is required to select beams, transpassing the lens system under spatial angle smaller then certain value (except the selected area aperture - see below).

The main part of imaging formation system is the objective lenses system. The incident electrons pass through a sample and further propagate through the objective lenses to form a diffraction pattern at the first back focus plane and an image at the image plane of the objective lens system. The system of objective lenses is the most important part of the imaging system, because it not only produces the first image of an object, but also determines the imaging quality and resolution limit. Though the electromagnet lenses are compact and easy to manipulate and maintain, the lenses imperfections (e.g. spherical and chromatic aberrations) limit the resolution and even produce distorted images. In optic lenses light can converge or diverse during propagation. Unlike them, the lenses in TEM are made of electromagnet by which electrons can only converge. In recent years, however, the aberration corrector has been invented, which is a big breakthrough in electron microscopy. The aberration corrector serves for elimination of magnetic lens imperfections. Modern TEM instruments equipped with such aberration correctors offer the possibility to observe atomic images with sub-angstrom resolution as well as signal to noise ratio is enhanced. By some cases, the quality of the image may be increased by using the objective aperture. By inserting it, the part of electrons, which are scattered under very wide angles, is excluded, yielding the image of better contrast.

After forming the first image and diffraction pattern of an object, the further magnified image up to million-times is done by series of lenses, namely lenses of projection system, which consists on an one intermediate lens and a group of projector lenses. Latter ones are used only to form the magnified intermediate image, produced by objective lens. The intermediate lens typically works in two regimes. Adjusting the strength of this lens we may enter into the first regime, when the lens is focused on the intermediate image and provides it further to the projector system, yielding the final image on the screen or on CCD-camera. This is the normal imaging mode, so-called bright-field (BF) imaging mode (see figure 2.1 (b)). The primary beam is used for the imaging in the bright-field mode in contrast to the dark-field (DF) mode, whereby some scattered beams are used. Though, the intermediate lens may be focused not on the first image plane (where the intermediate image is placed), but on the back focal plane of the objective lens. To understand the difference, refer to figure 2.1 (a). As shown in the ray diagram, the transmitted and scattered electrons are focused on the first back focal plane of objective lens. As the projection lens system provides only the magnification of the image, the diffraction pattern located in back focal plane is magnified and projected on the phosphor screen/CCD-camera. Thus, from the optical point of view the difference between diffraction and image modes is only in the fact, which optical plane is projected to the screen. So, if the sample is crystalline, the diffraction reflexes are observed. By means of selected area aperture, which is placed in the first image plane, one can select the specific beams of the diffraction forming image, coming out from the desired area of the sample. Thereby only the diffraction contributed by this desired part will be projected on the screen.

2.1.3 Structure characterization using electron diffraction

Electron diffraction techniques are often used to determine important crystallographic information of the examined sample, including lattice parameters, symmetry, crystallographic orientations in crystal and morphology. Medium-voltage electron diffraction in TEM is a rather complex physical process. Hence, a thoroughly complete description of underlying principles can be found in several textbooks [35], [15]. To account for the understanding and interpretation of electron diffraction data I present a simplified description of appearance of electron diffraction patterns in the framework of geometrically optical considerations.

Due to the wave-particle dual nature of electrons, their interaction can be treated either wave-like propagation-diffraction or particle-like deflection-scattering. Let us consider the wavefront of the plane electron wave diffracted on two points C and B (see figure 2.2 (b)). The distance between centers is equal to $d = BC$. Consider two corresponding wave propagation parameters: the wave vectors of incident $\vec{k}$ and scattering $\vec{k'}$, which are depicted in figure 2.2 (a). Wave vectors relate to each other as follows:

$$\vec{K} = \vec{k'} - \vec{k}, \tag{2.6}$$

where length of scattering vector $\vec{K}$ may be found from geometrical considerations:

$$|\vec{K}| = \frac{2\pi}{\lambda} 2 \sin\theta. \tag{2.7}$$

In the case of elastic scattering the energy of the electron does not change after scattering, i.e. $|k| = |k'| = \frac{2\pi}{\lambda}$. Consider the constructive interference of diffracted and transmitted waves. Let us apply the approach of Bragg reflection mentioned above. That implicates the treatment of beams behavior, as if incident beams are reflected from the atomic planes P_1 and P_2 of spacing d. The Bragg condition must be fulfilled for the constructive interference of reflected beams. In general case, the path difference of two rays R_1 and R_2 shown in figure 2.2 (b) is equal to $AC + CD$. In particular case, when scattering semi-angle θ is equal to Bragg angle θ_B, one can write the Bragg law:

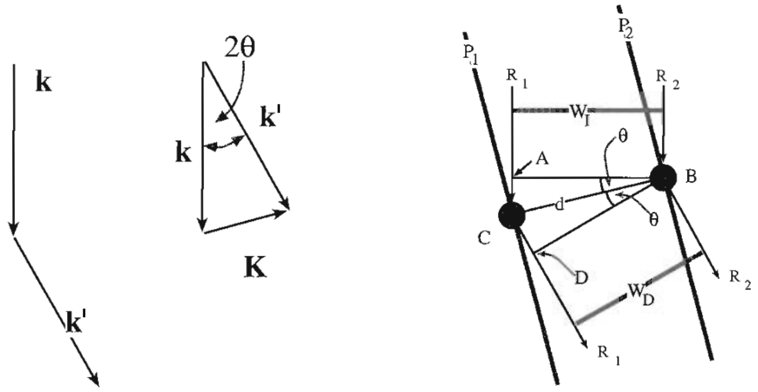

(a) (b)

Figure 2.2: (a) Incident $\vec{k}$ and scattered $\vec{k'}$ wave vectors, whose difference is a vector $\vec{K}$. (b) Schematic of scattering of two beams R_1 and R_2 on two points C and B. These points are lying in plains P_1 and P_2. Schematics were adopted from [35] with modifications.

$$2d \sin \theta_B = n\lambda, \tag{2.8}$$

where λ is the electron wavelength and n is an integer. Then, expanding this equation with the equation 2.7 and taking $n = 1$, one obtains, that at the Bragg condition the magnitude of the vector $\vec{K}$ is reciprocally related to the distance d between the planes:

$$|\vec{K}| = \frac{2\pi}{d} = |\vec{g}| \tag{2.9}$$

$$\vec{K} = \vec{g} \tag{2.10}$$

Thus, when vector $\vec{K}$ is equal to a reciprocal lattice vector $\vec{g}$, then the diffraction maxima emerge. This last equation is called Laue condition and it results in the occurence of Bragg reflection. One can show, that Laue condition is equivalent to Bragg condition. Laue condition is easy to understand by considering so-called Ewald construction. In reciprocal lattice space each point corresponds to the set of parallel atomic planes (hkl). One draws the incident and diffracted wave vectors $\vec{k}$ and $\vec{k'}$. The Ewald sphere is then defined as the sphere in reciprocal space with radius $\frac{2\pi}{\lambda}$, such that the vector $\vec{k}$ is a radius of the sphere and it ends on one origin of the reciprocal lattice. The section through the reciprocal space is shown in figure 2.3. Then, reciprocal lattice points which intersected by Ewald sphere will be recorded as diffraction spots, since geometrically the condition $\vec{k'} - \vec{k} = \vec{K} = \vec{R}$ is for these points fulfilled.

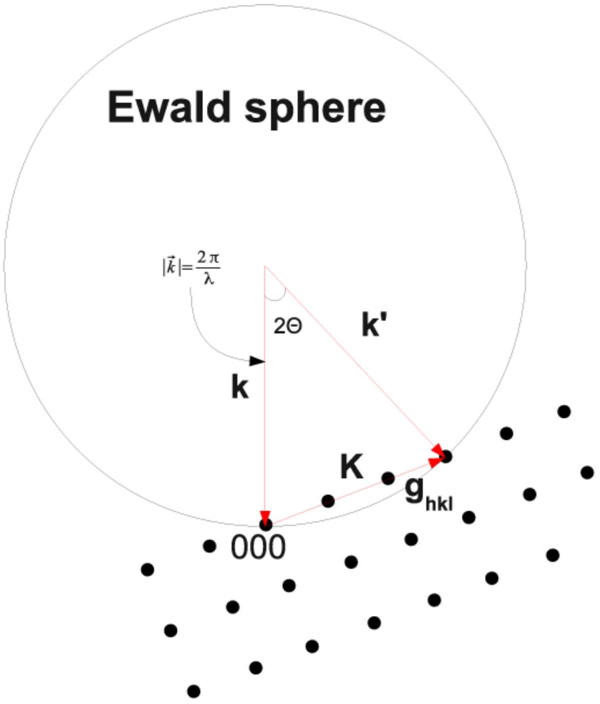

Figure 2.3: (a) Ewald sphere constructed on vector $\vec{k'}$ intersects a reciprocal lattice point, so that the Laue condition for $\vec{k'}$ is fulfilled and diffraction spot will be observed.

Considering the diffraction in real crystal, one should generalize the treatment to three-dimensional crystal lattice. Because TEM samples are normally thin (for instance, it should be $< 100\,nm$ thick for high-resolution TEM imaging), then the reciprocal lattice points extends in reciprocal space rods or relrods while in other two dimensions the sample is infinite resulting that the diffraction spot does not broaden in in other two directions. Therefore, even if the Bragg condition is not exactly fulfilled, crystal planes that are close to the Bragg condition will be still recorded on the diffraction pattern, since in that case not points but relrods from corresponding planes are intersected by Ewald sphere. Herewith the intensity of the reflex depends on the relrod intersection position. This can be described by the introduction of so-called excitation error $\vec{s}$, which is the distance between the current scattering vector $\vec{K}$ and the vector $\vec{g}$ of reciprocal space:

$$\vec{s} = \vec{K} - \vec{g}. \tag{2.11}$$

As the next step, one can associate each reflex (or diffraction spot) on the diffraction pattern to the specific crystallographic plane of the sample. Thus, the geometrical arrangement of diffraction reflexes gives the crystal structure whereas distances between peaks corresponds to the respective spacings between atomic planes in crystal. Let us consider the analysis procedure of electron diffraction pattern. We restrict ourselves in the case, when the crystal structure is already known or at least there is only few structure types. Since by my study of nanowires it is the case, this restriction is justifiable. Then the diffraction analysis algorithm consists in orientation of the sample so that the beam is parallel to low-index zone axis. The captured diffraction pattern is then compared with the standard ones.

Concerning the Laue condition 2.10 it is possible to rewrite it in terms of real space lattice vectors $\vec{a}$, $\vec{b}$, and $\vec{c}$:

$$\vec{K} \cdot \vec{a} = 2\pi h \tag{2.12}$$

$$\vec{K} \cdot \vec{b} = 2\pi k \tag{2.13}$$

$$\vec{K} \cdot \vec{c} = 2\pi l, \tag{2.14}$$

where h,k and l are integers, which define a crystallographic plane (hkl) .

An important issue in diffraction imaging is the calibration of the imaging system. The calibration is performed using a specimen with known lattice plane spacing d. Typically one uses polycrystalline Au thin film, so that the diffraction rings instead of spots is observed on this sample. The calibration consists in the calculation of camera length L value, the effective distance between the sample and the screen is given by:

$$d \cdot R = \lambda L, \tag{2.15}$$

where R is the distance between direct and diffracted beams on the screen, and λ is electron wavelength.

2.2 Atomic force microscopy (AFM)

In my work I use the contact atomic force microscopy (AFM) technique to perform the buckling tests. Let me briefly describe the contact AFM techniques in this section.

2.2.1 Principle of atomic force microscopy

The atomic force microscopy is based on the following straightforward principle. If one bring a body close to another, then they begin interact with each other due to arisen forces, such as van der Waals, electrostatic forces or other interatomic forces. This idea of AFM is to use the first body is a force sensor whereas the second body is a studied sample. The force sensor is represented by a cantilever beam fixed at one end and a sharp tip. If the AFM-tip is approaching the sample the superposition of the repulsive and attractive forces cause the cantilever to bend. For a small displacement in accordance with Hooke's law the restoring force exerted by the cantilever can be written as:

$$\vec{F} = -k\Delta x\vec{e}_x. \tag{2.16}$$

Here k is the spring constant of the cantilever and Δx is the displacement of the AFM-tip in the direction of the force vector. The force acting on the cantilever can be evaluated if the spring constant k is known. The requirement for high sensitivity imposes, that the cantilever should be soft. That means the spring constant should be small. The equation for the cantilever with rectangular cross section [33]:

$$k = \frac{Ewt^3}{4l^3} \tag{2.17}$$

shows, that in order to decrease k the length l cantilever should be much longer, than width, w and thickness, t. The second requirement regards the resonant frequency of the cantilever, which should be high enough (at least $> 10\,kHz$) to be insusceptible against low frequency mechanical vibrations. This requirement is fulfilled by the selection of light cantilever materials and miniaturization of the cantilever. Assuming the dimensions of the cantilever are in tens to hundreds micrometer whereas the material is silicon or silicon nitride, the spring constant is estimated to be several $N \cdot m^{-1}$, that allows atomic resolution studies [33]. The cantilever deflection or tip displacement in its turn may be detected by means of several methods. Most important among them are listed below.

1. Laser deflection method consists in the detection of the impinged laser beam from the rear side of the cantilever with a four-quadrant-detector. The laser beam reflects from the cantilever surface and directed to the four-quadrant-photodetector. If no force acts on the cantilever, the reflex spot points at the cross of quadrants, the signal at the photodetector is in that case balanced. If the cantilever is deformed, the reflected beam is deflected and the reflex spot in its turn moves out from the balanced condition, that can be observed.
2. Optical interferometry methods are based on detection of interference occurring between the cantilever rear side and cleaved end of the single-mode optical fiber, that is used to lighten the cantilever.
3. A piezoresistive detection method of cantilever deflection implements a piezoresistive element, which is embedded into the cantilever. The deformation of the cantilever during the AFM-test results in a change in resistivity of the piezoresistive element, which is included in an electronic detection circuit. The change of resistivity then is translated into the force. Due to its extremely compact design this displacement detection method is realized in AFM-sensor used in this work (see 3.2.2).
4. In a capacitance detection method the cantilever is used as one of two capacitor's plates. The bending of the cantilever is detected by the change of system capacitance.

2.2.2 Working modes

Relevant forces in the cantilever-tip/sample system are the long range forces, such as electrostatic and magnetic forces, and short range forces, such as van der Waals forces, adhesion, frictional forces, capillary forces. For the classification purpose the interaction potential of the system can be approximated with well-known Lennard-Jones potential, which is written as:

$$\phi(r) = 4\varepsilon \left(\frac{\sigma}{r}\right)^{12} - 2\left(\frac{\sigma}{r}\right)^{6}, \tag{2.18}$$

whereby the first term is the potential of repulsive field whereas the second term corresponds to the potential of attractive field. Here ε is the potential well depth,

σ is the corresponding distance between atoms, and r is the actual distance. The repulsive term can be derived by considering overlapping electron clouds of tip and sample atoms and hereafter applying the Pauli-Principe. The attractive term is derived from van der Waals interaction. The variety of AFM-techniques is then classified in three main types: non-contact mode, tapping mode, and contact mode. Figure 2.4 depicts Lennard-Jones potential versus spacing between two interacting atoms/molecules. Three regions denoted below the diagram correspond to classification into three different working modes: contact, tapping, and non-contact mode. Non-contact techniques are used to perform the scan over the surface of the sample with the tip. Thus, the topography of the surface may be obtained. According the name, the non-contact-AFM technique is characterized by such experiment geometry, when the AFM-tip does not touch each the sample during the scan or it just performs the tapping over the sample surface. The contact mode AFM is also mainly used for topography imaging, but besides that some non-imaging applications of contact mode AFM are important, such as mechanical probing used in this work or indentation-like experiments. Further description of topography imaging regimes is beyond the scope of this work, since the work was

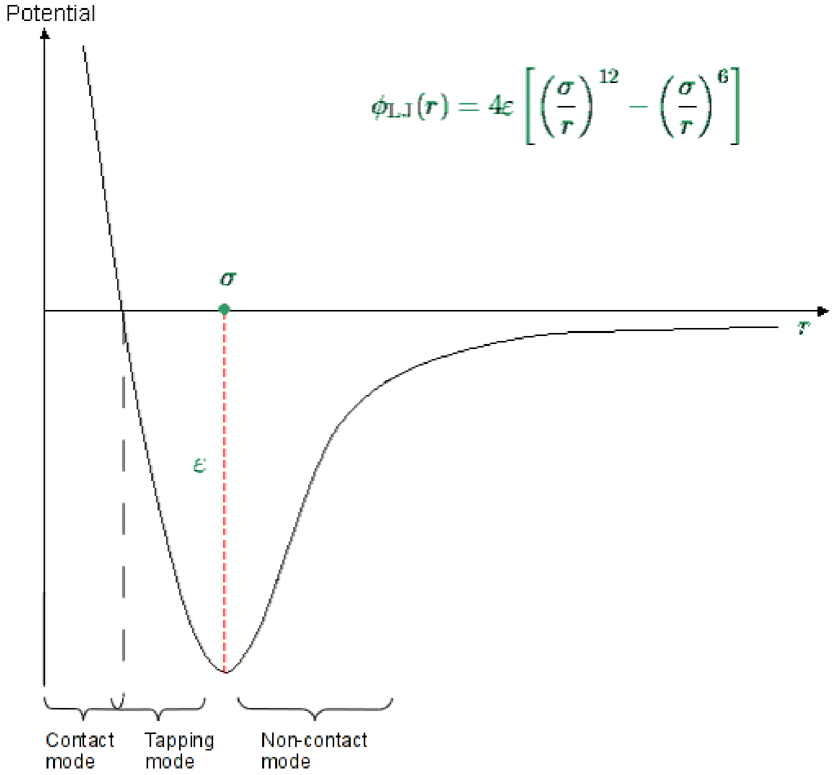

Figure 2.4: Lennard-Jones interaction potential as function of distance r between two atoms. Three operational modes: contact, tapping, and non-contact modes correspond to three regions on the diagram.

done only for contact mode by local mechanical probing with AFM. This technique is sometimes called force spectroscopy and consists of the determination, how the arisen force depends on the cantilever deflection. This deflection occurs during the mechanical testing of the sample with the AFM-tip in a particular location on the sample, yielding force-displacement plots. Experimentally, in this method one measures the cantilever deflection and consequently, the displacement of the tip as function of the sample movement. Assuming the linear dependence of the force on cantilever deflection, one can obtain this force.

2.2.3 Local force probe

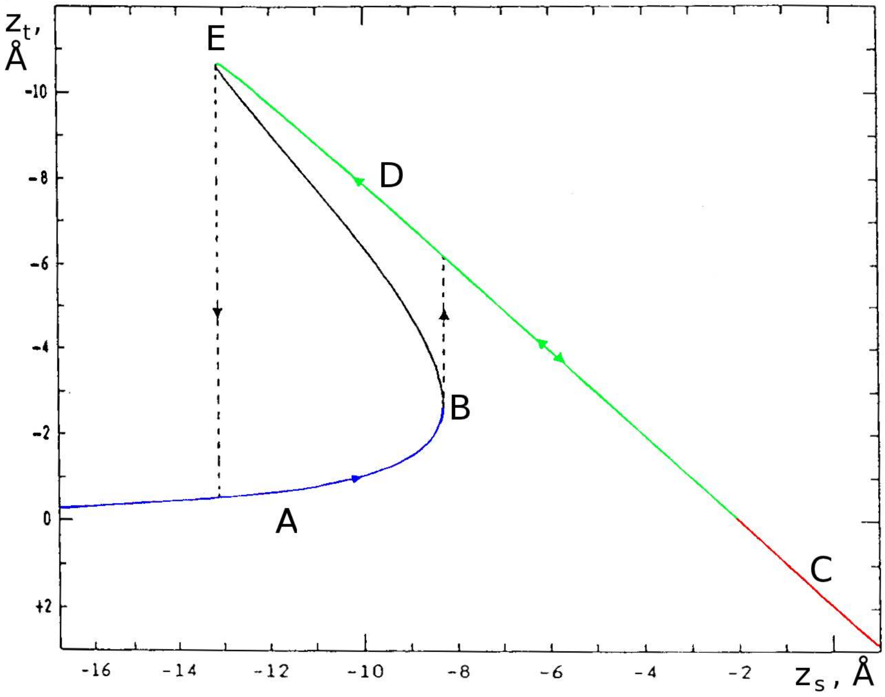

Figure 2.5: Simulation of the $z_t(z_s)$ plot, z_t is the tip displacement, which is plotted as function of sample movement z_s. Adopted from [33].

Let us consider, what happens as the AFM-tip approaches the sample surface. Figure 2.5 shows the simulation of the $z_t(z_s)$ dependence, i.e. the tip displacement z_t versus sample movement z_s. At the beginning, the AFM-tip and the sample are far away from each other. The interaction forces are negligibly small, resulting in zero displacement of the tip. By approaching the sample to the tip (region A, blue curve) the attractive force begins to act on the tip and the cantilever bends towards the sample surface. The gradient of the attractive force becomes equal to the spring constant of the cantilever at point B, therefore the jump to contact with the surface occurs. Further the pushing of the cantilever with the sample through cantilever zero position takes place (transition D → C). At point $z_t = 0$ the attractive force is substituted by the repulsive force (red curve). The tip-sample system in contact regime shows the linear dependence of the tip displacement on the sample displacement (region C, red line). Then one reverses the sample movement direction. At point of zero deflection (again by $z_t = 0$, transition C → D) the tip remains sticked to the sample due to adhesive force (green curve). As soon as the gradient of adhesive forces becomes equal to the spring constant (point E), the cantilever rips off from the contact.

An experimental plot $z_t(z_s)$ is shown in figure 2.6. On can clearly distinguish between the characteristic regimes and associate them with a simulated plot shown in figure 2.5. Knowing the cantilever spring constant k, it is possible to transform the $z_t(z_s)$ characteristic to the force-displacement plot (see the right Y-axis) according to the Hooke's law. The force-displacement plot contains a lot of information about the tip-sample interaction. Thus, the slopes of the curve may help by extraction of elastic properties of tip and sample. Points of instability which mean cantilever jump events, provide values of maximal adhesive (point E) and attractive force (point B). These forces are actual for this relative tip-sample configuration. As one can see, the experimental plot qualitatively differs the simulated ones. For instance, the main difference is, that the experimental plot possesses the pronounced hysteresis, which is missing in the simulated plot. The discussion of this and other features of experimental force-displacement plots in reference to this study will presented in sections Experiment and Discussion.

2.3 InAs structure and elastic properties

2.3.1 InAs bulk

As III-V semiconductor InAs is widely used in optoelectronic applications, and therefore its bulk properties are well studied. It crystallizes under normal conditions in the Zinc-blende structure. This structure is represented by two fcc (face-centered cubic) lattices (see figure 2.7) consisting of two different types of atoms. The lattices are displaced relative to each other by 1/4 of lattice diagonal along this diagonal. Thus, the structure is layered with one layer of group III atoms and the second layer of group V atoms. The stacking sequence for cubic Zinc-blende crystal structure is $ABCABC\ldots$

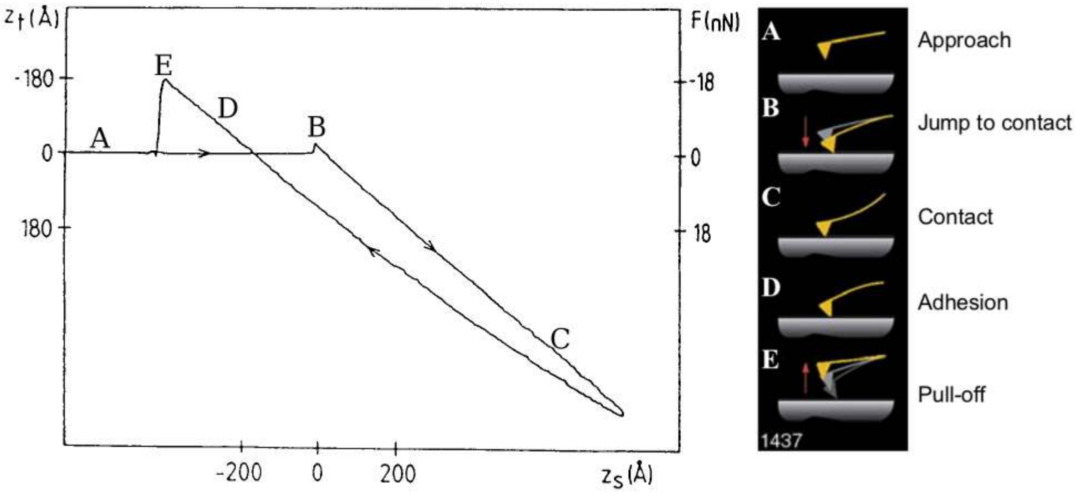

Figure 2.6: The experimental force-displacement plot obtained on a TaS_2 sample using a SiO_2 cantilever. Please mention the force axis is the right Y-axis. Different regimes are marked different regimes that undergo the cantilever-sample system by load-unload tests. The plot on the left hand is adopted from [33], the schematic of sample-tip geometry on the left hand is adopted from [8].

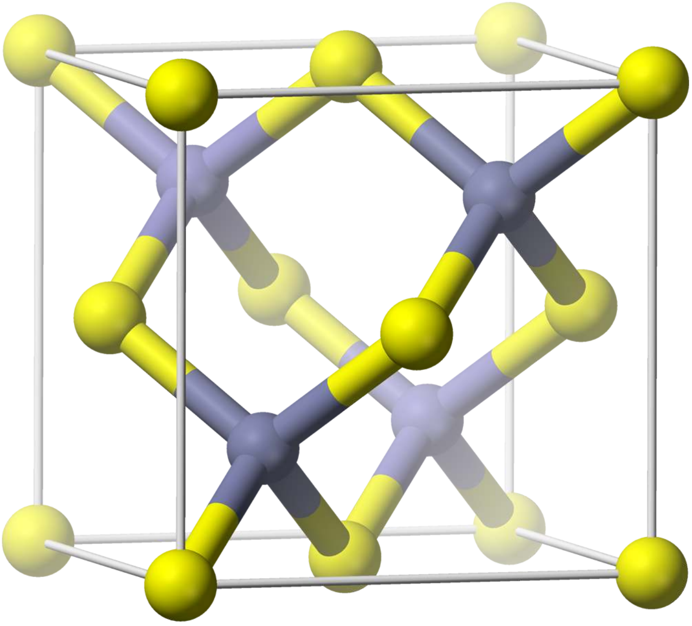

Figure 2.7: Schematic presentation of the Zink-blende crystal structure as a combination of two fcc lattices shifted along the cube diagonal by 1/4 of the diagonal length. Adopted from [4].

Evaluation of Young's modulus

Consider a bended nanowire of known cross section, with the curvature radius R. The elastic energy W of the bended nanowire can be written as following:

$$W = \frac{EI}{2} \int \frac{1}{R(z)^2} dz, \tag{2.19}$$

where E is the Young's modulus, I is the second moment of area, $R(z)$ is the local radius of curvature, and z is the location along the nanowire long axis. Let us assume, that R is the same over the whole nanowire length, i.e. the wire is in "global most-bend state" [9]. Then the equation for elastic energy W can be written as:

$$W = \pi \frac{EI}{R}. \tag{2.20}$$

The force per unit length acting in the most-bend state of the nanowire can be obtained as:

$$F/l = \frac{1}{s}\frac{dW}{dR} = \frac{EI}{2R^3}, \tag{2.21}$$

where $s = 2\pi R$ is the circumference of the wire. Finally, one can express the Young's modulus E as follows:

$$E = \frac{2R^3 F}{I \cdot l}. \tag{2.22}$$

The second moment of area I is defined as:

$$I = \int_A y^2 dA, \tag{2.23}$$

where A is the cross section of the nanowire perpendicular to its growth direction or to the nanowire long axis. The second moment of area is governed by the axis, around which the nanowire is bended. The quantity y is the distance from the axis to the element of area dA. In this study nanowires with circular and truncated triangle cross sections are investigated. For a circular cross section with radius a the second moment of area can be easy calculated in polar coordinates:

$$I_{circ} = \int_A y^2 dA = \int_0^{2\pi} \int_0^a r^3 \sin^2 \theta dr d\theta = \frac{\pi a^4}{4}, \tag{2.24}$$

For a truncated triangular cross section, however, the evaluation of I is more complicated. The value of the second moment has been obtained by V. Migunov *et al* in [27] by introducing a truncation ratio $r = \frac{AB}{AC}$ (see figure 2.8) and solving analytically the integral 2.23. For arbitrary truncation ratio r the second moment of area for the axis, which coincides with section AB in figure 2.8, can be found as:

$$I_{tr} = \frac{\sqrt{3}(2(1-r)^4 - r^4 - (1-2r)^4)d^4}{96(1-r)^4}, \tag{2.25}$$

where d is the nanowire cross-section width parameter denoted as BC in figure 2.8. For the InAs nanowires studied in this work the truncation ratio r is equal 0.2 as obtained from three-dimensional electron tomography [27].

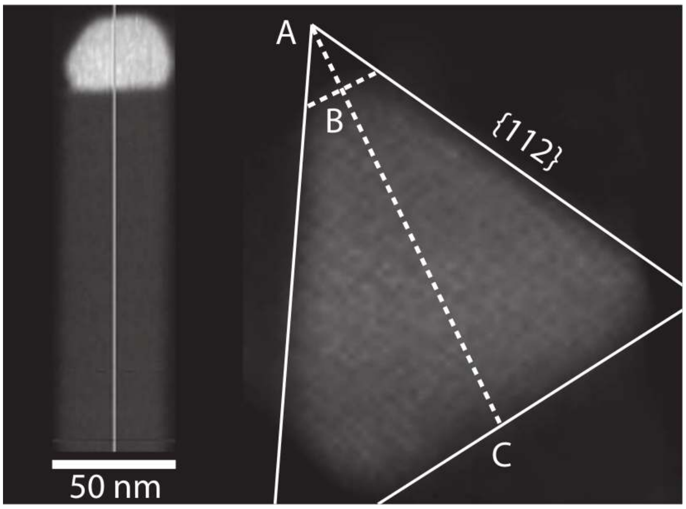

Figure 2.8: On the left hand: high angle annular dark field (HAADF) image of the nanowire recorded in scanning TEM mode. Bright particle on the top of nanowire is Au catalyst. The truncation ratio r is determined as the quotient $\frac{AB}{AC}$. The line AC coincide with the axis, around that the bending happens. On the right hand: cross-section of InAs nanowire with $\langle 111 \rangle$ growth direction as obtained from three-dimensional electron tomography in TEM. Adopted from [27].

2.3.2 InAs nanowires synthesis and properties

Let us then proceed to nanoscale dimensions, in particular quasi one-dimensional objects like nanowires. Here several issues become important. Reducing the object size from bulk to the nanosize, the ratio of volume atoms to surface atoms dramatically decreases. Therefore, the surface influence, which is neglected in the bulk case, becomes important at the nanoscale.

Another problem of nanoscale objects description is that the formation of planar defects during the objects synthesis can happen. Up to now there is no detailed theory explaining the defects formation. However, one distinguish three types of structure for the objects studied at this work. They will be represented after the description of synthesis of nanowires.

Metal-organic vapor-phase epitaxy (MOVPE) technique was used for InAs nanowires synthesis [13]. As it is clear from the acronym, the synthesis represents the epitaxial growth of structures on the specific substrate from the decomposited metal-organic precursors, and can be proceeded in several steps:

1. Bulk InAs with (001) crystallographic orientation is terminated with As atoms, denoted as InAs(001)B, was used for the nanowires growth. Colloidal Au-nanoparticles of app. $50\,nm$ diameter are dispersed on the substrate. Au nanoparticles are catalyst for the nanowire growth and their diameter determines the diameter of grown nanowires.

2. The substrate with deposited Au nanoparticles is placed into the low-pressure MOVPE set-up (see figure 2.9). Prior to the nanowire growth the substrate is annealed at $600\,°C$ under flow of TBAs (tertiarybutylarsin ($C_4H_9AsH_2$), group-V) and nitrogen over 10 minutes by melting down the Au particles and forming Au-In eutectic interface. The flow of TBAs during annealing is needed to reduce oxides at the substrate surface.

3. Growth occurs at the temperature to $400\,°C$ at constant flow of precursors and nitrogen over 8 minutes. Precursors TBAs and TMIn (trimethylindium ($In(CH_3)_3$), group-III) were supplied with a V/III ratio of 6.

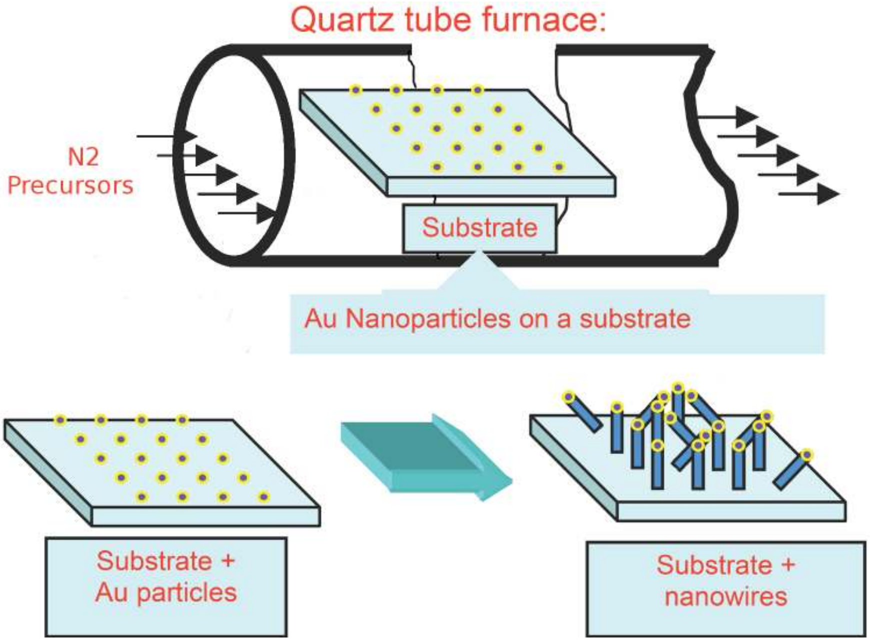

Figure 2.9: Scheme of MOVPE growth of InAs nanowires. At the top is the substrate inserted into the MOVPE set-up shown. The flow direction of precursors and N_2 is indicated with arrows. Bottom part shows the substrate before and after growth phase. Adopted with modifications from [34].

2.3.3 Structure of InAs nanowires

The SEM micrograph of the InAs substrate with grown nanowires is shown in figure 2.10 (a). It was shown [26], that 90 % of the nanowires are perpendicular to the substrate with their axes along $\langle 001 \rangle$ direction. 10 % of the nanowires grew inclined to the substrate (see figure 2.10 (b)). Following classification yields on the basis of detailed structural HR-TEM and SEM morphological studies [26]:

- Type I: nanowires with growth direction $\langle 001 \rangle$, oriented perpendicular to the substrate (001). Type I nanowires have cubic zink-blende structure without any planar defects.
- Type II nanowires: inclined to the substrate at angle 54.74 ° with respect to the substrate normal. For this nanowires the growth direction is $\langle 111 \rangle$. Dense $\{111\}$-twinning defects are observed in this structure. Twinning planes forming planar defects are perpendicular to the growth direction.
- Type III: nanowires are $\langle 112 \rangle$-oriented and inclined to the substrate at angle 35.26 °. The same $\{111\}$-twinning defects in this case are oriented parallel to the growth direction.

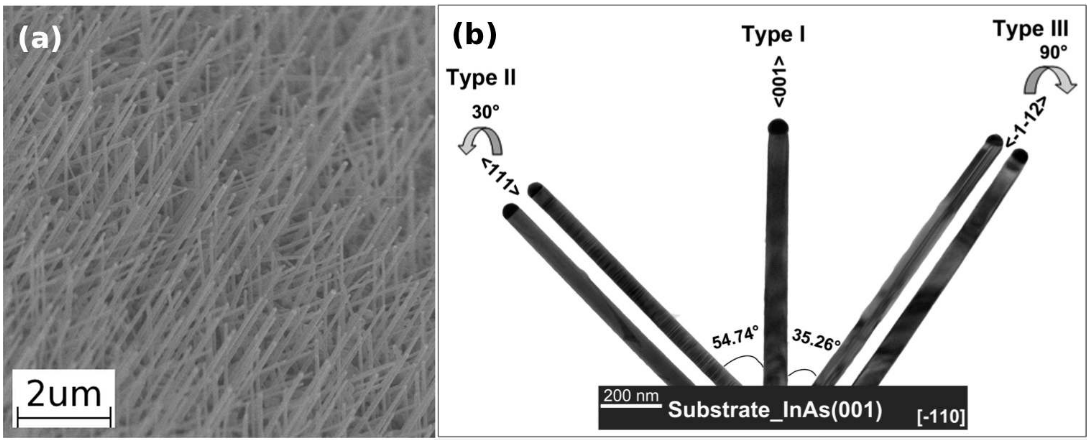

Figure 2.10: (a) SEM image of a part of the substrate with as grow nanowires. One clearly identifies three different inclinations of wires. (b) TEM images of selected nanowires combined relative to the InAs (001) substrate. This schematic illustrates classification of nanowires in three types according their growth direction. The growth directions as well as the inclination angle are shown for each type of wire. Figure (b) is adopted from [26]

For evaluation of Young's modulus by the proposed bending method, the knowledge of nanowire cross-section is required. For all three wire types the cross-section was determined by Zi-An Li *et al* [26] using 3D-electron tomography in TEM (see figure 2.11). On the cross-section images sidewall microfacets are shown as determined by the analysis of the diffraction patterns and the tomography images. Thus, type I wires have the distinct facets with {100} and {110} planes (a). Wires of type II have truncated triangle as a cross-section and six {112} distinct facets whereas typ III nanowires have approximately round cross section with no distinct facets. Figures 2.12 (d) and (e) schematically show an arrangement of planar defects in nanowires of type II and type III. The {111} twinning planes are schematically depicted on Type II and III nanowires perpendicular and along the growth direction, respectively.

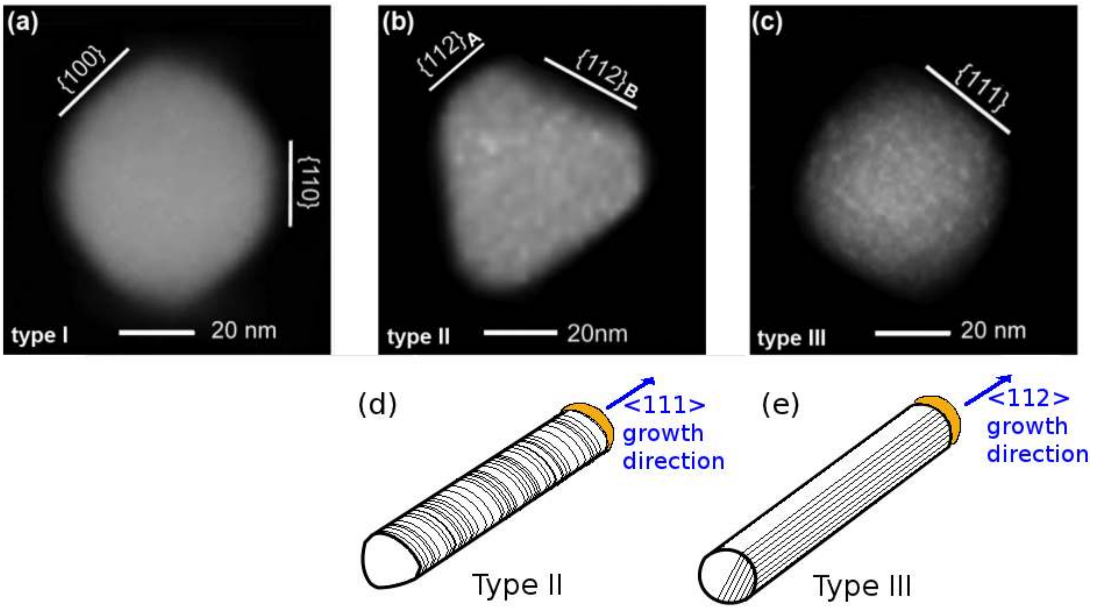

Figure 2.11: Cross-sections of three types of nanowires with marked microfacets: (a) Type I, (b) Type II, and (c) Type III. The arrangement of twinning defects in form of {111} twinning planes is schematically shown in (d) and (e) for defects containing nanowire types. Micrographs $(a) - (c)$ are made by Dr. Zi-An Li [26].

Planar defects observed in type II and type III nanowires represent the failure of stacking order in crystal structure. Planar defects observed in the studied nanowires are rotation twinning defects. These defects lead to remarkable coexistence of two crystal types in the same crystal. In our case that is the most common polytypes: Zink-blende (ZB) structure and Wurtzite (WZ) structure. The former is demonstrated in section 2.3.1. Both Zink-blende (which is based on fcc) and Wurtzite (based on hexagonal closed packing - hcp) are most densely packed. Thus, the potential energy difference of forming whether ZB or WZ type is usually small, allowing the formation of stable mixed structure at particular growth conditions [23]. To understand the difference between this two structures one takes a look on figure 2.12, which depicts two primitive hexagonal unit cells of Wurtzite (a) and Zink-blende (b) structures. Two different colors of circles denotes the different atom types: white corresponds to In whereas grey corresponds to As. The stacking order of Zink-blende is $ABCABC\ldots$ in the direction $\langle 111\rangle$. The WZ structure in the direction [0001] differs from ZB only in the third layer. The arrangement of this layer is identical to the A layer, so that the stacking order is $ABAB\ldots$ The stacking order along the [0001] (Wurtzite) and [111] (Zink-blende) directions are showin in figures 2.12 (c) and (d), respectively.

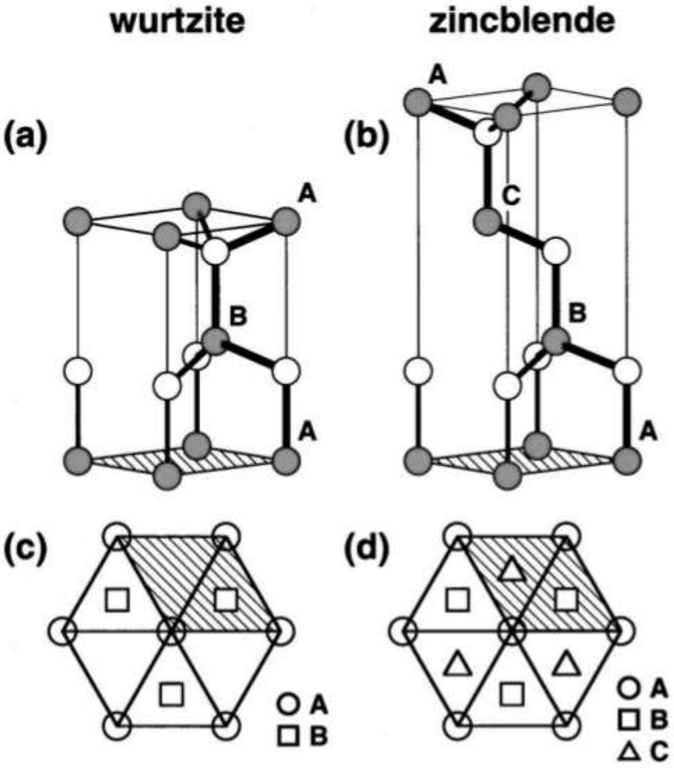

Figure 2.12: Crystal structure of Zink-blende (b) and Wurtzite (a) of InAs. In and As atoms shown in grey and white color or vice versa. The stacking order of planes in two structures is noted with "$ABA\ldots$" and "$ABC\ldots$" sequence, respectively. (c) and (d) shows the stacking order along the [0001] direction for Wurtzite and [111] direction for Zink-blende. Schematics adopted from [29].

Consider the appearance of the rotating twinning, which is common planar defect for typ II and typ III nanowires of our sample. Models of Zink-blende (a) and Wurtzite (b) structures are imaged so, that the image plane corresponds to the crystallographic plane (110). Different colors of circles denote different elements. The simple atomic model of the rotation twinning defect is shown in figure 2.13 (c). This planar defect can be described as the failure of stacking, whereby the segment of WZ denoted by CAC stacking order is built between ZB segments. Thus, the structure containing both ZB and WZ segments is formed. The rotating twinning defect owns its name due to geometrical considerations. Indeed, regarding the figure 2.13 (b), if one rotates the atomic arrangement around the axis [111] by $\pi/2$ at A plane, one obtains the twinning shown in (c). The HR-TEM image of Type II InAs nanowire along [110] zone-axis is shown in (d). One can note the specific zigzag-shaped contrast at the nanowire edge, which is formed by periodical repetition of ZB and WZ segments. It was shown for thin films of compound semiconductors [29] and, later, for nanowires [11], that one can control the density and even though the periodicity of defects by controling of growth conditions.

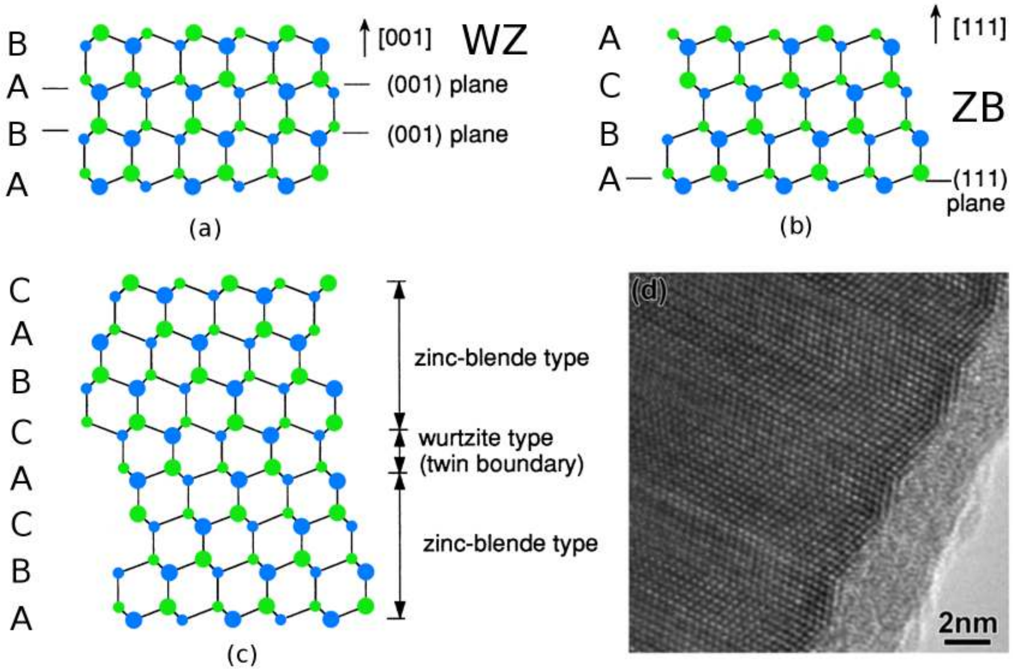

Figure 2.13: The simple atomic model of crystal structures. (a) Wurtzite structure, (b) Zink-blende structure, (c) Formation of twinning defect. The stacking layers are denoted by $ABCACBCA$. From the bottom here are four atomic layers denoted by $ABCA$ forming Zink-blende type. Then the layers CAC set up one Wurtzite segment. Further the $CBAC$ stacking sequence forms again three ZB segments. (d) HR-TEM image of InAs nanowire with [111] growth direction [26]. Schemes (a)-(c) were adopted from [23] with modifications.

3 Experiment

3.1 The alignment of nanowires by dielectrophoresis (DEP)

Contact atomic force microscopy (AFM) experiments in a transmission electron microscope (TEM) require a specific AFM-sample that consists of a supporting substrate with InAs nanowires to be studied, located on the substrate. Along with requirements for successful TEM-imaging on the one hand, the requirement to perform AFM-tests on the other hand are listed below:

- The sample has to be transparent for the electron beam. The examined nanowires are all transparent for the electron beam since their diameter typically does not exceed $100\,nm$. For the AFM measurement inside the TEM that means that either the nanowires should be deposited on a transparent substrate or a non-transparent substrate can be used but with specifically arranged nanowires. The latter case implies the next listed requirement.
- The nanowires have to stick out from the substrate edge in order to be imaged while the non-transparent substrate is being used.
- Since the AFM-tip is large comparable to nanowire size the distance between nanowires should be on the order of the AFM-tip dimensions, so that the neighboring nanowires do not hinder the AFM-test procedure.
- Nanowires have to be as parallel to the sample holder tilting axis as possible. In this case the chances to find the nanowires in the Bragg condition for the electron diffraction analysis are higher than for random orientation. Also the evaluation of AFM-test experiment requires such alignment of tested objects in order to simplify further calculation of material properties from the measured data.

The non-trivial challenge of sample preparation is solved by means of dielectrophoretic deposition. In this section I will present a brief description of dielectrophoresis in reference to sample preparation.

3.1.1 Dielectrophoretic force

To understand the dielectrophoretic alignment one should consider the basics of electromechanics of particles. Let us consider an electrical dipole. It consists of charges $+q$ and $-q$. The distance between charges is given by the vector $\vec{d}$, consequently the dipole moment can be written as $\vec{p} = q\vec{d}$. In an external homogeneous electrical field $\vec{E}$ the Coulomb force acts on the dipole resulting in a torque as depicted in figure 3.1 (a) [22]:

$$\vec{M} = \vec{p} \times \vec{E}. \tag{3.1}$$

Now one locates the same dipole in non-uniform electrical field as shown in figure 3.1 (b). In this case directions of acting forces on each charge slightly vary. The net force can be written as:

$$\vec{F} = q\vec{E}(\vec{r} + \vec{d}) - q\vec{E}(\vec{r}). \tag{3.2}$$

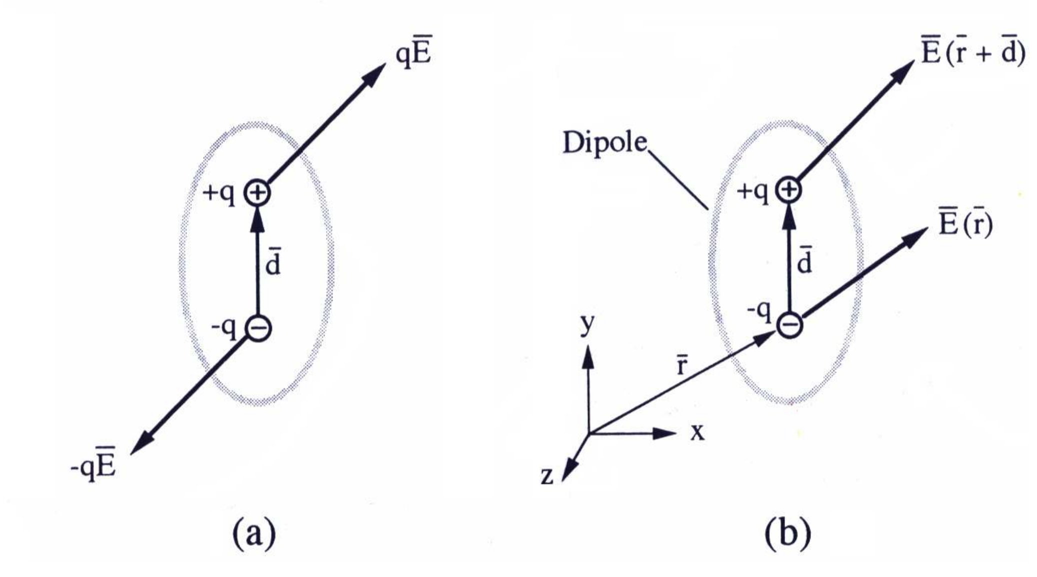

Figure 3.1: Two charges are conjugated in the dipole. (a) Torque induced by Coulomb force components; (b) Forces exerting on small dipole in the non-uniform electrical field. Schematics adopted from [22].

We assume the scale of non-uniformity of electrical field is larger than the size of the particle. In the case of dipole that means, that the field non-uniformity is larger than the length of vector $\vec{d}$. This is the so-called dielectrophoretic approximation

[22], which implies that the objects generating the electrical field (for instance, electrodes) are much larger than manipulated particles. This assumption is adequate in our case. We can expand the electric field $\vec{E}(\vec{r}+\vec{d})$ about position $\vec{r}$ in a Taylor series:

$$\vec{E}(\vec{r}+\vec{d}) = \vec{E} + \vec{d}\nabla\vec{E}(\vec{r}) + \frac{1}{2}\vec{d}^2\nabla^2\vec{E}(\vec{r}) + \ldots \tag{3.3}$$

Neglecting the terms of order larger than two and combining the equations 3.2 and 3.3 the force can be written as:

$$\vec{F} = q\vec{d}\nabla\vec{E} = \vec{p}\nabla\vec{E}, \tag{3.4}$$

As next step one proceeds to a dielectric spherical particle in the uniform electrostatic field. The particle is polarized in the external field, so the dipole moment is induced. To obtain the equation for the DEP-force on the particle one can use the simple way of so-called effective dipole method [22]. This method is based on the idea, that one can replace the particle with an infinitely small dipole, which generates the same electrostatic potential φ as the particle. Then, the dipole moment $\vec{p}_{eff}$ of the equivalent dipole is called effective. Understanding the origin of DEP-force requires us to use this method, which is not rigorous but very practical. Figure 3.2 shows the particle of radius R and dielectric permittivity ε_p depicted in a dielectric fluid of permittivity ε_m. One the one side the electrostatic potential of the particle at a position $\vec{r}$ is described by well-known equation:

$$\varphi = \frac{p_{eff}\cos\theta}{4\pi\varepsilon_m r^2}, \tag{3.5}$$

On the other side, one can determine the equations for the potential inside and outside the sphere:

$$\varphi_{in}(r,\theta) = -Br\cos\theta, r < R \tag{3.6}$$

$$\varphi_{out}(r,\theta) = -E_0 r\cos\theta + \frac{A\cos\theta}{r^2}, r > R. \tag{3.7}$$

Comparing the last equation for φ_{out} to the equation 3.5, one gets the equation for the effective dipole moment:

$$p_{eff} = 4\pi\varepsilon_m A. \tag{3.8}$$

The unknown coefficient A can be found combining two continuity conditions across the particle-medium boundary $(r = R, \theta)$ for electrostatic potential 3.6 and for the

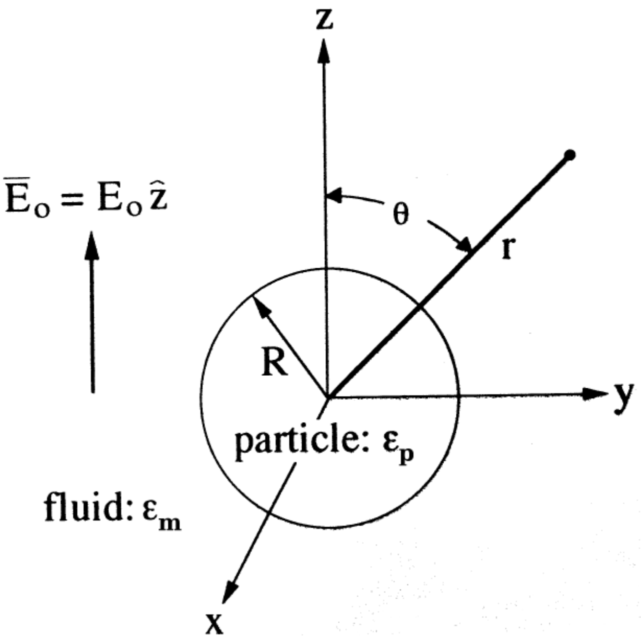

Figure 3.2: The spherical dielectric particle of radius R immersed in dielectric medium and placed in uniform electrical field $\vec{E}$. Dielectric permittivities of the particle and the medium are ε_p and ε_m, respectively. Adopted from [22].

normal component of the displacement flux vector. Then the coefficient A takes on the form:

$$A = \frac{\varepsilon_p - \varepsilon_m}{\varepsilon_p + 2\varepsilon_m} R^3 E_0. \tag{3.9}$$

Expansion of the last equation in the equation 3.8 yields:

$$p_{eff} = 4\pi\varepsilon_m f_{CM} R^3 E_0. \tag{3.10}$$

Here f_{CM} is so-called Clausius-Mossotti factor, which gives the strength of polarization as function of particle and medium permittivities:

$$f_{CM}(\varepsilon_m, \varepsilon_p) = \frac{\varepsilon_p - \varepsilon_m}{\varepsilon_p + 2\varepsilon_m}. \tag{3.11}$$

In the general case of an alternating electric field the Clausius-Mossotti factor is a function of complex permittivities $\epsilon_{m,p}$, which depends on medium and particle conductivities σ_m, σ_p. The field frequency ω can be described as:

$$\epsilon_{m,p} = \varepsilon_{m,p} + \frac{\sigma_{m,p}}{j\omega}, \tag{3.12}$$

where j is the unit imaginary number.

Staying in the framework of the effective dipole approximation, we can write the time-dependent DEP-force as:

$$\vec{F}_{DEP}(t) = \mathrm{Re}[\vec{p}_{eff}\exp(j\omega t)] \cdot \nabla\,\mathrm{Re}[\vec{E}\exp(j\omega t)] \tag{3.13}$$

Time averaging of this equation yields:

$$\langle \vec{F}_{DEP}(t) \rangle = \frac{1}{2}\mathrm{Re}[\vec{p}_{eff} \cdot \nabla \vec{E}^{*}]. \tag{3.14}$$

After expending this equation with equation 3.10 assuming complex quantities instead of scalars for f_{CM} and $\vec{p}_{eff}$ one has:

$$\langle \vec{F}_{DEP}(t) \rangle = g\varepsilon_m \mathrm{Re}[f_{CM}]\nabla E_{rms}^{2}, \tag{3.15}$$

where E_{rms} is a root-mean-square magnitude of AC electric field and g is the geometrical factor, which depends on volume and shape of the particle. For the spherical particle g is equal $2\pi R^3$. The DEP-force acting on the particle in the alternating electric field is then proportional to the geometrical factor g and the real part of Clausius-Mossotti factor $\mathrm{Re}[f_{CM}]$, that determines the force dependency on the field frequency. More important conclusion is that the DEP-force is proportional to the gradient of root-mean-square magnitude of electric field, i.e. the particle imposed in non-uniform electric field will be dislocated by DEP-force in the region of larger field for $\mathrm{Re}[f_{CM}] > 0$ suggesting so-called ”positive” DEP, or in the region of weaker field for $\mathrm{Re}[f_{CM}] < 0$ suggesting ”negative” DEP, respectively. In this study I use positive dielectrophoresis for the manipulation of nanowires forcing them into near parallel alignment between dielectrophoretic electrodes, that respond to electric field generation.

3.1.2 Setup for dielectrophoretic alignment

Fabrication of samples for AFM-TEM measurements was performed using home-made dielectophoresis setup. The setup is shown in figure 3.4. It consists of two micromanipulator stages placed on a table of an optical microscope Zeiss Axiotech. The first stage (ThorLabs, model MBT602) provides smooth movement of the top platform along three orthogonal axis as depicted in figure 3.3 (a). The spring design allows positioning of the top platform with a precision of around $0.5\,\mu m$ [3]. The second stage (OP Mount Instrument, model TRS-1) provides double tilting and rotation of the platform stage about axes corresponding to shift axes of XYZ-stage (see figure 3.3 (b)). Tilt and rotation angular resolutions are $\Delta\alpha_{tilt} = 15''$ and $\Delta\alpha_{rot} = 8''$, respectively [7]. Then the displacement resolutions of the tilt (for points on the stage edge, that are maximally outlying from the tilt axis) and rotation mechanisms at the edge of round stage platform of radius R are equal to:

$$R \cdot \Delta\alpha_{tilt} \approx 23\,mm \cdot 7.3 \cdot 10^{-5} \approx 1.7\,\mu m \tag{3.16}$$

$$R \cdot \Delta\alpha_{rot} \approx 23\,mm \cdot 3.9 \cdot 10^{-5} \approx 0.9\,\mu m. \tag{3.17}$$

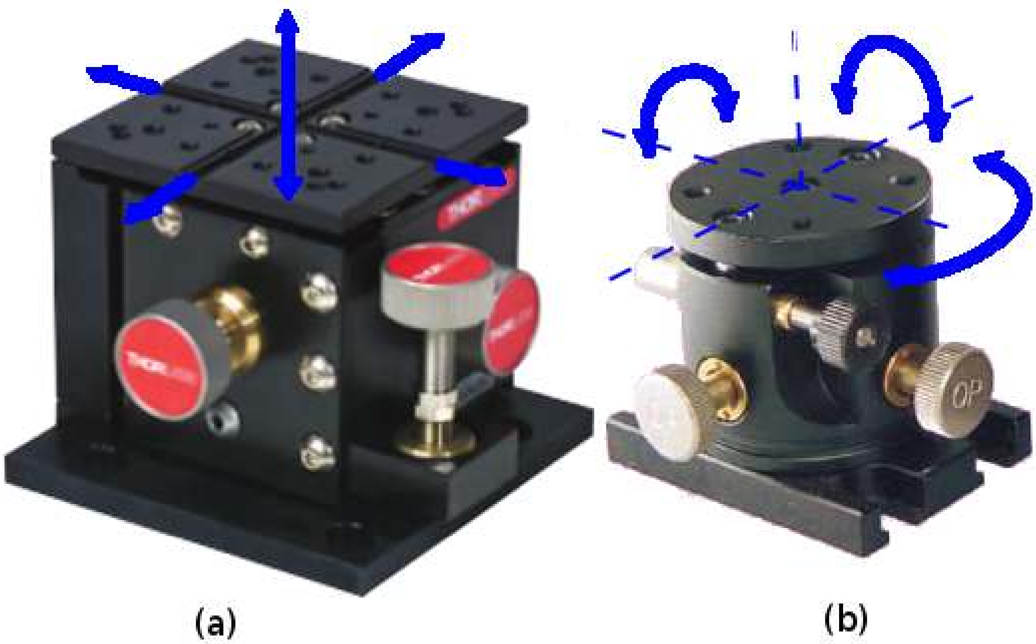

Figure 3.3: Commercial micrometer precise manipulation stages used to build the DEP set-up: (a) Three-axis micropositioning platform (ThorLabs MBT602). Blue arrows shows the possible directions of the top platform translation; (b) Double tilt and rotation stage (OP Mount Instrument TRS-1). The tilting and rotation directions of the top platform are shown with blue arrows as well as the tilt/rotation axes with blue dashed lines.

The dielectrophoretic electrodes can be manipulated with micrometer resolution. A pair of specially designed clamps (marked "5" in figure 3.4) is fastened on the micrometer stages. These clamps are manufactured of brass and designed to fix the 0.25 mm copper wire, that, in its turn, holds electrodes glued on to these wires. To fix the copper wire one should loosen the screw used to press on the clamping spring (see figure 3.6). After inserting the wire one tightens the screw until the wire is fixed. The special microscope table (marked "6" in figure 3.4) allows positioning of the system of two manipulators under the microscope objective. The clamps are electrically isolated from the micrometer stages by using plastic screws for fastening and thin isolation sheets between clamps and manipulator platforms. At the back the clamps are connected with wires to the low-voltage arbitrary waveform generator Keithley 3390 (marked with 2 in figure 3.4). It provides an alternating voltage of frequency up to $50\,MHz$ and a peak-to-peak voltage amplitude V_{p-p} up to $10\,V$ to generate the electrical field for the dielectrophoresis.

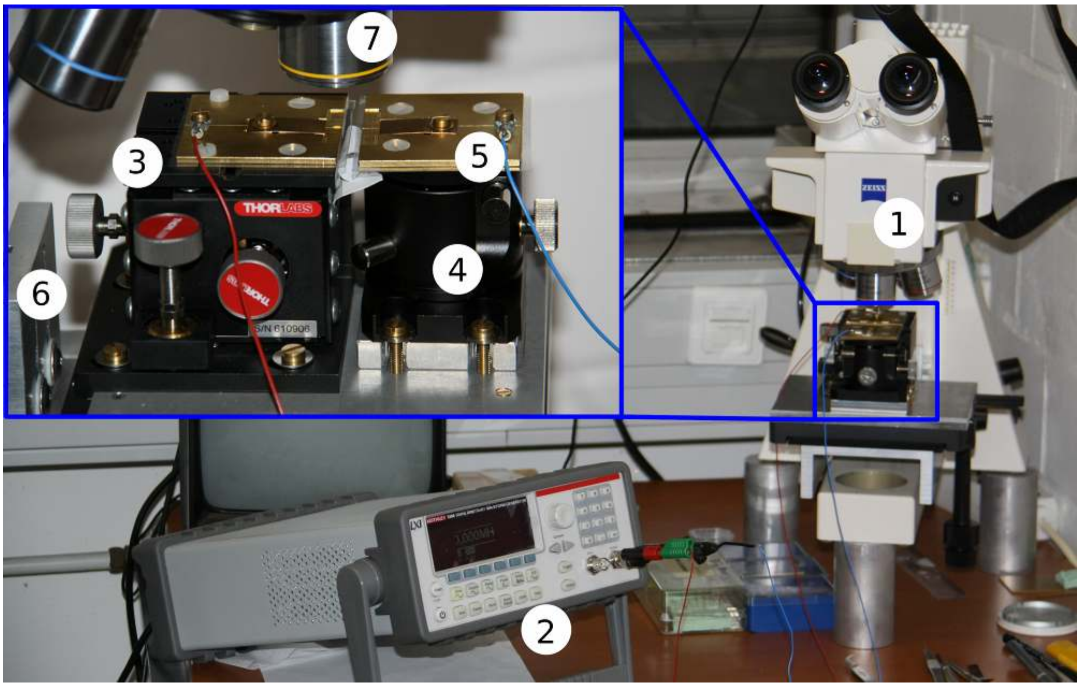

Figure 3.4: The home-made dielectrophoresis setup used for nanowires alignment. Inset shows the coupled micromanipulation stages. Marked components are: (1) Zeiss Axiotech optical microscope; (2) arbitrary waveform generator Keithley 3390 used to generate the alternating electric field between the electrodes; (3) three-axis micropositioning platform; (4) double tilt and rotation micropositioning stage; (5) clamping system for DEP-electrodes fixation; (6) microscope table featured with XYZ-positioning capabilities; (7) optical microscope objective.

3.1.3 Preparation of electrodes for the dielectrophoresis

A number of ideas were proposed for electrode preparation. Electrodes should satisfy the requirements given by DEP-method and partially by the AFM-testing procedure:

- Electrodes must be fine enough to generate the non-uniform fields.
- The grid design with a repeating pattern is preferable since the periodic arrangement of units with similar geometry gives rise to a similar local electrical field distribution. That allows to obtain the set of arranged nanowires on the whole edge of electrodes by means of just a single DEP-process.

- The preparation method should be fast and easy.

Based on these requirements a simple and effective method of electrode preparation was chosen. It implies the use of prefabricated commercially available standard TEM-grids as a blank.

Figure 3.6 (a) shows the photograph of the electrode arrangement on the clamping system. Each electrode consists of a piece of standard TEM grid glued to a Cu wire with diameter $0.25\,mm$. The Cu wire is used as support during dielectrophoresis, clamping, transportation and sample storage. Two component conductive epoxy is used for the cementing process.

To prepare the DEP-electrodes used in this work one needs a copper TEM-grid of the thickness $0.1\,mm$ and diameter $3.05\,mm$, a microscope slide and a one-sided razor blade. The TEM-grid is laid on the microscope slide and carefully cut in two parts with a razor blade under the optical microscope at low magnification. In order to satisfy the size requirements of AFM-TEM sample holder operational part and to facilitate further sample inserting and positioning, the width of the AFM-sample should be at least two times smaller than the width of the sample holder. The cutting scheme is shown in figure 3.5 (a). As the next step the $12\,mm$ long copper wire is compressed on one end to increase the interface area between the wire and the grid. Then a small drop of epoxy is applied to the plattened tip. One touches the bottom part of the grid with the end as depicted in figure 3.5 (b). Hereafter one lifts up the grid and if necessary visually adjusts the grid position, so that the wire axis which is parallel to the sample holder tilt axis is parallel to the working edge castellation elements and the wire is lying in the same plane as the grid. Hereafter the exposition of the DEP-electrode for $2-3$ hours on air is required in order for the epoxy to harden.

3.1.4 DEP: experimental procedure

The dielectrophoretic alignment is implemented by the following steps:

- Preparation of nanowires solution. The DEP implicates the usage of dielectric medium, typically deionized water or isopropanol. Nanostructures are often being transported and manipulated in solutions. Apparently, one can use the dispersion of nanowires in a solution both for transport and sample preparation.

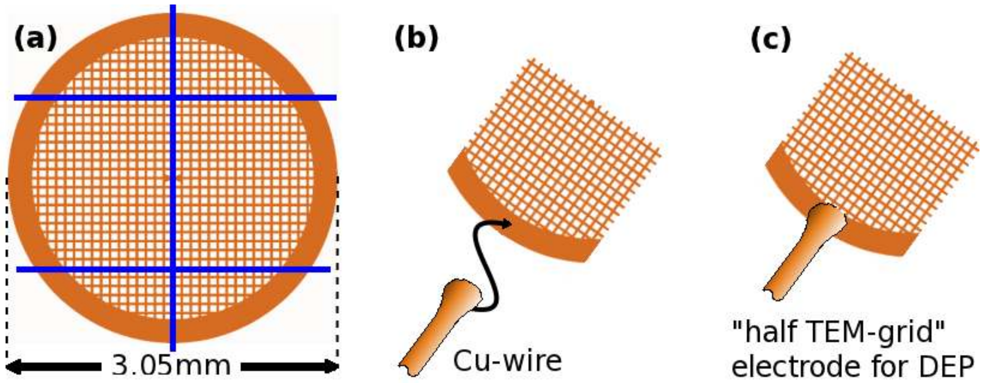

Figure 3.5: (a) Image of the TEM-grid cutting scheme. The cutting takes place across the blue lines. Grid showed is a 300-mesh pro inch standard TEM grid, which has been used in our experiments. (b-c) Scheme of grid attachment.

- Electrodes adjustment to each other. The position of the electrodes defines the distribution, local amplitude, and direction of the electric field.
- Adjustment of electric field parameters on the frequency synthesizer.
- Delivery of solution to the electrodes and switching on the electrical circuit.
- Control of the DEP-arrangement with optical microscope.

Preparation of the nanowires solution

To prepare the nanowires solution one cleaves the substrate with grown nanowires into pieces and takes the best of them. To find out, which part of substrate is the most appropriate one ought to precharacterize the whole substrate by SEM. Figure 3.7 presents SEM-images of different parts of the same substrate. Depending on local physical conditions during annealing and growth (temperature, precursors concentration, geometrical configuration causing for instance the local precursor flow shadowing etc.) the morphology of nanowires varies in different substrate parts. As one can see in figure 3.7 (a) the nanowires are of the same diameter over the whole nanowire length. Most of them have a similar length. One can identify all three available types of nanowires in the micrograph.

The nanowires shown in figures 3.7 (b), (c) and (d) are of more complicated morphology than the wires imaged in (a). The wires depicted in (b) have the form of long bended needles. The majority of nanowires in (c) and (d) exhibits the tapered morphology. Deviations from the simple morphology may complicate the further analysis.

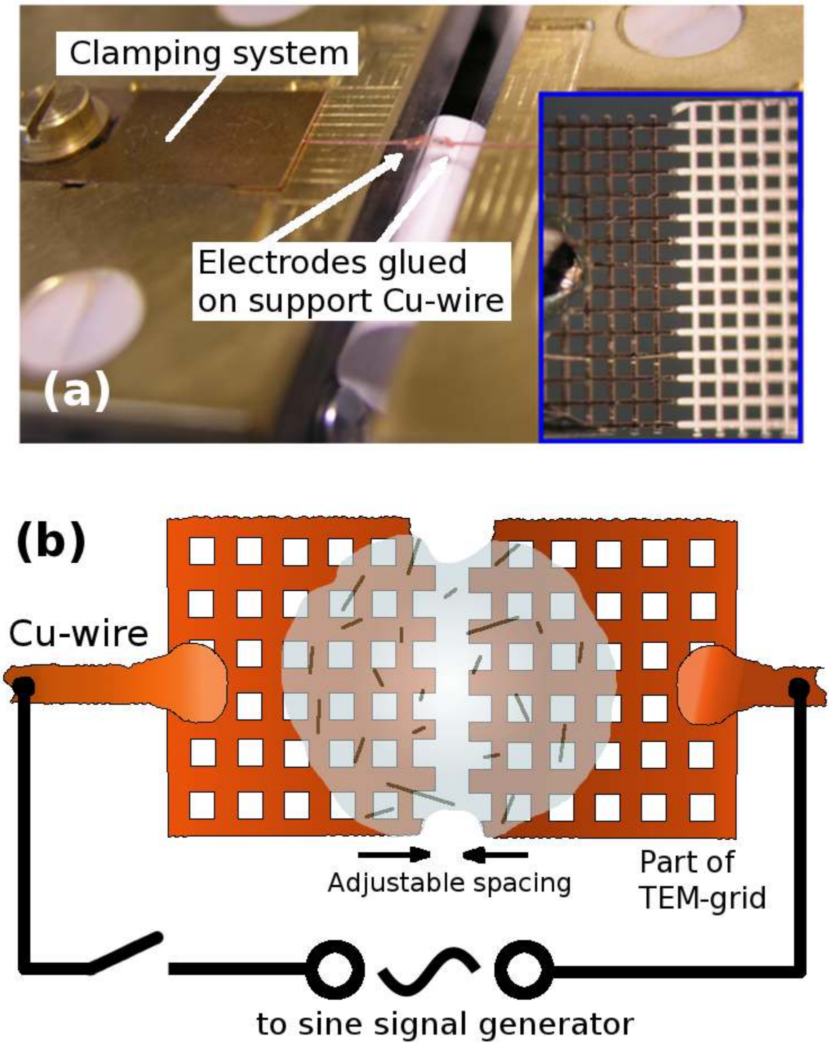

Figure 3.6: (a) Photograph of the clamping system with electrodes fixed on it. Inset shows the optical microscope photo of the electrodes arrangement. Electrodes are placed close to each other by using the micropositioning, so that the distance between them is of order $10\,\mu m$. Grid cell-to-cell distance is equal to $65\,\mu m$. (b) Scheme of the DEP-arrangement.

After choosing the appropriate substrate piece, one puts it in the clean chemical container with up to $5\,ml$ dielectric liquid. It is convenient to use the deionized water or isopropyl alcohol (IPA) not only as transport solvent but also as the dielectric medium for DEP. Then the container is placed into the ultrasonic bath for $5-30$ seconds to separate the nanowires from the substrate. For further processing the suspension must be diluted or an additional ultrasonic bath treatment may be required because of too high or too low nanowires concentration, respectively. To check whether the nanowires concentration is appropriate one puts a droplet of the suspension on the clean silicon substrate with a micropipette and observes the substrate in the optical microscope. The optimal value of the concentration is

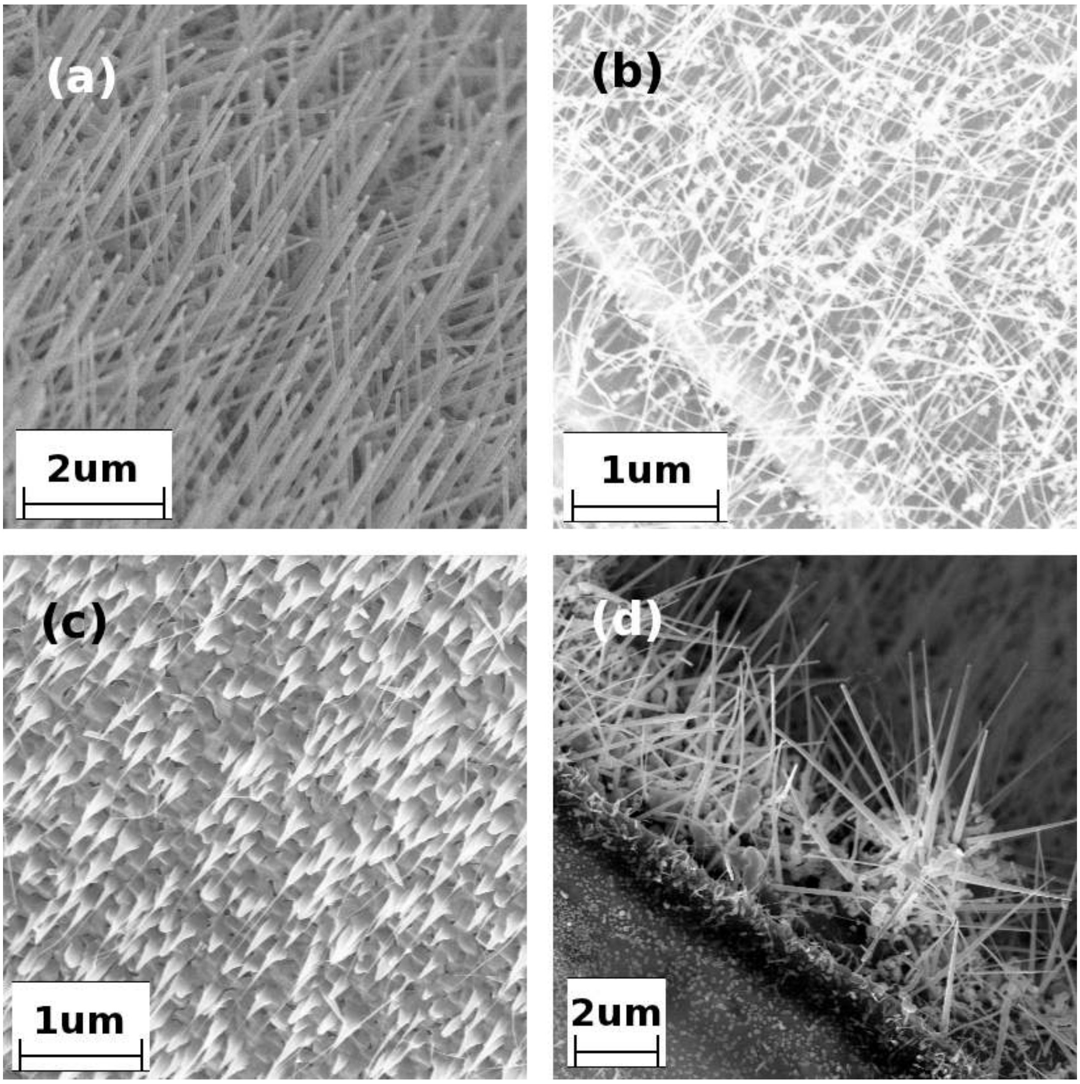

Figure 3.7: SEM-micrographs of different parts of the InAs substrate with grown InAs nanowires. For sample preparation it is preferably to use such parts of the substrate with morphologically appropriate nanowires, for instance the part depicted in (a).

found by try and error after multiple DEP tests and is about $(30-300)\times 10^{9}\,m^{-3}$. The length of nanowires typically does not exceed several micrometers.

Adjustment of electrodes and electrical field parameters

At this stage one adjusts the electrodes at a defined distance, typically $5-10\,\mu m$, from each other and the electrode edges are lying in the same plane. The positioning of the electrodes is carried out by the micrometer stages described in section 3.1.2. One of the electrodes is attached to the linear 3-axes stage whereas the second electrode is attached to the double tilt/rotation stage. It is equivalent to the configuration where the first electrode would be fixed stationary, but the second one could move around six degrees of freedom providing outstanding flexibility of positioning. The adjustment is proceeded simultaneously with observing the electrode area in the optical microscope. Unfortunately, one faces a problem during the adjustment of the tilt/rotation stage. This stage is designed so that the tilt axes are lying in the plane of upper surface of the stage platform whereas the clamping system situated several millimeters above the platform. Since the electrodes are not directly attached to the stage platform but by virtue of the clamping system, the tilting of the platform induces the additional undesirable rotational dislocation of the second electrode about the tilting axis. This effect should be compensated with adjustments of other stage and therefore may complicate the whole procedure. For this reason the fixing of electrodes in the clamping system should involve prealignment of electrodes by eye.

The occurrence of additional effects listed below during the dielectrophoretic alignment procedure may complicate the determination of required conditions. The total force acting on the single nanowire during DEP can be found as the sum of variety of forces, which act due to various effects:

- Brownian motion and gravity [18]. Considering the colloidal dynamics this effect can be neglected, if the observation period is long since the average of force associated with Brownian motion is zero. The second effect specified by the acting of buoyancy force is also negligible for nanometer-scale objects assuming, that one deals with freshly prepared solution.

- Electrohydrodynamical effects, generation of fluid flow due to the applied alternating voltage [18]. Dissipation of the electric power $W = \sigma_m E^2 (Wm^{-3})$ occurs in the solution due to its finite conductivity σ_m. The power dissipation gives rise to local heating and the temperature gradient produces gradients in conductivity, density and dielectric permittivity [30]. The natural convection due to density gradient forms the fluid flow which drags nanowires. On the other hand the permittivity gradient gives rise to the dielectric force whilst the conductivity gradient generates free volume charge and the Couloumb force respectively. Besides that another effect called AC electro-osmosis may give rise to the fluid flow [18],[30], [10].

For these reasons the optimizing of DEP parameters (alternating voltage frequency, electrode distance, peak-to-peak voltage) is necessary so that the dielectrophoretic force dominates over others. The dependence of the yield of aligned nanowires on the DEP parameters was studied by Raychaudhuri *et al* [31]. It was found, that for electrodes geometry described in the article the optimal distance between electrodes is $10\,\mu m$, the optimal alternating voltage frequency for InAs nanowires and deionized water as medium is $1\,MHz$ and peak-to-peak voltage is $5\,V$. Their electrode geometry is represented by $1\,\mu m$ width finger-like arrays, and either 20 or $45\,\mu m$ length fingers. Since the local roughness of the electrode edge in our studies is on the order of several micrometers it is reasonable to use the DEP parameters of [31].

The procedure of dielectrophoretic alignment

To start the dielectrophoretic alignment one takes about $1-3\,\mu l$ of the nanowires suspension with a micropipette and carefully applies it from above to the preliminary adjusted electrodes. Hereafter one turns on the generator output thereby starting the dielectrophoretic alignment. The alignment procedure can be observed in the optical microscope, when nanowires appear of nanowires between the electrodes. After drying of the drop the electrodes with aligned nanowires may be used as AFM-samples.

During the DEP the bridging as well as non-bridging of electrodes by the wires may occur. The deposited nanowires tend not to be swept away by blowing off the solution drop [31]. The reason of the stability of nanowires after deposition is adhesion forces between the electrode and nanowires. In our studies we confirm that the wires which deposit with the electrode bridging are hardly affected by the surface tension forces whereas the majority of nanowires, which are not bridging, are swept away during the drying. Thus, the bridging of the alignment gap improves the yield of aligned wires.

The DEP method slightly differs depending on the solution medium. If one uses the deionized water as the solvent medium one should focus on the complete coverage of the zone between the electrodes with the suspension since its high surface tension ($72.8\,mN/m$ at $20\,°C$ [1]) tends to contract the droplet to a sphere. For this reason one may use the isopropyl alcohol as the solution medium; offering a smaller surface tension ($21.4\,mN/m$ at $20\,°C$ [1]) isopropanol completely covers the surface of electrodes. Another advantage of the solution with low surface tension is the following. The lower the surface tension is, the smaller is the undesirable force, acting on deposited nanowires and attempting to sweep the nanowires away during the drying of the solution. Isopropanol with its lower surface tension is preferable in this case. However, we did not notice any significant differences in DEP results when using either isopropanol or water.

3.1.5 DEP results

Figures 3.8 (a) and (b) show optical microscope photographs of aligned nanowires lying on the electrode edge after DEP. On the top one can see the electrode, which imaged edge appears blurred. Despite that one can clearly observe the aligned nanowires sticking out of the electrode edge. The field distribution is highly dependent on the local geometry of the electrode edges. Hence the possible non-uniformity of the electric field may influence the alignment of wires in such a way, that they deposit not exactly parallel to each other. Since the top edge of the electrodes is generally rough, nanowires deposited on these roughnesses appear in photograph, as they are positioned on various hight. Nanowires may deposit not only on the top edge of the electrode but also on to any roughnesses. **Indeed, the optical micrograph 3.8 (b) shows the same part of the electrode but with the focus is slightly altered. Now the nanowires which was in the focus at the photograph (a) are not visible whereas other nanowires are in focus now.** Another example of the aligned nanowires is shown in figure 3.9.

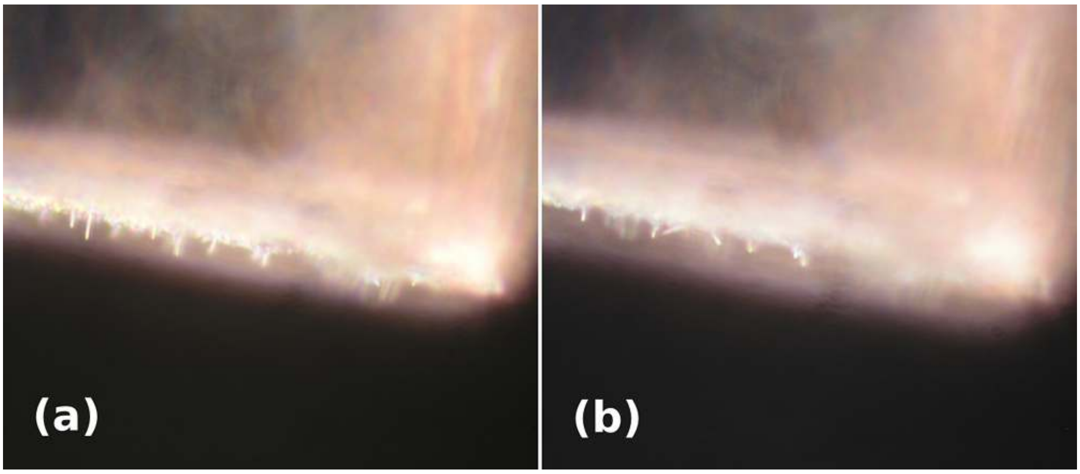

Figure 3.8: An optical microscope image (a) of the electrode after DEP procedure. Aligned nanowires are mostly **nearly** parallel to each other. The image (b) shows the same electrode but the focus is slightly changed. The second electrode is not visible since it was moved away to eliminate its blurring ”halo”.

On this TEM image one can distinguish the electrode edge at the top left part of the image and three aligned nanowires which projections are nearly parallel to each other.

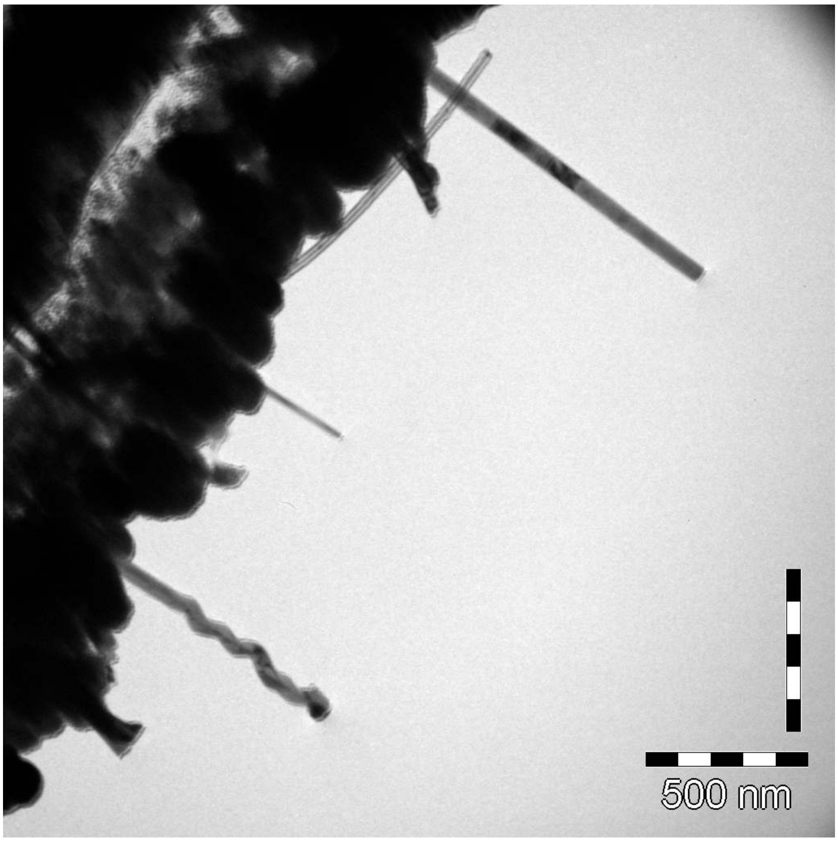

Figure 3.9: TEM image of aligned InAs nanowires.

3.2 AFM in situ TEM experiments

3.2.1 AFM-TEM sample holder

In this work I used a commercially available AFM-TEM sample holder from Nanofactory Instruments [6]. The AFM-technique implies a use of AFM-sensor, which must satisfy very strict size tolerance to be integrated into the tiny dimensioned operational space of the conventional TEM sample holder.

The design of the AFM-TEM sample holder is based on the modification of a conventional single-tilt holder, as shown in figure 3.10. The signal pre-amplifier and cable interface are positioned on the left side while the holder body carries the signal wires. The gap width between poles does not exceed $1-2.5\,mm$. That impose heavy demands on the size of tip part of the holder. As one can see from schematic view of the operational area at the holder tip (see figure 3.10 (b)) the AFM-sensor is fixed whereas the sample is movable. The sample is attached to the hat holder, that is put on the metal bar, which is welded to piezotube front edge. The coarse movement of the sample is controlled by the positioning system based on piezotube,

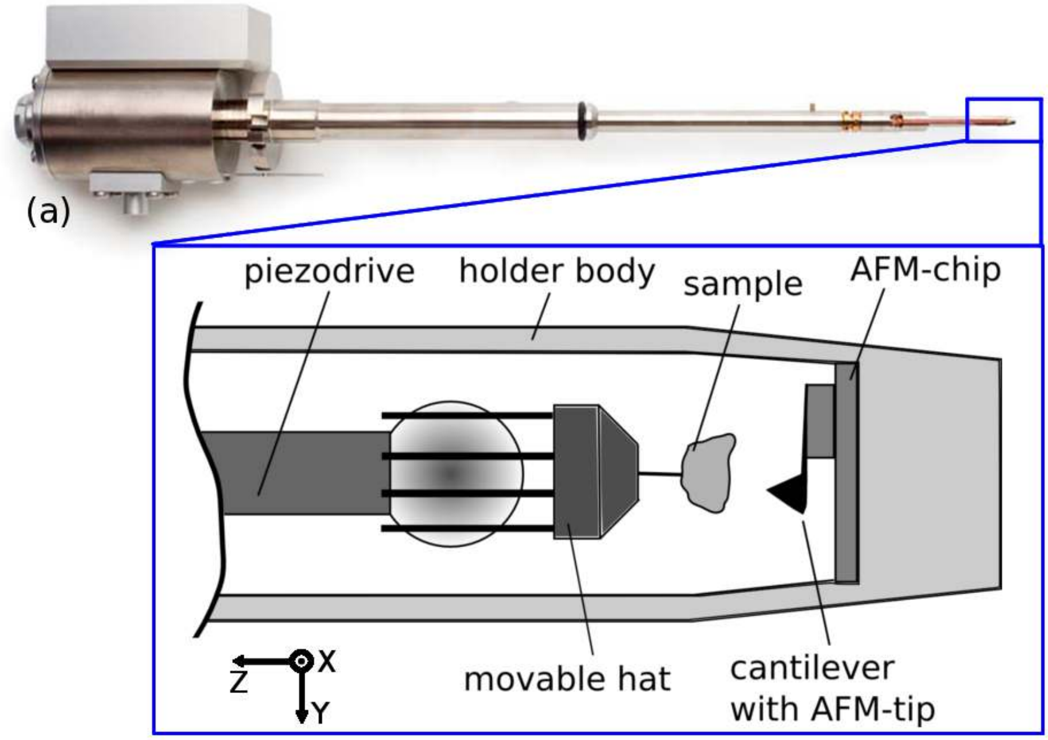

Figure 3.10: (a) Photo of the commercially available AFM-TEM sample holder (Nanofactory Instruments) used to perform AFM *in situ* TEM measurements. It represents the variant of usual single-tilt holder, used in state-of-the-art transmission electron microscopes. The on-board pre-amplifier and the cable interface are situated in the left part of the holder. After inserting the sample holder inside the TEM, the tip of the holder body is positioned between the pole pieces of the objective electron lens. On the schematic view (b) of the holder tip the main parts of AFM-TEM-system are shown, these are a fixed AFM-sensor and a movable hat with the sample on it. Denoted axes directions are consistent with directions shown in figure 3.11. Note the electron beam goes along X-axis, i.e. normal to the plane of the image.

which repetitive motions afford the hat holder to slide inertially over the metal ball in three dimensions. Since the piezotube carries the sample, then the bending of the piezotube or its lengthening gives rise to the correspondent displacement of the sample. This is the fine movement regime, which provides nanometer precise positioning of the sample.

3.2.2 AFM-sensor description

A schematic view of the AFM-sensor is shown in figure 3.11 (b). Silicon micromachining is used to fabricate the electrical and mechanical elements of the AFM-sensor [28]. The force detection is based on the piezoresistivity of one of the arms of a Wheatstone bridge (R_4 at figure 3.11 (a)). The piezoresistive circuit elements are represented by boron implanted areas of cantilevers. To induce the current change through the galvanometer one should bend the cantilever, which changes in the resistivity of piezoresistive element.

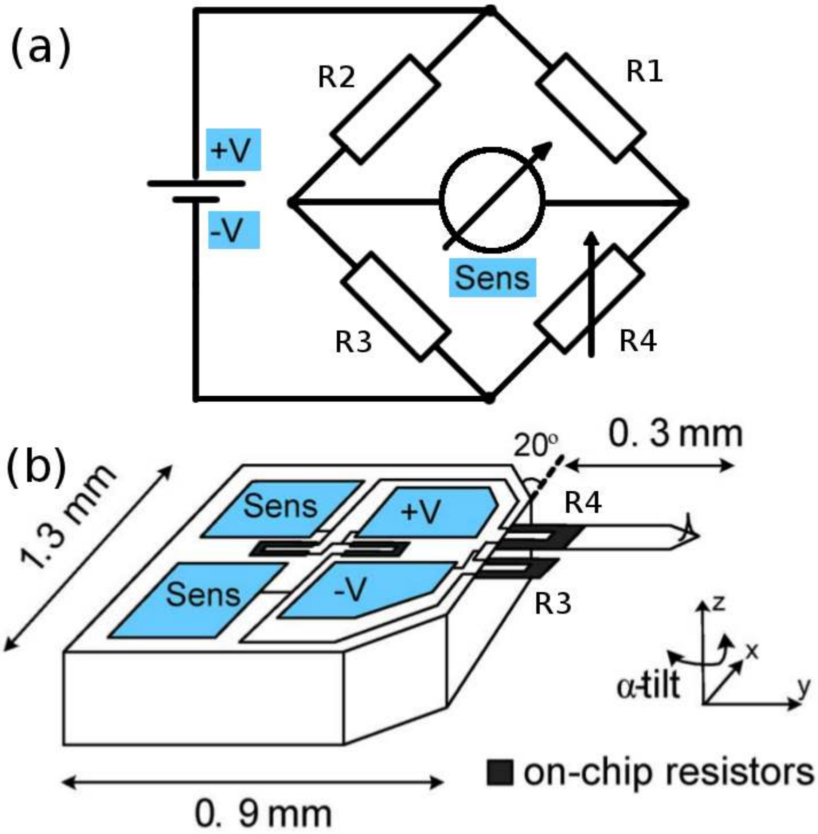

Figure 3.11: Wheatstone bridge electrical circuit shown on figure (a) is used as the basic part of force measuring system in the AFM-sensor (b). On the schematic view (b) the contact areas (blue), wire tracks as well as resistive elements (in gray) are shown. Contact areas are used to connect elements of Wheatstone bridge electrically with thin gold wires. The notation of elements on the electrical circuit corresponds to the one on the schematic view. The image (b) is adopted from [28] with modifications.

The potential difference caused by the changed resistance is measured by means of the galvanometer in the interfaced amplifier unit and consequently translated in the displacement of cantilever using electrical conversion factor. The electrical conversion factor c is determined by the calibration procedure done at the factory. The procedure consists in pressing the AFM-cantilever against a hard surface and simultaneous measuring the bridge output $U\,(mV)$ and displacement $\Delta x\,(nm)$. As the equation

$$U = c\Delta x \tag{3.18}$$

Sensor ID	Cantilever dimensions $l \times w \times t\,[\mu m]$	$k\,[N/m]$	$c\,[mV/nm]$
W4D6#17	300/70/3.4	4.1	5.2
W4D19#12	300/70/3.0	2.8	5.8

Table 3.1: Parameters of cantilevers used in this study.

is valid, the estimated electrical conversion factor c can be used for the force determination [28]:

$$F = k\Delta x = k\frac{U}{c}, \tag{3.19}$$

where k is the spring constant of the cantilever approximately given by elasticity theory:

$$k = \frac{Ewt^3}{4l^3}, \tag{3.20}$$

where E is Young's modulus, l,w and t are cantilever dimensions (see table 3.1). As one can see from the figure 3.11, an additional cantilever is introduced to compensate the current drift in the Wheatstone bridge due to temperature change.

Since parameters k and c of the cantilever are required for the force calculation, they are provided in support documentation by manufacturer. For the sensors used in the study, the cantilevers parameters are listed in table 3.1 [21]. Detailed information about the manufacturing and characterization of AFM-chips can be found in [28].

SEM-micrographs of two cantilevers are shown in figure 3.12. Micrographs represent the sideways overview. One can clearly distinguish the conical AFM-tip. The height of the tip does not exceed 2.5 μm.

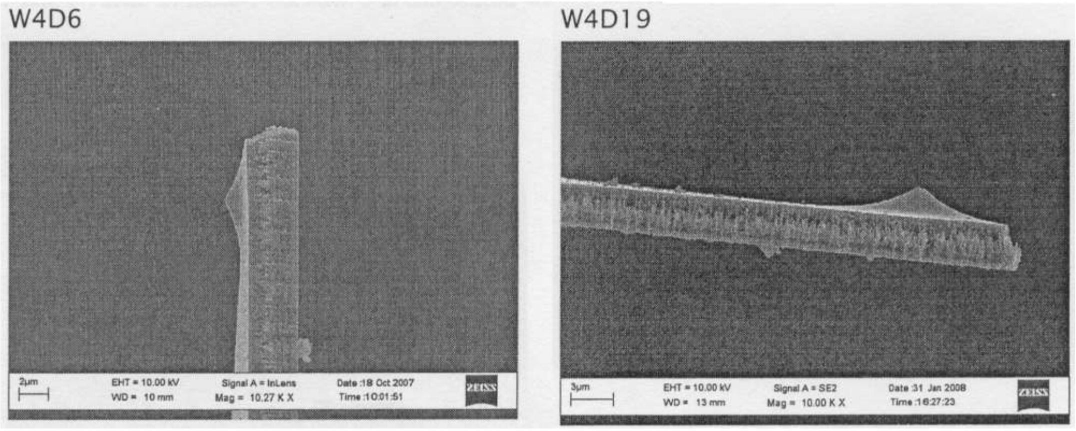

Figure 3.12: Two AFM-sensor tip SEM micrographs, which were used in my experiments. Sensor data including cantilever dimensions and spring constant are listed in table 3.1. Adopted from [21].

3.3 Experimental procedure: tests on a bare Cu substrate

In this section I describe the experimental procedure of AFM load-unload tests on a bare copper substrate. This preparative testing was intended to establish the operational procedure. The substrate was prepared by the ”half TEM-grid”-electrode preparation method described in section 3.1.3. The AFM *in situ* TEM test using the described in section 3.2.1 AFM-TEM sample holder was implemented in several steps:

1. Adjustment of control software for each AFM-sensor. Since the software calculates the force automatically using the equation 3.19, these parameters should be set into the software options every time after sensor replacement.
2. The placing of the sample in the hat holder and consequently mounting the hat holder into the sample holder. Hereafter, one performs the approach of the movable part (sample) to the fixed part (AFM-cantilever) of the system by hand using fine tweezers under optical microscope. The distance between sample and cantilever should not be less than $200\,\mu m$ to prevent the damage of the system components by mechanical vibrations during the mounting sample holder into TEM column.
3. The sample holder is inserted into the TEM and the usual microscope alignments are performed. This and the following steps are performed inside TEM. The visual control of the whole procedure carried out by TEM imaging. One should find the movable part of the holder with sample on it and perform its preposition with respect to the AFM-tip. The operating range of fine positioning does not exceed $\pm 10\,\mu m$ along axes Z and Y (according to figure 3.10) and $\pm 1.2\,\mu m$ along the axis X. One should bring very gently the sample to the tip. To simplify the height adjustment, it is convenient to use the beam wobbling of TEM.
4. When the distance between the sample and the cantilever is in the range of fine movement, the fine sample positioning to be performed. The sample should be brought to the position, which later will be the test start position. Whereas the in plane positioning is very straightforward, the height adjustment of the sample and AFM-tip requires the special procedure. One adjusts the focus of the TEM first on the fixed part (the AFM tip). Then one resets to zero the defocus value at microscope control. Afterwards one adjusts the focus

on the movable sample. The defocus value at microscope control shows the hight difference between the AFM-tip and the sample. Then one changes the hight position of the sample and check the hight difference again, repeating the whole sequence as much more as needed.

5. The measurement parameters may be adjusted prior to each test trial by control software. It is worthy of note, there are two basic modes of operation for this sample holder. First is the scanning mode while the second mode is the local force spectroscopy. Since my measurements were performed only by the second technique, I list here only measurement parameters relevant to that technique:
   - **Acquisition time** in ms. The entire time of a single measurement.
   - **Dual slope/single slope** option. The measurement may be performed either in one direction i.e. forward (single slope) or with return to the reference point, i.e. forward and back (dual slope). For the AFM-tests concerning the capturing of force-displacement characteristics it is useful to choose the dual slope option, because the backward measurement is important for measurement corrections which will be discussed later.
   - **Start/stop values** for measurement in nm. In case of the AFM-sample holder, these values determine the minimal and maximal values for the sample displacement.
   - **Input/output channel** values, which determine, what will be measured (input channel) as function of variable parameter (output channel value). For the capturing of force-displacement plot, the input channel is set to the force whereas the output channel is the displacement along the stretching Z-axis.
   - Number of acquisition samples, which is upper limited by 2000.
6. The AFM-test itself can be started after parameters adjustment. The test is proceeded in accordance with its description in section 2.2.3. Briefly it consists of the sample movement to the AFM-tip, followed by cantilever jump to the contact. Hereafter, further movement of the sample-tip system occurs until the maximal displacement, which is set by the **stop value** parameter, is reached. Then if the **dual slope** option has been chosen the sample moves backwards.

The typical sample-tip arrangement during the test is shown in figure 3.13 (a). Here the AFM-tip is in the right upper part of the TEM-micrograph, the sample is in the left bottom part. The movement directions are marked with arrows. The blue and red arrows correspond to the forward and backward sample movement, respectively.

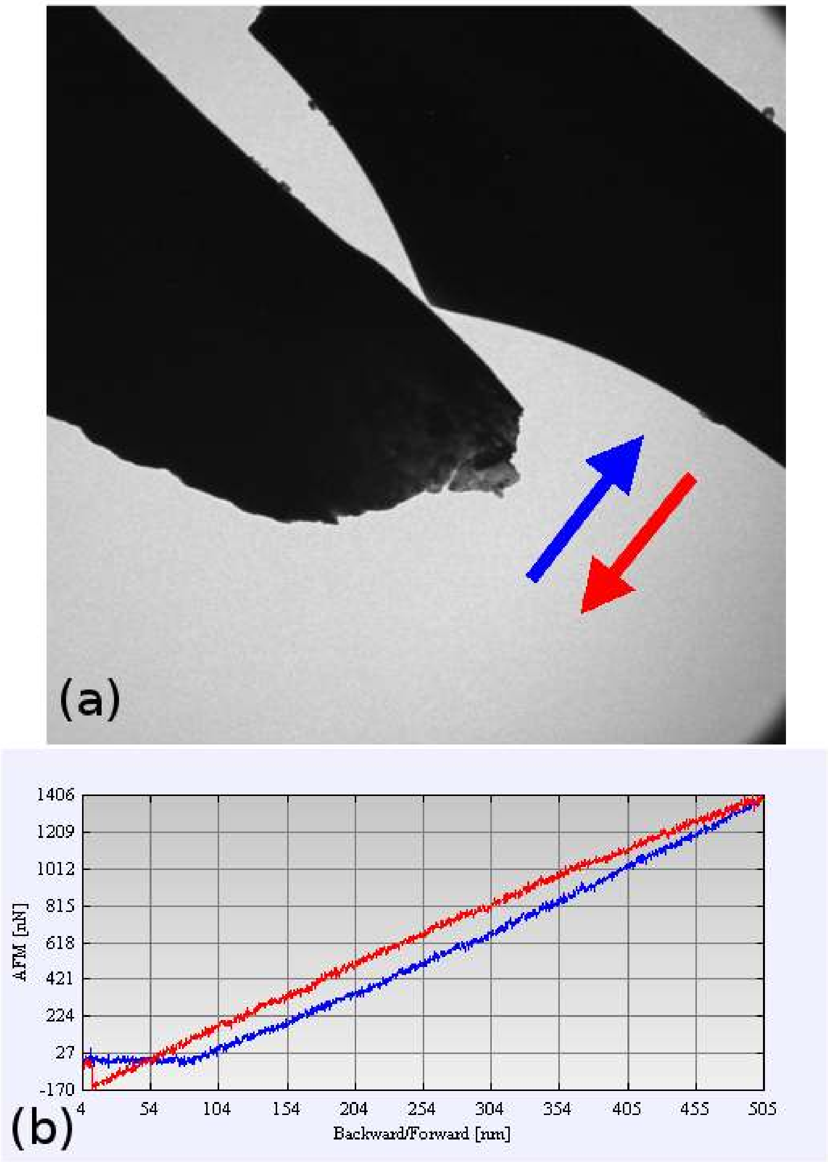

Figure 3.13: (a) TEM-image of the bare substrate (left) in contact with the cantilever (right) concerning load-unload experiment. Blue and red arrows show the movement direction of the cantilever during the test. The corresponding Force-Displacement curves shown on the image (b).

In figure 3.13 (b) the typical resulting Force-Displacement plot (FD-plot) of such test is depicted. On the Y-axis the measured force as function of sample displacement is plotted. Applying to the system cantilever-sample the model of two springs, it is possible to extract from the FD-plot a total spring constant of the system k_{tot} from the FD-plot [28]:

$$k_{tot} = \frac{k_c k_s}{k_c + k_s}, \tag{3.21}$$

where k_c and k_s are the spring constants of the cantilever and the sample, respectively. Moreover, if the sample does not deform during the test or deforms negligeable, the cantilever spring constant k_c can be extracted directly as the slope of FD-plot. Thus, the comparison between the measured value and the value reported by the manufacturer could be done. For the "bare substrate" experiment the copper grid as the sample was used. Due to large displacement values and relatively low hardness of Cu (in comparison with the tip material Si_3N_4) some undesirable effects such as imprinting the tip into the sample or plastic deformation of the sample may distort the FD-plot. Thus, the extraction of the AFM-cantilever spring constant k_c using the copper substrate would be erroneous. As a consequence, using of the bare substrate sample with higher indentation hardness (Si, or even diamond) would be recommended for precise setup calibration.On the FD-plot all characteristic features which show the difference between ideal (in elastic regime) and experimental plots can be observed. These features (non-linearity of the slopes or differing slopes in load and unload regimes etc.) with their significance will be disclosed later.

3.4 Experimental procedure: tests on InAs nanowires

Here, the experimental procedure of InAs nanowires testing and the evaluation of experimental data will be presented. Some examples of load/unload tests video on InAs nanowires are presented in multimedia appendix. The idea of test configuration for AFM load-unload testing of nanowires is schematically depicted in figure 3.14. In this case instead of the bare substrate, InAs nanowires aligned by dielectrophoresis are to be tested. By TEM imaging a nanowire lying on the substrate (which is represented by copper "half-TEM grid" electrode) is to be found. The wire should stick out against the electrode edge so that the AFM-tip able to reach the nanowire. The substrate as well as the sensor are positioned in the AFM-TEM sample holder, which is inserted into the TEM. The measurement procedure generally does not differ from the procedure of bare substrate testing (see previous section 3.3) except for some important details. The experimental procedure of AFM-testing of nanowires is a modification of experimental procedure proposed by [12].

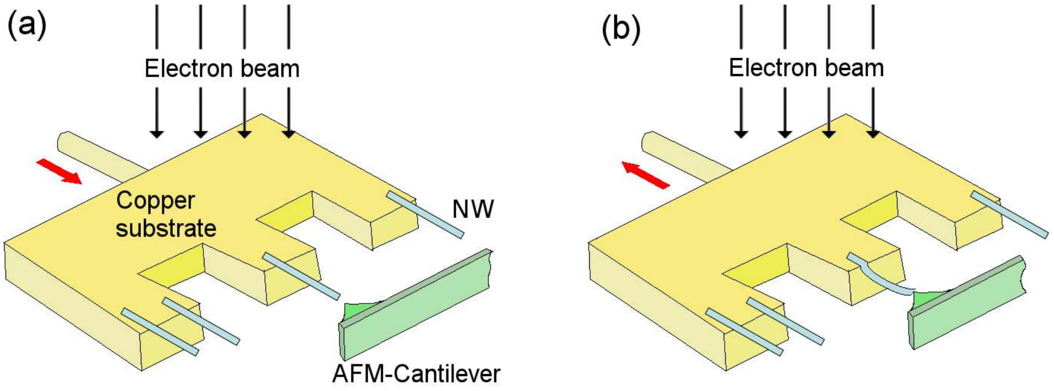

Figure 3.14: The schematic shows the arrangement of the nanowire on the substrate (as a movable sample) and AFM-cantilever (as fixed part). The sample and the AFM-sensor are pushed into the AFM-TEM sample holder, which is in its turn inserted in the TEM. The configuration before the test and during the test by the maximal displacement is presented in (a) and (b), respectively. Red arrows show the direction of forthcoming substrate movement. The electrons path in TEM is nearly perpendicular to the substrate.

The yield of aligned nanowires varies for every DEP trial. This yield depends mostly on the local spatial configuration of electrodes, which is different each time. Although the positioning of counterelectrodes is supposedly micrometer precise, in actual practice it becomes troublesome or even sometimes impossible to bring electrodes to optimal configuration. The reason is, that the working range of both micropositioning stages is severely restricted. Due to specialties of mechanical design, the positioning error becomes significant near the working range boundary. Because of this, the yield of useful wires aligned by DEP does not go beyond $15-20$ per electrode.

In fact, in $15-20$ samples there are typically only few nanowires that may be considered as appropriate, which meets the set of requirements:

- The nanowire should lie parallel to the sample holder tilt axis, that is in the plane which is perpendicular to the electron beam. It raises the chances to find the Bragg condition by means of sample tilting and then to acquire a diffraction image, how it was already explained in section 3.1. More important, the Young's modulus calculation by used method is possible only if the nanowire length is known. But if the wire is out of the plane, which is perpendicular to the beam then the direct length measurement by TEM is impossible since in TEM only the projection of the wire is observed. When the nanowire belongs to image plane the length of its projection is equal to its real length. To control whether the wire is perpendicular to the electron beam one can check the focus values at the fixing point and the end point of the nanowire. The angle between the electrode edge and the nanowire should be near 90°.

- The nanowire does not touch any other nanowire or dirt pieces. Otherwise, the characterization by our technique become pointless because of interference with those objects.
- The wire should not be tapered, i.e. it has the same diameter along the overhang length. Since the majority of elasticity experiments are carried on the non-tapered nanowires, I chose only non-tapered wires. Moreover, the tapering of the nanowires may complicate the calculation.
- Our method of testing implies that the nanowire should be fixed on the electrode since the change of wire length under load is relevant for the further calculation. In fact, the adhesion forces between the nanowire and the copper substrate are high enough, that the wire almost always stays fixed during the bending tests.

In the following sections I present the experimental procedure and evaluation of results on individual InAs nanowires. Among the tested wires four of them are chosen for evaluations. Half of them is of type II (samples denoted by M7 and M3), and the rest is of type III (samples M6 and M1). Measurements on samples M1 and M3 were carried out in a TEM Philips CM12, unless otherwise noted. Samples M6 and M7 were measured in TEM FEI Tecnai F20.

3.4.1 Nanowire M7

TEM micrograph of the sample M7 is shown in figure 3.15 (a). On the bottom part of the micrograph one can see the substrate, which is the edge of the electrode. The nanowire was chosen in accordance with fore-mentioned requirements for the sample (see section 3.4). The TEM image gives always the projection of the sample. The projection length and visible diameter of the sample were measured from the TEM images and amount to $(515.0 \pm 0.6)\,nm$ and $(45.7 \pm 0.9)\,nm$, respectively. The opposite ends of the nanowire are both near in focus, therefore one shall accept the projection length as the wire's real length with regard to the error, introduced by this assumption.

It is possible to determine the type of the nanowire directly from figure 3.15 (a) . The sample is identified as the InAs nanowire of type II with dense rotation twinning planar defects since one finds a contrast of stripes perpendicular to the

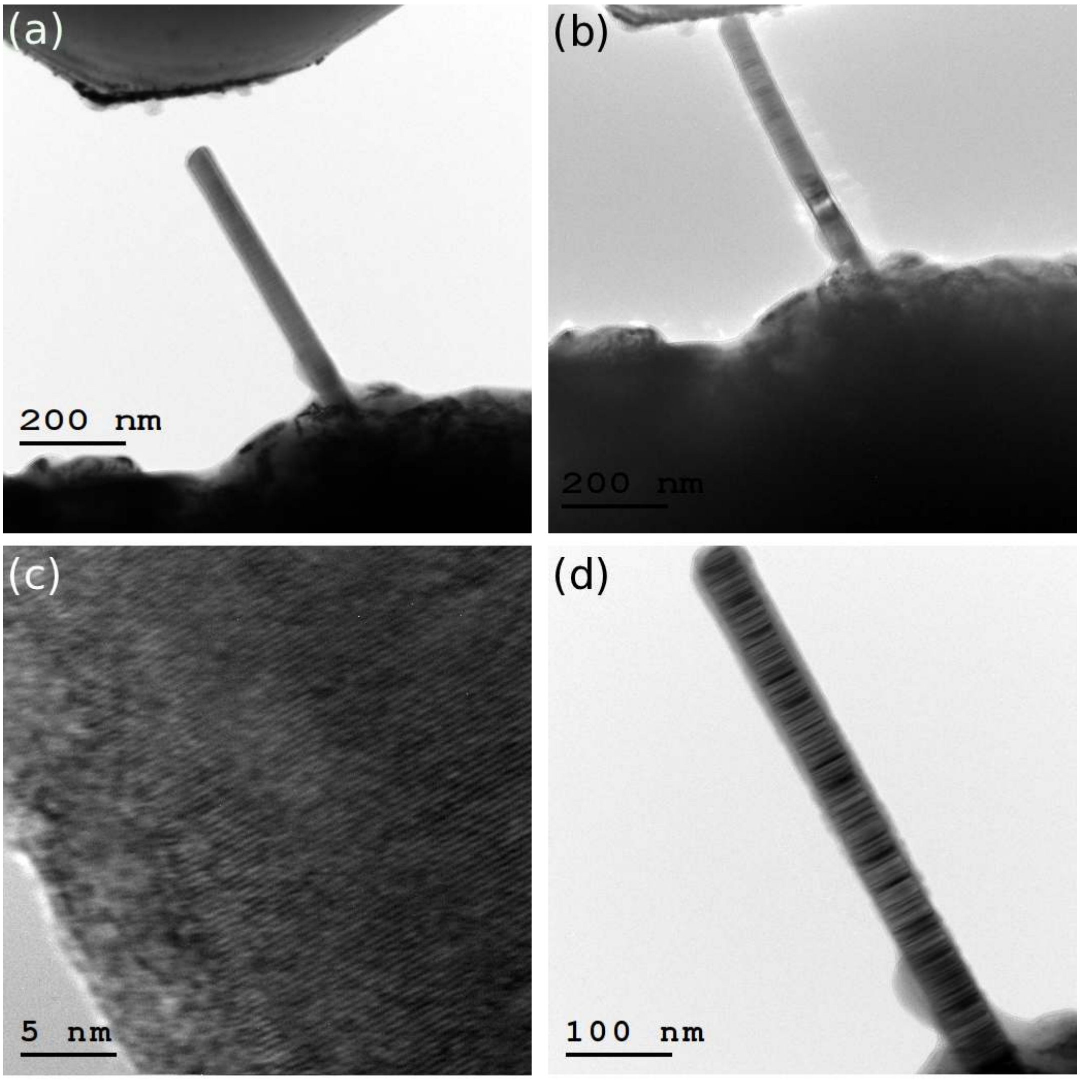

Figure 3.15: TEM micrographs of the nanowire M7 before load (a) and during load, i.e. in contact with the cantilever (b) during load-unload experiment. The HR-TEM image of the wire (c). The shell of contaminations of thickness about $5\,nm$ can be distinguished.

nanowire growth direction. The HR-TEM micrograph 3.15 (c) shows that the wire is covered with an amorphous layer which can be attributed most likely to amorphous carbon. Although the carbon deposition is a common effect observed due to decomposition of rest gases by electron beam exposure, the second source of this visible contamination is the DEP procedure. Thus, the suspensions of the nanowires used by DEP are very susceptible to any contamination since the water or isopropanol is used as solvent. Contaminants may be dissolved in the solution during the solution preparation, as well as during DEP by contact with electrodes. As one can see on the TEM image, there is increased contaminations layer on the wire near to the substrate-wire contact point. It is consistent with the assumption that contaminants dissolved in the solution and remain during drying of the solution during DEP.

AFM-TEM tests were performed on the sample M7 as described in sections 3.3 and 3.4. Figure 3.16 (a) shows the typical Force-Displacement plot acquired by the AFM-testing of the sample M7. The force measured by AFM-sensor is plotted along Y-axis while the substrate displacement is plotted along X-axis. Comparable to figure 2.6, the experimental plot has the identical characteristic regions. Please mention that the Y-axis in figure 2.6 is inversed in comparison to the Y-axis direction in figure 3.16 (a). Refer to section 2.2.3 for detailed explanations of marked regions.

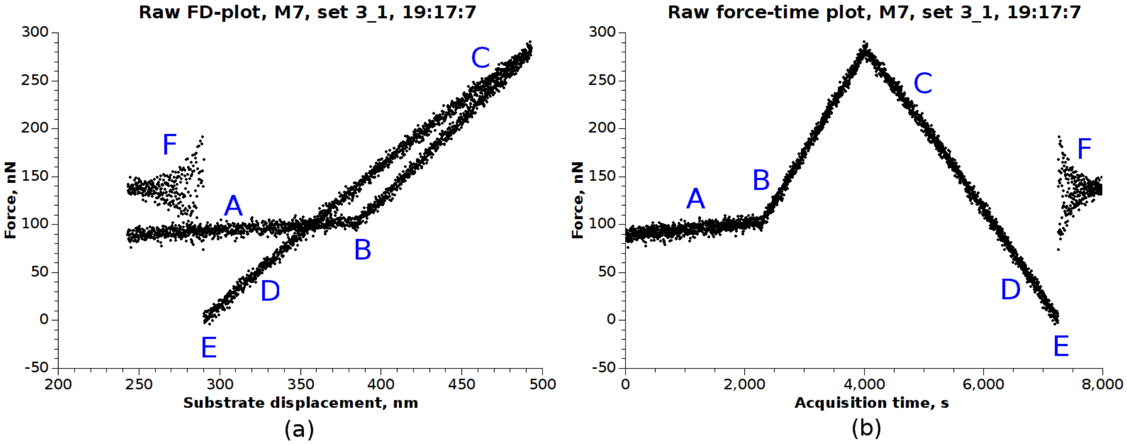

Figure 3.16: (a) Experimental raw force-displacement plot of AFM-test for sample M7. The upper-case letters mark the main regimes of the test in accordance with the explanation in section 2.2.3. (b) shows the force behavior as the function of acquisition time.

To clarify the FD-plot the corresponding force dependence on time is shown in figure (b). The regions in this plot are marked consistent with the FD-plot. The acquisition time of both load and unload regimes is 4 seconds each, that is an AFM-test duration of 8 seconds.

The FD-plot shows that during the approach the force increases. Even more, the approach curve (region A) does not coincide with the retracting curve (region F). In fact, it indicates the influence of an undesirable charge effect, which should be eliminated. The correction of the force-displacement plot is performed for all experimental plots and will be shown on the example of the nanowire M7.

Correction of Force-Displacement plots

In case of force-displacement plots the correction of raw data has several steps, which should be done before the interpretation and discussion of physical processes. We take a detailed look at correction steps.

1. The raw force-displacement plot starts from non-zero values of the force and displacement. Regarding the displacement, for the preparation of each AFM-test the positioning of the sample near to the cantilever is required. That is done by means of fine movement of the piezodrive. Since the piezo is already stretched to the test begin, the displacement value on the plot shows this offset, which is generally non-zero. Thus, one performs the shift of the whole graph along X-axis. Two possibilities are feasible here: the zero displacement point may be assigned either to the first measured point or to the point B of the tip-wire contact establishment. It is preferable to follow the second way since in this case the region of contact is more important than the approach region. This step of correction is illustrated by figure 3.18 (a).

2. As can be observed in majority of raw FD-plots, the force increases in the approach region, where the force should be constant. The so-called charge effect can be assumed as the main disturbing effect during the AFM-TEM tests. Due to electron beam illumination of the cantilever electrons are absorbed by the cantilever. Accumulated charge drains through the piezoresistive layer, resulting in an additional current in the detector circuit, as it is shown in figure 3.17. Total current is then converted to the force, yielding the increasing force.

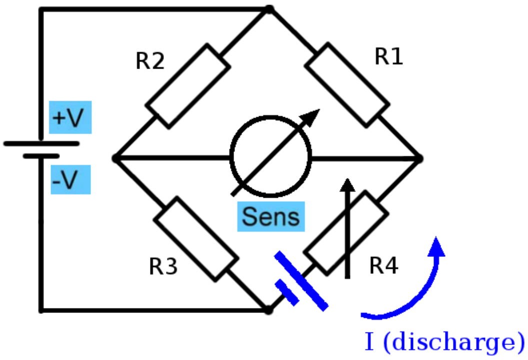

Figure 3.17: The Wheatstone bridge detection circuit with additional source resulting in the discharge current flow

One assumes that the charge effect depends linearly on time. Therefore, to eliminate this effect one should determine the slope of the region A. One obtains the slope by linear approximation $y = B + Ax$ of the region. Here two steps of the test - forward and backward sample movement - are handled differently. For the forward movement one should recalculate each actual force value F_i by subtraction (or addition) of the slope value A multiplicated by the actual displacement value x_i:

$$F_{i,corr} = F_i \pm A \cdot x_i. \tag{3.22}$$

The sign is determined, whether the charge effect is ”positive” or ”negative”. If it is ”positive” the growth of force value occurs by untapped cantilever and vice versa. Since measured points of a FD-plot are plotted by backward movement against the same displacement axis and inversely, the addition to each actual force value (or substraction in case of ”negative” charge effect) should be performed. Note that the tailoring of resulted forward and backward curves should be carried out. Hence the additional term is in the equation for arbitrary force value:

$$F_{i,corr} = F_i \mp A \cdot x_i \pm 2A \cdot x_{max}. \tag{3.23}$$

3. Finally the last correction step is the elimination of the force offset, which is present on every raw FD-plot. For instance, force values for the approach are typically non-zero due to slightly unbalanced detector scheme, which, however, does not affect the measured data reliability since it is the effect of the offset. At this step only the addition (subtraction) of the offset value B to each force value F_i is required, resulting in the final formula:

$$F_{i,corr} = \begin{cases} F_i \pm A \cdot x_i \pm B & \text{if } x_i = [x_0;\, x_{max}]; \\ F_i \mp A \cdot x_i \pm 2A \cdot x_{max} \pm B & \text{if } x_i = [x_{max}; x_0] \end{cases} \tag{3.24}$$

The result of correction step 2 and hereafter 3 is shown in figure 3.18 (b). Measured points of load (forward movement) and unload phase (backward movement) are marked with black and red, respectively.

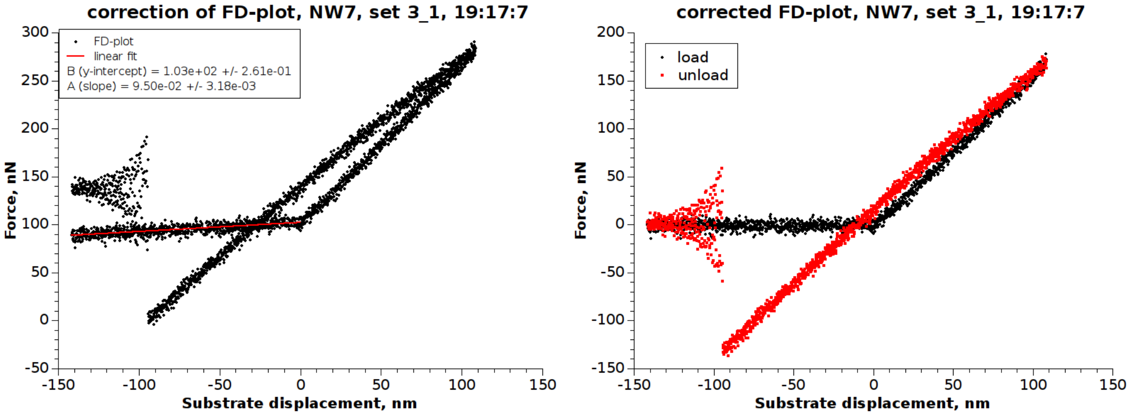

(a) (b)

Figure 3.18: (a) The force-displacement plot shifted along X-axis in accordance with first correction step. Zero substrate displacement point corresponds now to the contact establishing point of nanowire-cantilever system. (b) The corrected FD-plot: eliminated charge effect and zero force offset.

Further evaluation

Bending tests are performed several times in several measurement sets. Initial conditions (start/maximal sample displacement value, acquisition time, initial sample position) within the same measurement set are approximately equal. Every AFM-test is accompanied by acquiring a video. As mentioned earlier, the combination of FD-plot and video capture allows to unambiguously match the image of a bended nanowire with its position in the FD-plot. In the case of TEM Philips CM-12 the CCD-camera in live mode with 512 × 512 pixels resolution has been used whereas the GIF-TV with resolution 768 × 576 pixels has been used in TEM FEI Tecnai F20. Unfortunately, the video provides the degraded quality comparable to static imaging, as well as artifact addition by video encoding. Hence, video films were used practically only to determine the radius of curvature of wires by maximal displacement. Snapshots of characteristic moments of a selected AFM-test are depicted in figure 3.19.

As was discussed in section 2.3.1 the Young's modulus is estimated in our method using the equation:

$$E = \frac{2R_{max}^3 F_{max}}{I \cdot l}. \tag{3.25}$$

For the purpose of Young's modulus evaluation the following information is required. First of all, the corrected FD-plot is used for extraction of the maximal force value F_{max} (force by maximal bending). Let us call F_{max} in the FD-plot the "reversal point" since it is the transition from forward to backward movement of the sample.

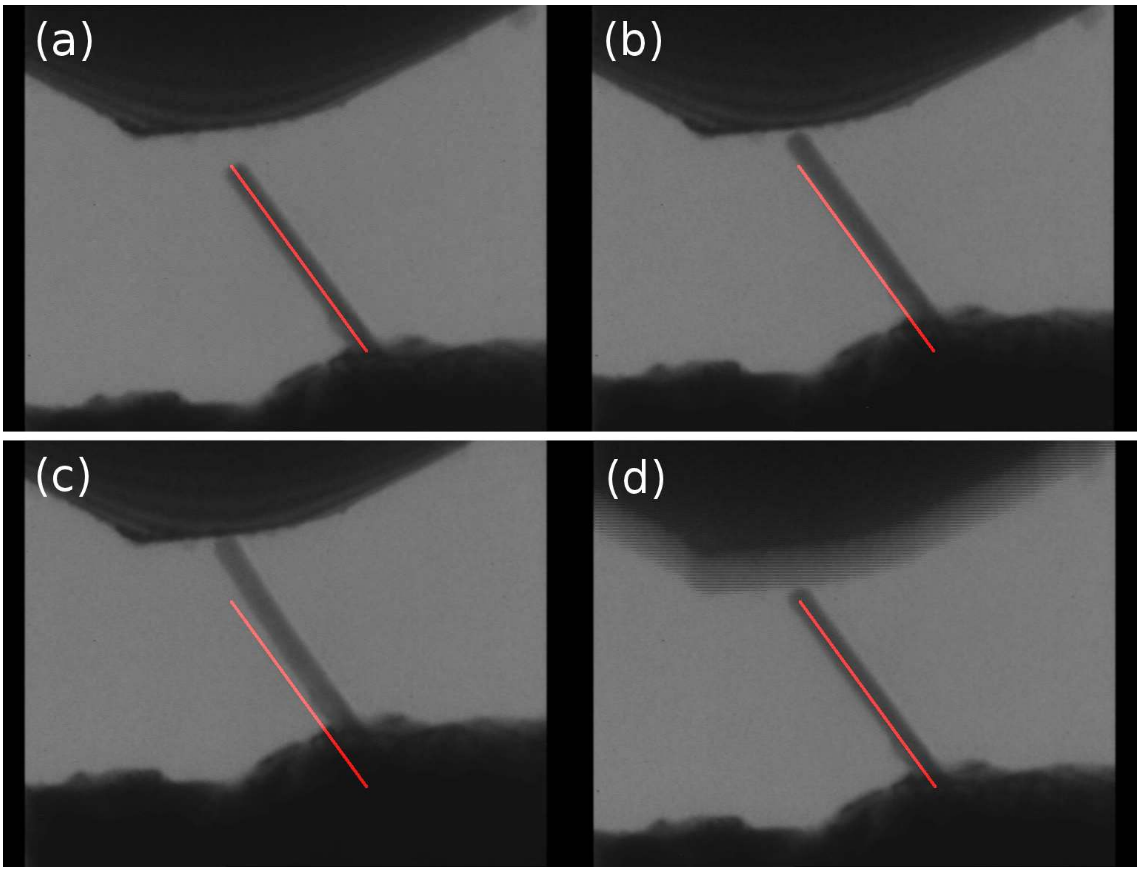

Figure 3.19: Characteristic moments are shown in video snapshots of AFM-load/unload test: (a) approaching to the cantilever tip; (b) snap to the contact; (c) maximal substrate displacement; (d) snap-off from the contact. Red line, which corresponds to the length of the nanowire centerline, is shown as a reference. Since the red line stands still, one can clearly observe the movement of both cantilever tip and the substrate. The curvature of the wire is observed in snapshot (c). The snap-off moment (d) is characterized by a smeared-out image of the cantilever.

This point is remarkable by the following reasons. It is very easy to match this reversal point with the corresponding image in the video film. On the other hand it is often impossible to match the start of the AFM-test with the start of the video recording. The synchronization of these two events ia very inaccurate since they are synched by hand. Also a time-lag exists caused by software processing.

The second important constituent of the elastic modulus determination is the radius of curvature of the nanowire in the condition of maximal bending. Since the transmission electron microscopy does provide only the projection of the objects, a special geometrical approach is introduced. Figure 3.20 (a) shows the bended nanowire, where the bending plane does not coincide with the image plane. The red dashed line designates the centerline of the wire while the blue line is the length l' between end and fix point of the wire. We assume that the local radius of curvature is equal to the total radius of curvature, i.e. the wire bends everywhere equally along its length. In this case the apparent curvature radius is not equal to the real radius. It will be shown, that the radius of curvature can be found by means of direct length l', real length l. Let us change the location of viewer so, that the image plane now coincides with the bending plane (figure 3.20 (b)). Consider the triangle ABC, that lies in the image plane. The centerline of the length l is also the arc of length:

$$l = R \cdot \alpha. \tag{3.26}$$

Here R is the radius of curvature and α is the angle between radii denoted by AC and BC. CD and BE are altitudes of the triangle ABC. Since ABC is an isosceles triangle with $AC = CB = R$, the altitude CD is also a bisector of the angle $\angle ACB = \alpha$. Then, from the geometrical considerations it is provable, that triangles ACD and ABE are similar. It follows that their angles are equal:

$$\angle ACD = \angle ABE = \alpha/2, \tag{3.27}$$

and it follows:

$$\sin \alpha/2 = \frac{AE}{AB} = \frac{AB}{2R} \tag{3.28}$$

Finally, by the substitution of the equation 3.28 into 3.26 and taking into account, that $AB = l'$, one obtains:

$$R = \frac{l'}{2 \sin \frac{l}{2R}}. \tag{3.29}$$

This equation can be solved for R only numerically. For the solution I used the open source numerical analysis software GNU Octave [5]. Thus, knowing l' from the video snapshot by maximal bending and l from preliminary acquired TEM-image one can determine the radius of curvature R regardless to the position of the bending plane.

Correction of the snapshots

TV-CCD camera of TEM Tecnai F20 can be used for video acquire by means of capturing the video from video-out into PC. It is noted above, that the video acquired by TV-CCD has the resolution 768 × 576 pixels (aspect ratio 4 : 3). This resolution is predefined by the capturing software. Since there was no resolution with aspect ratio 1 : 1, the correction of the raw video is required. An additional problem complicates this operation. Namely, there are black margins on both left

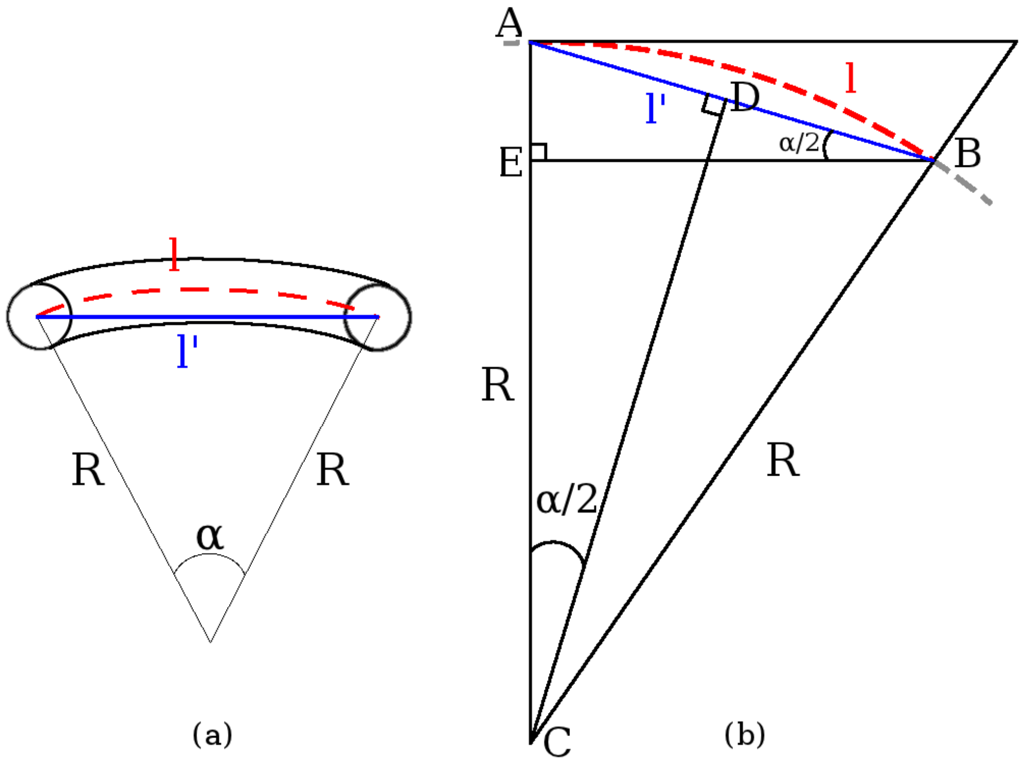

Figure 3.20: (a) A schematic model of the bended nanowire of the length l. The wire is bended in the plane, which does not coincide with image plane. The bisecant l' is lying in the image plane while it connects end points of the wire. Figure (b) shows the scheme of the threatened geometrical problem in the bending plane. The centerline of the bended wire is marked with dashed red line. The isosceles triangle ABC is formed by three sides, two of them are curvature radii while the third side is the bisecant l'.

and right sides of the acquired video. Thus, it is not clear, whether these margins are introduced by means of shrinkage of the original video signal or only by overlapping with it. The snapshots taken from the raw video by the TV-CCD camera are corrected as follows. The goal is to find once the correct scaling factor which will be used as multiplier of the snapshot height (width). After multiplication with this factor, each pixel both along the snapshot height and width will correspond to the same value in nm. Several steps are implemented here:

1. Taking a video snapshot (see figure 3.21 (b)) of the load/unload test at approaching phase. Then one selects a TEM-micrograph (figure (a)) of the wire, which was taken prior to the associated load/unload test.
2. One draws reference intervals on both images, so that the ends of the intervals belong to the same positions on the wire. These positions should be identifiable on both images. Thus, intervals a_1 and b_1 correspond to intervals a_2 and b_2, respectively.

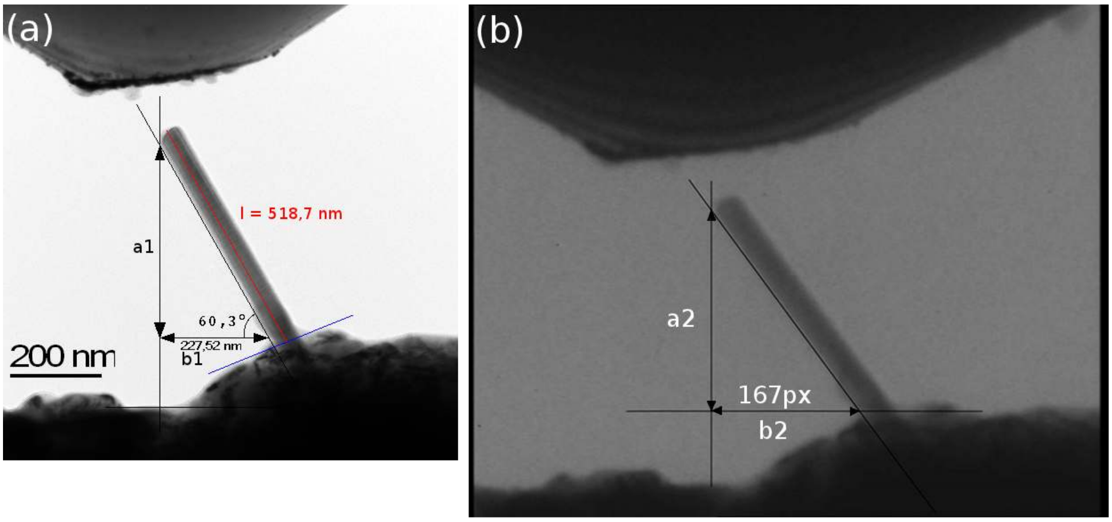

Figure 3.21: Figure (a) shows a TEM-micrograph of the nanowire while the corresponding video snapshot is shown in (b). Horizontal and vertical scales of the uncorrected snapshot are not equal. Two right triangles are build on four intervals. Herewith intervals marked as a_1 and b_1 correspond to a_2 and b_2, respectively. The correction of snapshots implies the calculation of the rescale factor and the multiplication the snapshot height with this factor, so that the scales of the snapshot become equal.

3. The measurement of the reference parameters: length of the interval b_1 (in nm), the inclination angle $60.3\,^\circ$ of the wire to b_1, and the length of the interval b_2 (in pixels). One immediately obtains the conversion factor for the TV-CCD snapshot as the ratio $\frac{b_1}{b_2} = \frac{227.52\,nm}{167\,px} \approx 1.362\,nm/px$.
4. One measures the interval a_2 of the uncorrected TV-CCD snapshot. Hereafter the rescale factor for the height of uncorrected TV-CCD snapshot can be found as the quotient:

$$\frac{\frac{a_1}{b_1}}{\frac{a_2}{b_2}} = \frac{\tan 60.3\,^\circ}{\frac{226\,px}{167\,px}} \approx 1.296. \tag{3.30}$$

Note that the correction procedure needs to be recalculated, if the TV-CCD video is acquired with another magnification.

Young's modulus evaluation

Now I present the explicit Young's modulus evaluation on the example of sample M7 (set3-1, 19 : 17 : 7). Consider the TEM TV-CCD video snapshot by maximal load, which is depicted in figure 3.22 (a). The snapshot has been corrected as described above, so one may directly measure the length l' of the interval between end- and fix-points. As it is shown in figure 3.22, the bisecant l' is limited by the blue line. This line was chosen as the substrate edge in this particular case. The line lies on the same characteristic points, as the similar line sketched in the TEM-micrograph (see figure 3.21 (a)). The wire length measured at the TEM-micrograph l is then equal to $(518.7 \pm 0.6)\,nm$ while the l' measured from snapshot equals to $(497.1 \pm 1.3)\,nm$. The force by maximal load can be found from the corresponding FD-plot shown in figure 3.22 (b) as the average of two force values, specified by linear fits of load/unload regions of FD-plots. The force average of two values by maximal displacement is equal to $F = 172 \pm 2\,nN$. The nanowire diameter determined from TEM-micrograph is equal to $42,4 \pm 0.9\,nm$. Using equation 3.29 one calculates the nanowire's radius of curvature, which in this case is equal to $516\,nm$. Since the type II nanowires have the cross-section of a truncated triangle, the second moment of area I can be found using the equation 2.25, yielding the value $97945\,nm^4$. Finally, the Young's modulus is given by:

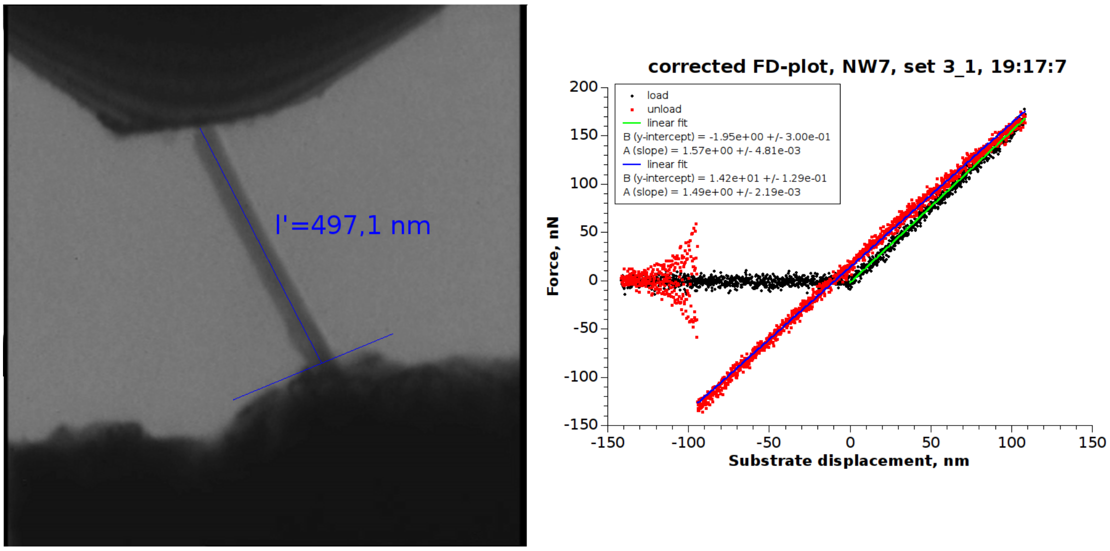

Figure 3.22: The corrected snapshot at the maximal load is shown in (a). The interval between end- and fix-points is measured by using this snapshot. Force-displacement plot (b) of the load/unload test is used to extract the value of the acting force.

$$E = \frac{2R_{max}^3 F_{max}}{I \cdot l} = \frac{2(516\,nm)^3 \cdot 172\,nN}{97945\,nm^4 \cdot 518.7\,nm} = 687\,GPa. \tag{3.31}$$

Results for the rest of AFM-tests on this sample will be shown after presentation of error calculation.

Error calculation and results summary for the sample M7

A standard error propagation schema was applied for the error estimation. Here I illustrate the error calculation of Young's modulus using one of AFM-tests on sample M7 as an example. Using equation 3.25 for Young's modulus in our method and combining the equation for the second moment of area I (see equation 2.24) one can write:

$$E \propto \frac{R^3 \cdot F}{I \cdot l} \propto \frac{R^3 \cdot F}{d^4 \cdot l} \tag{3.32}$$

Then, for the largest possible error the following standard treatment is valid:

$$\frac{\Delta E}{E} = \sqrt{3\left(\frac{\Delta R}{R}\right)^2 + \left(\frac{\Delta F}{F}\right)^2 + 4\left(\frac{\Delta d}{d}\right)^2 + \left(\frac{\Delta l}{l}\right)^2} \tag{3.33}$$

The estimation of the relative error $\frac{\Delta R}{R}$ is not trivial since the quantity R cannot be expressed in terms of l and l' explicit from equation 3.29. For this reason one needs to expand the sine function in equation 3.29. Typically the angle $\alpha/2 = \frac{l}{2 \cdot R}$ is small. Hence the expansion of the sine in a Taylor series should be performed around zero. Restricted to the third term of the series one obtains the following:

$$l' = 2R \sin \alpha/2 \approx 2R\left(\frac{\alpha}{2} - \frac{\alpha^3}{48}\right) = 2R\left(\frac{l}{2 \cdot R} - \frac{l^3}{48 \cdot R^3}\right). \tag{3.34}$$

The analytical solution for R yields

$$R = \pm\sqrt{\frac{l^3}{24(l - l')}}, \tag{3.35}$$

where the negative value of R is neglected as physically meaningless. Hereafter the equation for the relative error of the radius of curvature can be found by:

$$\Delta R/R = \sqrt{\left(\frac{\partial R}{\partial l}\Delta l\right)^2 + \left(\frac{\partial R}{\partial l'}\Delta l'\right)^2}. \tag{3.36}$$

Then the substitution of values l, Δl, l', and $\Delta l'$ in the equation 3.36 after differentiation, gives ΔR. Error of force determination is estimated from linear fits of load and unload regions. Considering the actual example, the relative error for the force is estimated to 2 %. Errors related to the interval l, wire diameter d and interval l' are determined from corresponding TEM-micrographs or video snapshots, respectively. The diameter d, however, is measured in several regions along the nanowire and the mean value with corresponding standard deviation gives the

Test Nr.	Time	l, nm	l', nm	Curvature radius R, nm	Force F, nN	Young's modulus E, GPa
1	18:27:17	515.0 ±0.6	499.9 ±1.3	611 ±28	185 ±2	765 ±121
2	18:33:13	517.1 ±0.6	495.5 ±1.4	513 ±17	87 ±2	212 ±28
3	19:17:7	518.7 ±0.6	497.1 ±1.3	516 ±17	172 ±2	687 ±89
4	19:7:58	524.5 ±0.6	512, 9 ±1.4	718 ±42	159 ±2	1046 ±202

Table 3.2: Summary of the measurements on the sample M7.

error Δd. Absolute errors Δl and $\Delta l'$ are determined as 1 pixel uncertainty when converting to the nm scale. In the example one obtains for the Young's modulus the largest possible relative error:

$$\frac{\Delta E}{E} = 3 \cdot 0.046 + \frac{2\,nN}{185\,nN} + 4\frac{0.9\,nm}{45.7\,nm} + \frac{0.6\,nm}{515.0\,nm} \approx 0.16 \tag{3.37}$$

Young's modulus was calculated also for other load/unload tests. Results of elastic moduli for AFM-tests on sample M7 are summarized in table 3.2. One can see that Young's modulus varies from test to test even for measurements with the same bending radius of curvature R. Reasons for the values dispersion for the sample M7 (as well as for other samples) will be discussed in chapter "Discussion".

3.4.2 Nanowire M1

The nanowire M1 was the first wire which was handled consistently with the developed measuring method. The nanowire overview is shown in figure 3.23(a). Here the substrate is on the right side while the AFM-tip is on the left side of the micrograph. In accordance with the geometrical model presented above, a red line corresponds to the length l. The nanowire bended by maximal displacement corresponding to one of two trials is shown in (b). Here the blue line named l' in the model connects two end points of the wire. Load/unload tests were performed in TEM Philips CM12. Fortunately, the camera used for the video capture does not shrink the image, as it is the case of samples M6 and M7. Thus the video aspect ratio is 1 : 1 and no additional distortions are introduced due to aspect restoring.

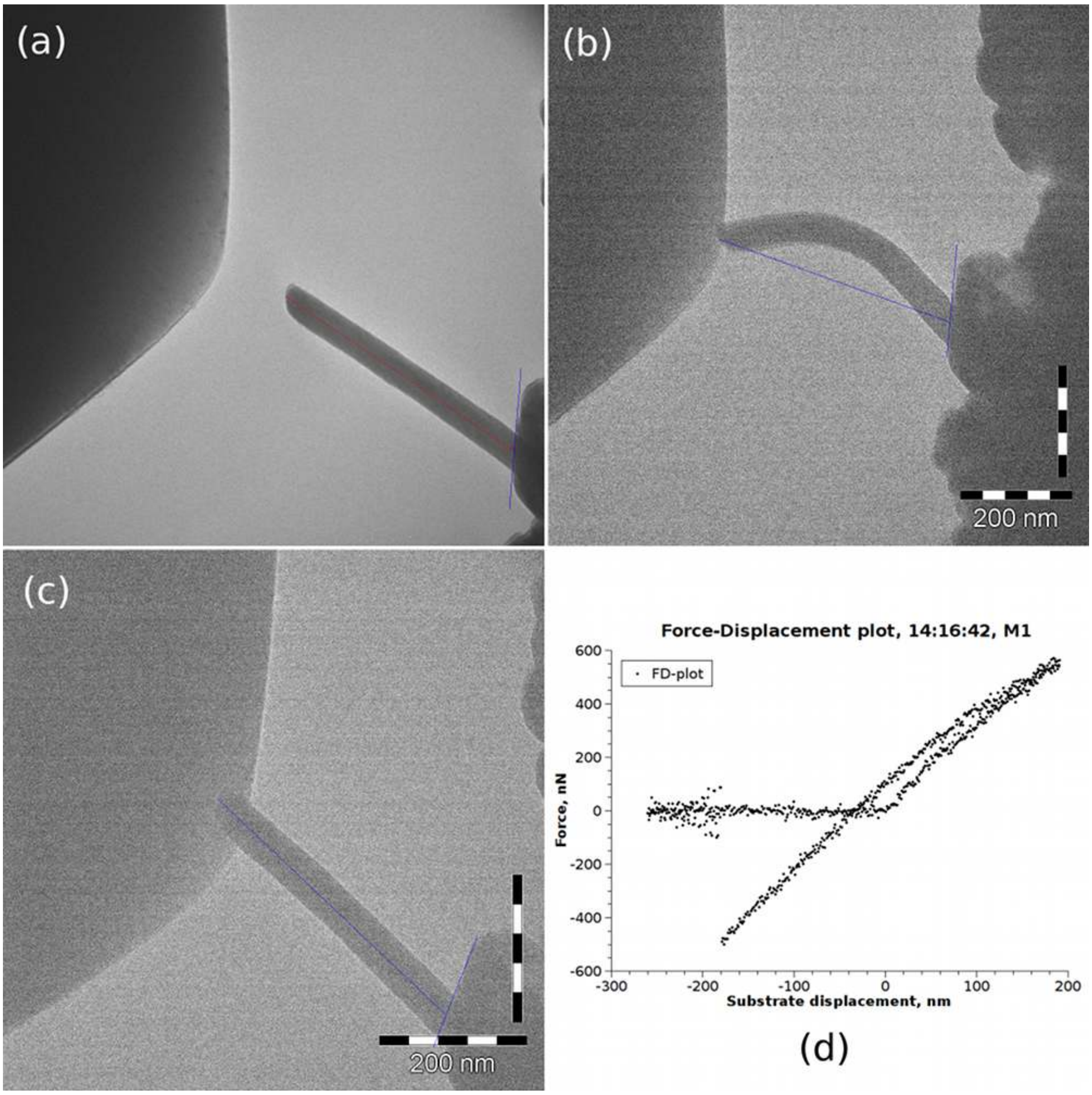

Figure 3.23: (a) The overview of the nanowire M1. The scale of the micrograph (a) is equal to the scale of the snapshot (b), which is taken by the maximal sample displacement during one of the load/unload tests. The snapshot (c) corresponds to another test, where the bending plane is at higher angle to the image plane in comparison to the first case. As a result, the curvature radius in the case (c) appears much larger than in the case (b). The FD-plot of one of the tests is depicted in (d).

The snapshot of the bended nanowire depicted in figure 3.23 (c) was taken by another trial set. The curvature radii of both cases are small and equal to 298 and 283 nm, respectively, but the second radius appears much bigger on the snapshot. The reason is that the bending plane in second case is much more inclined to the image plane than in the first case. The example of the force-displacement plot for wire M1 is shown in figure 3.23 (d).

The results for the nanowire M1 are summarized in table 3.3.

Test Nr.	Time	l, nm	l', nm	Curvature radius R, nm	Force F, nN	Young's modulus E, GPa
1	13:56:3	480.4 ±0.7	424.8 ±0.7	284 ±2	431 ±34	89 ±7
2	14:16:42	497.6 ±1.0	442, 1 ±1.0	299 ±3	546 ±6	129 ±5

Table 3.3: Summarizy of the measurements on the sample M1.

3.4.3 Nanowire M3

The sample M3 is of the type II, as one can see from the HRTEM-micrographs in figure 3.24 (a). Stacking faults along the growth direction can be identified by the visible zig-zag pattern. The overview of the nanowire M3 is shown in figure 3.25 (a). The nanowire has the diameter $56.9 \pm 1.3\,nm$. Example of the video snapshot of the maximal sample displacement can be seen in figure 3.25 (b).

Consider the video snapshot under load. Here the difference of snapshots of M7 and M3 samples is evident (compare for instance figure 3.25 (b) with any of 3.19). This is because in these cases different microscopes with different cameras were used. TEM Philips CM12 was used in the case of measurements on M3 wire. The CCD camera Hamamatsu used in this instrument allows the capture of video but with low frame rate in comparison with high frame rate TV-CCD camera of the newer instrument TEM FEI Technai F20. High frame rate is important if one requires the displacement information during the whole test trial. Concerning our method, the spacial configuration information only at the maximal sample displacement is required. The low frame rate old CCD camera of Philips CM12 TEM instrument gives video snapshots of better quality due to a longer acquisition time for each frame in comparison with TV-CCD camera of TEM FEI Technai F20. It should be noted, that the full acquisition time for a test in that case should be enough large, otherwise the frames might be too distant (in the meaning of time) from the maximal displacement moment.

Figure 3.25 (c) depicts a typical Force-Displacement plot of load/unload tests on the nanowire. As in previous cases, the FD-plot has the individual features. For instance, the non-linearity is observed near the maximal displacement point. These and other issues are considered in chapter ”Discussion”.

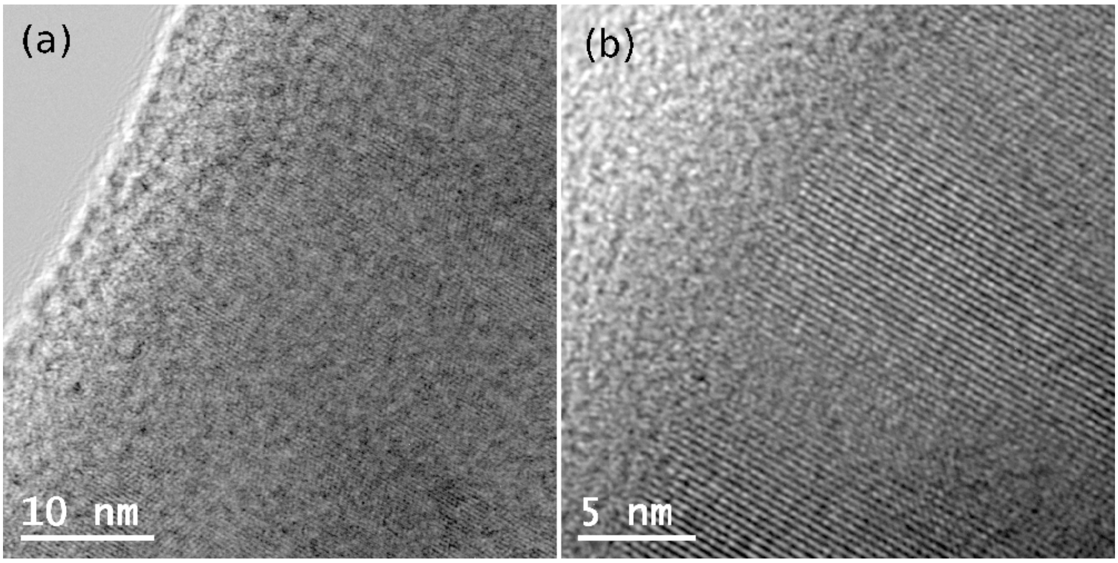

Figure 3.24: HRTEM-images of the nanowire M3. The zig-zag pattern of twinning rotations indicative for type II wires is clearly to distinguish.

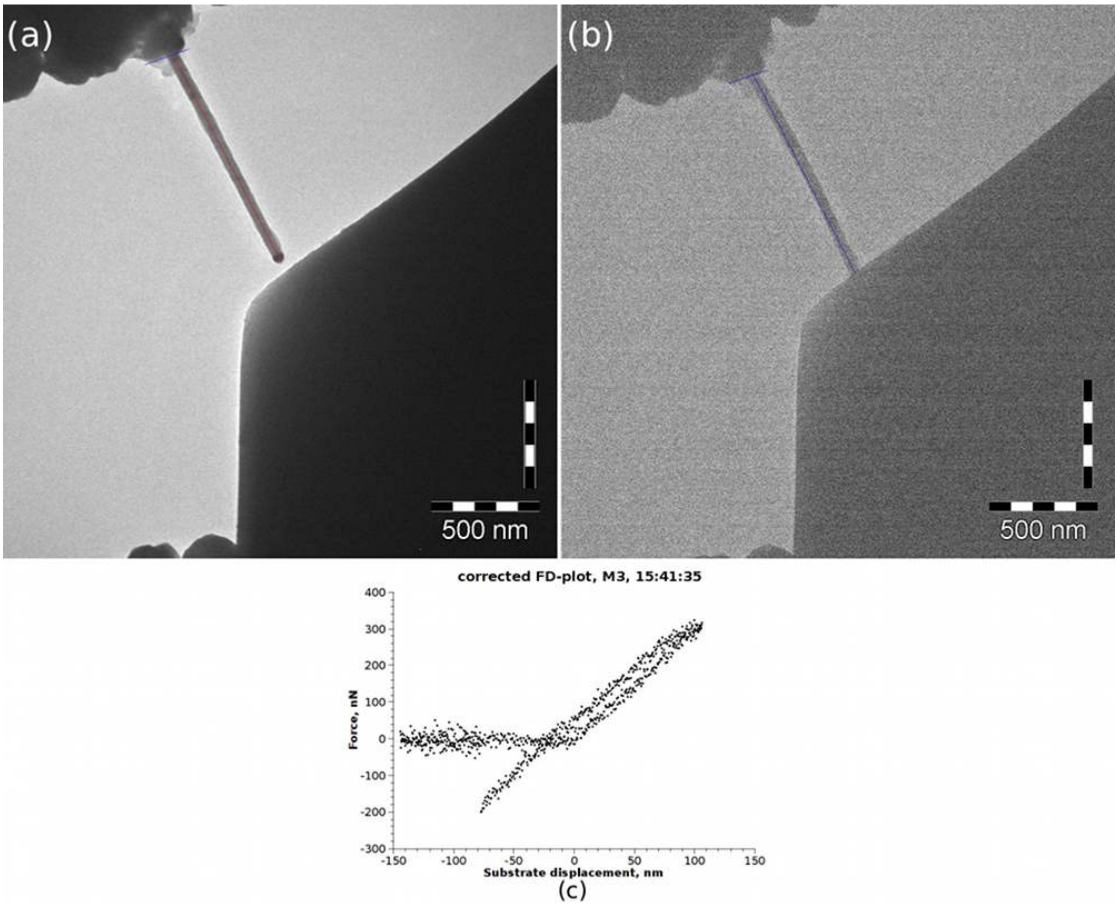

Figure 3.25: TEM-micrographs of the unloaded (a) and loaded (b) nanowire M3. Typical Force-Displacement plot is shown in (c).

Test Nr.	Time	l, nm	l', nm	Curvature radius R, nm	Force F, nN	Young's modulus E, GPa
1	15:41:20	1081.3 ±2.5	1021.0 ±2.5	926 ±25	306 ±2	1415 ±173
2	15:58:10	1078.1 ±2.5	1025.5 ±2.5	989 ±31	322 ±2	1914 ±580

Table 3.4: Summary of measurements on the sample M3.

Unfortunately, as in the case of sample M1 only results of two load/unload tests are presented here since the technique was not completely elaborated by the time of these experiments.

The measurements on M3 are combined in table 3.4.

3.4.4 Nanowire M6

TEM-micrographs of the sample M6 are shown in figure 3.26. At the top of the image one sees the AFM-tip while at the bottom the substrate with the nanowire is imaged. It is immediately clear from the micrograph, that the nanowire M6 is of type III because an Au nanoparticle located with the kink on the wire tip, that is characteristic for type III nanowires.An example of the acquired force-displacement plot is shown in figure 3.26 (c). The plot is already corrected as explained in section 3.4.1. The nanowire has the diameter $83.8 \pm 0.4\,nm$. Figure (b) shows the sample under load.

Summarized results can be seen in table 3.5.

3.4.5 Electron diffraction on sample M6

Selected area electron diffraction analysis was performed on three of four samples. Since the determination of the nanowires type was possible due to the stacking faults pattern, the analysis by means of electron diffraction pattern indexing of two nanowires (M3 and M7) was not performed. However, both diffraction test procedures of the nanowire M6 and the obtained results differ from those of other samples. Thus, for these samples only the selected area diffraction of several regions was acquired while the diffraction analysis during load/unload test was performed

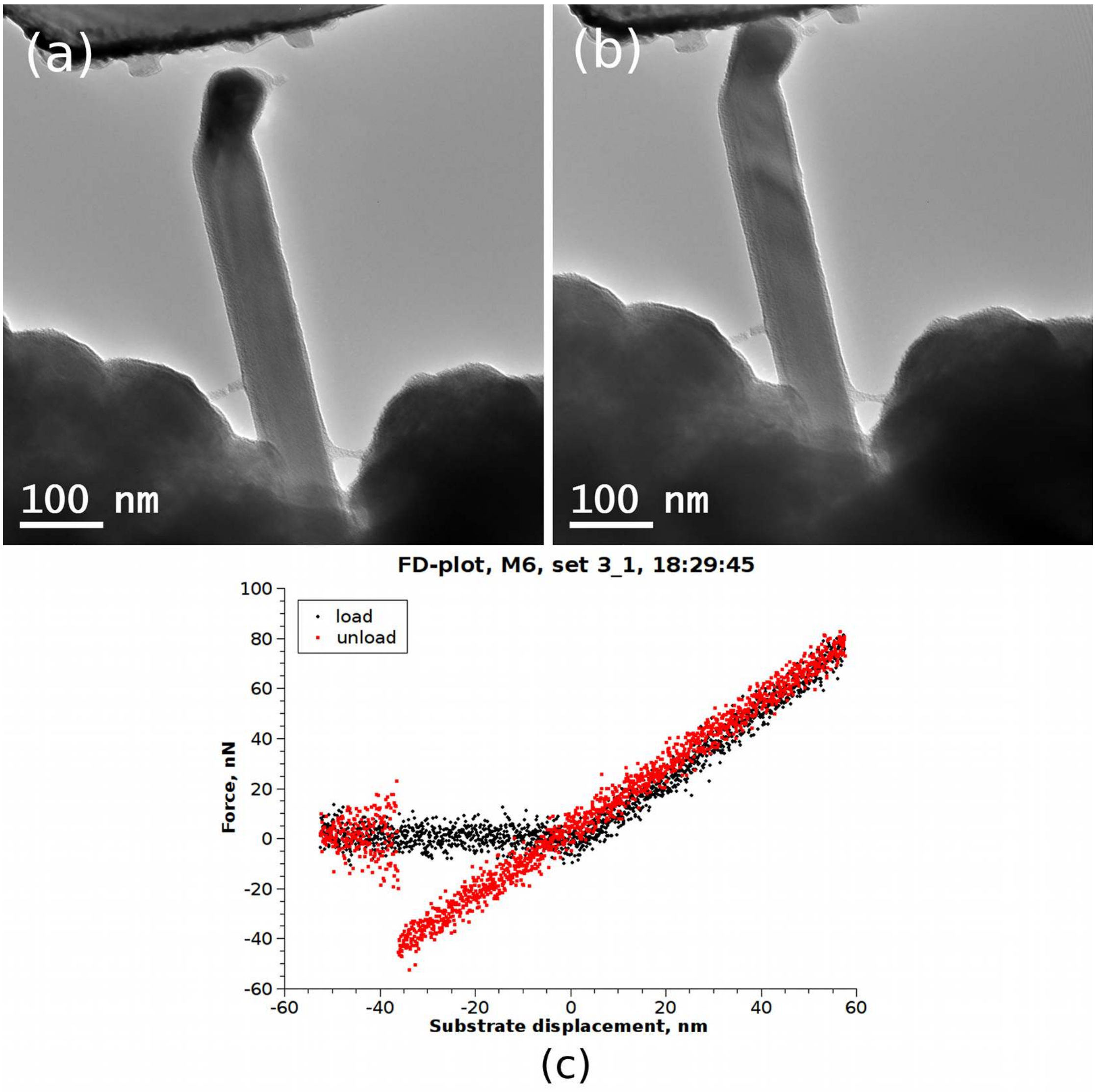

Figure 3.26: TEM-micrographs of the unloaded (a) and loaded (b) sample M6.

in the case of M6 sample. I present the experimental procedure description with results in this section.

Generally, the geometrical arrangement of the AFM-tip/sample system differs from the one described before only in few details as briefly described in the following:

1. Preparation to the AFM-load/unload tests, that implies the adjustment of the sample and the tip in height as well as close approach with the sample to the tip. The acquisition of low magnification TEM micrographs of the sample.
2. Setting the software control value to **Single slope** mode. That means the test is performed only in forward direction in contrast to typical **double slope** experiments. Once the sample substrate has reached the prescribed

Test Nr.	Time	l, nm	l', nm	Curvature radius R, nm	Force F, nN	Young's modulus E, GPa
1	19:45:16	468.9 ±0.6	458.9 ±1.5	651 ±52	101 ±2	49 ±24
2	19:48:21	471.4 ±0.6	463.0 ±1.5	719 ±69	109 ±2	71 ±20
3	19:56:15	471.0 ±0.6	465.4 ±1.5	873 ±123	101 ±2	118 ±49
4	19:59:58	471.9 ±0.6	460.7 ±1.5	623 ±45	164 ±2	70 ±15
5	20:02:42	$472,7$ ±0.6	461.5 ±1.5	625 ±45	212 ±2	90 ±19

Table 3.5: Summary of measurements on the sample M6.

maximal displacement, it stands there. If the test preadjustments are correct, the nanowire is bended. The force-displacement curve is acquired during the procedure.

3. While the nanowire is bent, a selected area diffraction pattern is acquired on the nanowire parts. It is also worth to capture the TEM micrograph of the bent nanowire.

4. One can release the nanowire by interchange of the end and start displacement values in the control software followed by the start of the unload process. And the unload part of Force-Displacement curve is acquired.

The indexed diffraction pattern depicted in figure 3.27 (a) was acquired before AFM-tests. The indexing of the diffraction pattern was performed by the comparison with standard transmission electron diffraction patterns, which may be found in many electron diffraction related textbooks [15]. The procedure implies the comparison of both angles and lengths between reflexes on two diffraction patterns. The standard pattern found is the hcp structure with zone axis $\vec{z} = \left[1\bar{2}1\bar{3}\right]$, which is shown in figure 3.27 (b).

The diffraction pattern which can be used for the determination of the plane normal to the growth direction is shown in the inset of (a). To acquire such a pattern one adjusts the electron beam intensity by converging the electron beam in diffraction TEM mode, so that the shape of the nanowire is observed within the direct diffraction spot due to established special conditions similar to imaging mode. After pattern recording one compares the normal selected area diffraction pattern with this special one. The direction of the nanowire's long axis on the special pattern corresponds to the crystallographic growth direction in normal pattern. Thus, according to the inset of figure (a) the plane normal to the growth direction is $\{0\bar{1}11\}$. It is worth to note, that here one talks about planes, but not about directions. First reason for that is, that diffraction reflexes are stereometrical projections of the reciprocal lattice points and they correspond to crystallographic planes of real space (see section 2.1.3). Second, the notation of crystallographic directions for hexagonal structures does generally not directly correspond to the crystallographic planes notation, as it is the case for cubic structures. According to the inset of figure (a) the plane normal to the growth direction is $\{0\bar{1}11\}$ plane.

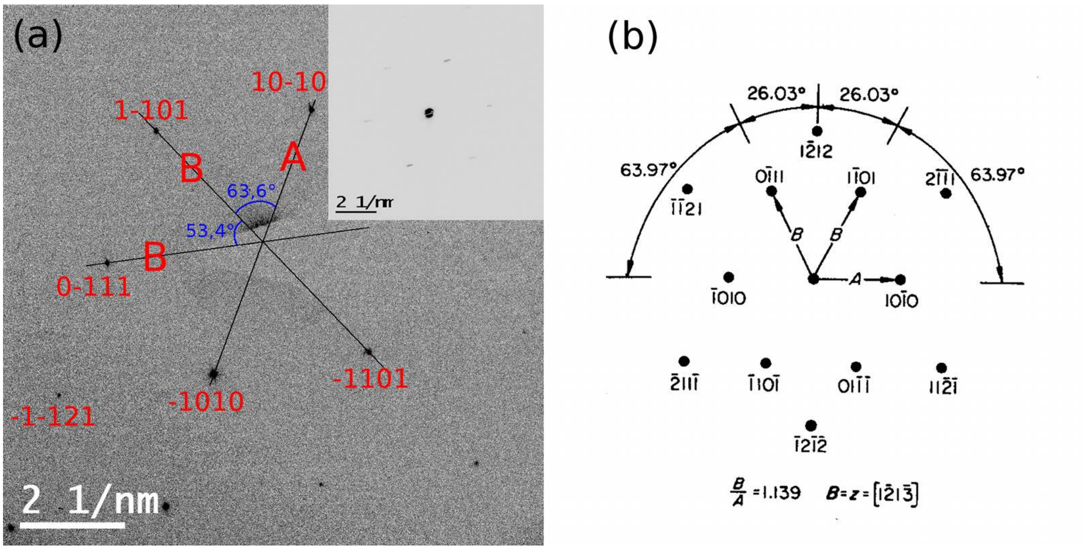

Figure 3.27: (a) Selected area diffraction pattern of M7 nanowire taken from wire's central part. Inset shows the diffraction pattern for determining the crystallographic plane, which is normal to growth direction. (b) One of the standard diffraction patterns of the hcp crystal structure for $[1\bar{2}1\bar{3}]$ zone axis. The pattern is adopted from [15].

Four AFM load/unload tests were performed simultaneously with the acquisition of diffraction patterns of the bent nanowire. Figure 3.28 shows one of the force-displacement plots. Corresponding set of diffraction patterns by different loads is shown nearby. To each diffraction pattern corresponds one individual force-displacement plot. Only one plot is shown here, namely, the one with maximal value of the substrate displacement.

The diffraction patterns differ considerably at different loads. The schematic of the diffraction pattern is shown in the left bottom part of figure 3.28. Lengths denoted by d_i, d_i' between the set of reflexes correspond to nearest and farthest distances of diffraction reflexes, respectively. Indexing $i = 1, 2$ is used to distinguish two set

Pattern Nr.	d_1, nm	d'_1, nm	d_2, nm	d'_2, nm	$d_{max,1}$, nm	$d_{max,2}$, nm
1	0.3688	0.3844	0.3390	0.3400	0.3749	0.3385
2	0.3647	0.3830	0.3410		0.3750	0.3409
3	0.3647	0.3815	0.3264	0.3350	0.3720	0.3318

Table 3.6: Summary of measurements on diffraction patterns on loaded nanowire.

of reflexes: $10\bar{1}0$ and $1\bar{1}01$, respectively. Parameter $d_{max,i}$ is the distance between intensity maxima of diffraction spots, measured by means of line scan on the image. This analysis was performed for three diffraction patterns shown in figure 3.28. One can see that the sizes of spots on pattern (2) are increased in comparison to pattern (1). Moreover, by a larger load (pattern (3)) the broadening of spots appears. The measured broadening angle is equal to 7.6°. The possible explanation of these effects is provided in the chapter ”Discussion”. Results of the analysis are represented in the table 3.6.

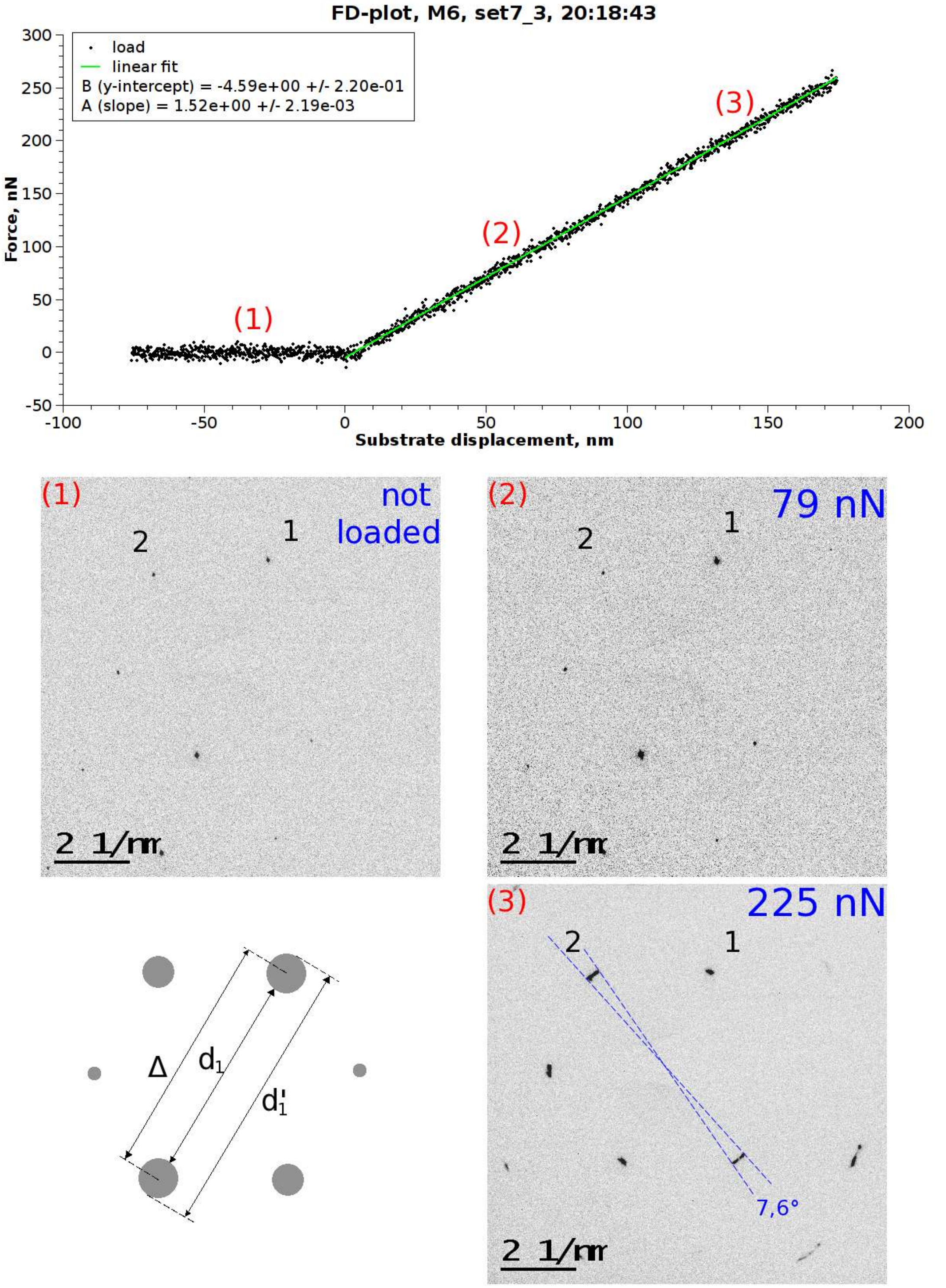

Figure 3.28: A force-displacement plot, recorded by one of the load tests on M7 sample. Diffraction pattern (1) acquired before the test is shown as reference. One can clearly see the diffraction pattern changes by applying the load on the nanowire. Thus, the pattern (2) is acquired at the maximal substrate displacement of 120 μm. Diffraction pattern (3) is recorded by larger maximal substrate displacement (250 μm). There is corresponding values of the measured force on right top corner of patterns.

4 Results and discussion

In this work two types of InAs nanowires with same planar defects of different orientations were studied. In type II nanowires planar defects are perpendicular to nanowire growth direction while in type III they are oriented along nanowire growth direction. Young's moduli of four nanowires using ”bending method” were determined. In this chapter final results are presented and discussed. Also an outlook on the method reliability and on a possible improvement is provided.

Elastic properties of InAs nanowires

Results are summarized in table 4.1. Here, only mean values of determined elasticity modulus for each sample and selected values of nanowire length, l, bisecant length l', and nanowire diameter d from one of the tests for one sample are shown. A quantity $\triangle \equiv l - l'$ is also shown in the table. General error of the averaged Young's modulus is calculated as follows:

$$\Delta\overline{E} = \sqrt{\sigma_{\overline{E}}^2 + \frac{1}{n(n-1)}\sum_{i=1}^{n}(\Delta E_i)^2}, \tag{4.1}$$

where $\sigma_{\overline{E}}$ is the standard deviation of the mean value $\overline{E}$ averaged from n measured values E_i for each nanowire. ΔE_i is an absolute error of a corresponding value E_i. This absolute error is calculated according the error propagation given by equation 3.33 on the page 67.

According to evaluated data the values of Young's modulus of type II nanowires ($\langle 111 \rangle$ growth direction) are in large excess over the bulk value of $97\,GPa$ calculated for mixed structure ZB along $\langle 111 \rangle$[27]. The comparison with Young's modulus values of multiple measurements obtained in [27] and [24] are smaller by one order than values found in this work. Because of large difference between both calculated bulk value and values found in literature the result obtained in this work for type II nanowires can be more likely interpreted as overestimated because of

NW type	length l, nm	length l', nm	$\triangle = l - l'$, nm	Nanowire diameter d, nm	**Young's modulus E, GPa**	Relative error $\Delta E/E$
Type II M7	515.0 ±0.6	499.9 ±1.3	15.1	45.7 ±0.9	**678** **±189**	27.9%
Type II M3	1081.3 ±2.5	1021.0 ±2.5	60.3	56.9 ±1.3	**1665** **±496**	29.8%
Type III M1	480.4 ±0.7	424.8 ±0.7	55.6	55.2 ±0.3	**109** **±21**	19.3%
Type III M6	472.7 ±0.6	461.5 ±1.5	11.2	83.8 ±0.4	**80** **±18**	22.5%

Table 4.1: Summary table for four measured InAs nanowires.

following reason. Young's modulus E of the nanowire is dependend on the nanowire diameter d as $E \propto d^{-4}$ (see equation 2.22). Hence, the small changes in value d produce large changes of value E. The overestimation of Young's modulus can be caused most probably by the underestimation of nanowire diameter d as will be explained later. This considerable underestimation is possible only in case of type II nanowire, since it has truncated triangle cross-section, by which the determination of diameter d is complicated. Nevertheless, some solutions are proposed for more precise determination of diameter d of type II InAs in order to refine the reliability of used method towards type II semiconductor nanowires.

Let us consider now the evaluated E-modulus of the typ III InAs nanowires. The nanowires of type III have circular cross section which simplify diameter measurements. Hence, the diameter underestimation is much less probable. Figure 4.1 shows dependence Young's moduli of type III InAs nanowires on nanowire's diameter. Black rectangular-shaped points refer to Young's moduli found by the electromechanical resonance method [27] while red circular-shaped points correspond to values obtained in this work. Young's modulus is increased in comparison with the bulk value for nanowires of diameters ranging from 30 nm up to 90 nm. Non-monotonic diameter dependence of Young's modulus dependence with a maximum at 50 nm is observed. This non-monotonic dependence can be hardly explained by surface contribution to the nanowire elasticity. The planar defects seem to influence Young's modulus of InAs nanowires. It is known that InAs nanowires with diameter less than 30 nm have a WZ structure while InAs wires with diameters above $80 - 100\,nm$ posess a cubic ZB structure typical for the bulk InAs [11]. Nanowires of "transition diameter" range between 30 nm and 80 nm show often a mixed ZB-Wz type of structure full with stacking fault defects. Density of these planar defects is different for different nanowires and especially increased for the nanowires of 50 nm diameter. It seem to be an additional evidence that the planar stacking fault defects increase elasticity of InAs nanowires.

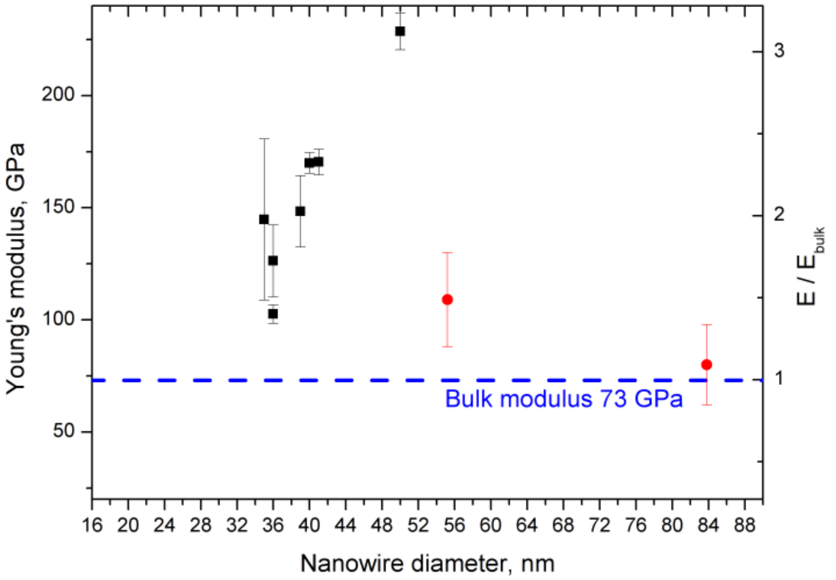

Figure 4.1: Young's modulus dependence of type III InAs nanowires on diameter. Black rectangular-shaped measurement points correspond to electromechanical resonance method [27], whereas red circular-shaped points originate from measurements by bending method used in this work.

Discussion of error values

One of the requirements for the reliability of the measuring method is that it gives adequately small error of physical quantities. Hence, the finding and analysis of error sources are important for the method characterization. The generalized error value is a geometrical sum of statistical errors of several measurements on each wire and errors of indirect measurements (see equation 4.1). Considering only errors of indirect measurements (i.e. disregarding statistical errors), values $\Delta E/E$ for M6 and M7 samples are almost always larger than these for M1 and M3. For instance, relative errors of elasticity modulus of M1 are in the range of 4%-8% while in the case of M6 the relative error is between 21% and 49% (refer to summary tables 3.3 and 3.5). To understand the reason for large errors, let us consider figure 4.2. The diagram (a) shows dependence of calculated curvature radius R as a function of the difference $\triangle$ between the measured nanowire length l and bisecant length l' (see figure 3.20 on page 63) by keeping l' constant and varying l as a parameter. Corresponding derivative of the curvature radius as a function of $\triangle = l - l'$ is shown in figure 4.2 (b). Measurements data for nanowire M6 was used to calculate R and plot these two diagrams.

According to diagrams one can conclude, that if the lengths l and l' are close to each other or, more concrete, $\triangle$ is smaller than app. $3\,nm$, the error ΔR becomes large. Indeed, the equation for error ΔR (see expression 3.36 on the page 67) contains partial derivatives of radius R with respect to l and l'. The derivation of R leads to the high order hyperbolic dependence of error $\Delta R/R$ on the quantity $\triangle$, and as a result giving large error values at small values of $\triangle$. Moreover, for the estimation of Young's modulus' error one has to triple the error (as follows from error propagation 3.33). Thus, the Young's modulus' error is highly governed by quantity $\triangle = l - l'$.

Let us consider now the direct measurements. The errors originate essentially from the measurements of the nanowire diameter d, nanowire length l, and bisecant length l'. In this work, these measurements were performed directly from TEM micrographs or video still images (refer to section 3.4.1 for details). In these direct measurements, errors are equal to size of 1 image pixel. Generally, the pixel size at micrograph (the size of 1 pixel in nm) is less than that of a snapshot. Moreover, video still images appear very noisy in comparison to micrographs. Therefore sometimes it is difficult to say, where the boundary of the nanowire is on the snapshot. Thus the error of l' estimated from video snapshots is typically larger than that estimated from the TEM imaging.

According to equation 3.36 the relative error of the diameter is four times included in the general error ΔE. In most cases it was possible to measure the diameter many times along the whole length of the nanowire. Multiple measurements reduce the error of diameter determination significantly. Here one faces another issue. In the case of round cross section the diameter of the wire is definitely the width of the wire projection. The width of projection for a type II nanowire depends on position of wire relative to the electron beam since the cross-section of type II nanowires is a truncated triangle. Indeed, there are two extreme cases of the projection widths. According figure 4.3 a minimal width of the projection, which corresponds to the "diameter" d used in Young's modulus calculations, is given by d_1. The width of the second projection of the wire can be easily found geometrically that is shown on the right in figure 4.3. It is given by $d_2 = d_1/\cos\frac{\pi}{6}$. The quotient $\frac{d_2}{d_1} = \frac{2}{\sqrt{3}}$ shows,

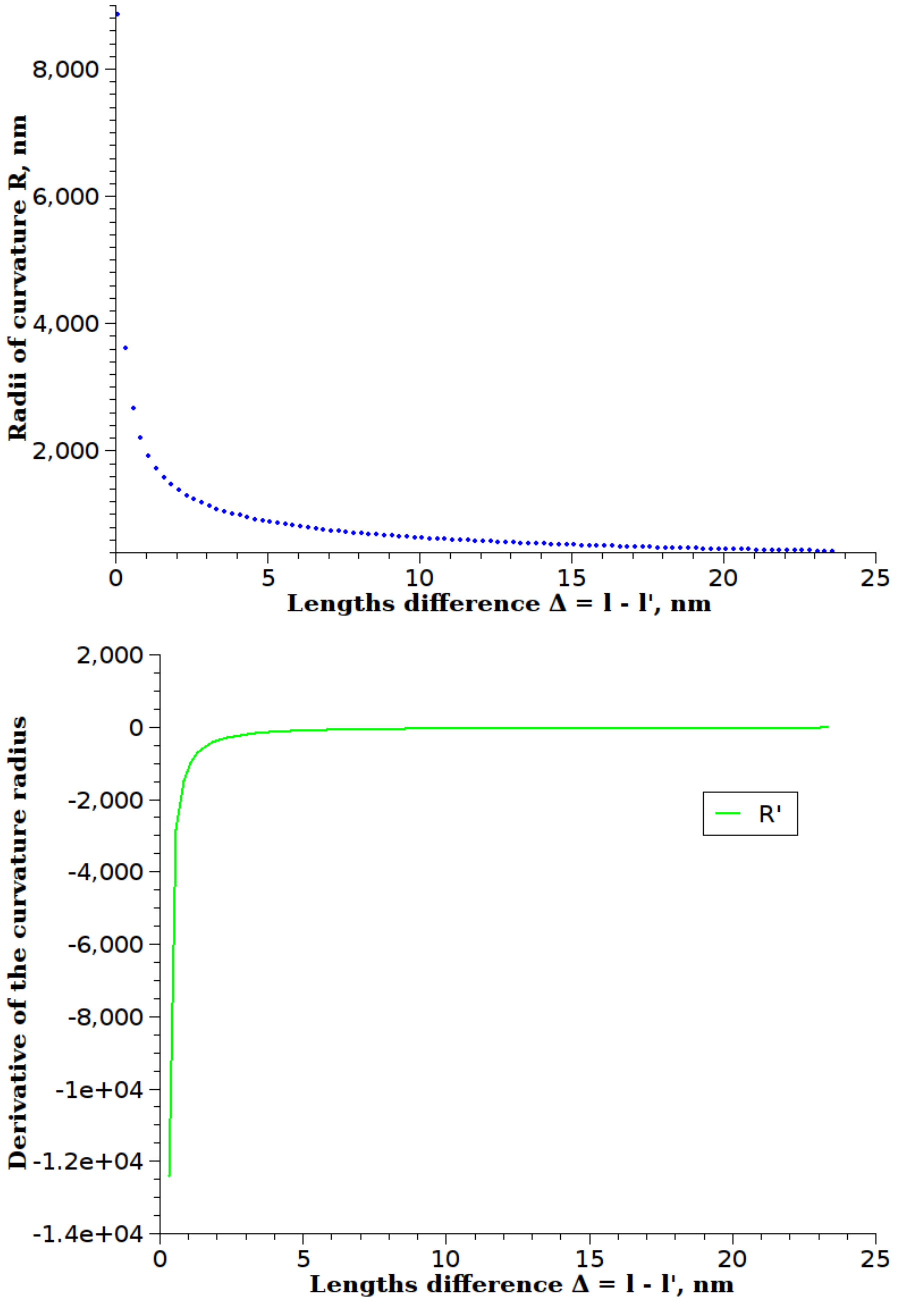

Figure 4.2: (a) Behavior of the curvature radius as a function of the difference $\triangle = l - l'$. (b) The derivative of the plot (a) with respect to curvature radius. Points of the plot (a) are calculated by means of equation 3.35. Herewith, the length l' remains constant while the length l is variating.

that the measured "diameter" of the wire with truncated triangle cross section can vary up to 15 %.

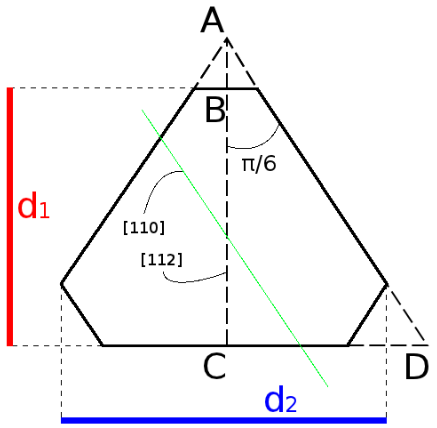

$$AB/AC = 0.2;$$

$$AD = \frac{AC}{\cos\pi/6} = \frac{d_1}{0.8\cdot\cos\frac{\pi}{6}};$$

$$d_2 = AD - \frac{AB}{\cos\frac{\pi}{6}} = \frac{d_1}{0.8\cdot\cos\frac{\pi}{6}} - $$
$$- 0.2\frac{d_1}{0.8\cdot\cos\frac{\pi}{6}} = \frac{d_1}{\cos\pi/6}.$$

Figure 4.3: Left: schematic of a cross section of type II InAs nanowires. The cross section of the nanowire is a truncated triangle with truncation ratio $r = \frac{AB}{AC} = 0.2$. Red and blue lines denote widths of two extreme projections d_1 and d_2 to the plane of a TEM micrograph, so that the relation $d_1 \leq d \leq d_2$ is true. Right: the derivation of the relation between extreme widths d_1 and d_2 is presented.

Another one uncertainty arises from the measurements of the force acting on the nanowire during bending. The ideal geometry of an AFM-test shown in figure 3.14 on the page 55 implies, that the cantilever is perpendicular to the nanowire (or, equivalently, sample holder tilt axis is parallel to the nanowire long axis). In experiment it can hardly be achieved. The geometry typically observed in experiment is showed in figure 4.4. There is likely an angle $\pi/2 - \alpha$ between the nanowire long axis and the cantilever front surface, which is not equal to 90 °. The sensing capability of the AFM-sensor, however, is specified in the direction which coincides with sample holder tilt axis. Therefore only the perpendicular component $F_\perp$ of the force acting on the nanowire is measured. This is one of the main drawbacks of our measurement technique. Let us call this issue the ”force determination problem”.

In this work the measured force was not analyzed in components, since it requires the recording of low magnification TEM micrographs in order to visualize the nanowire and the cantilever front/back surface in one micrograph. Very often it can not be done due to disturbing charge effects. In fact, there is a charge on the sample holder parts due to beam illumination resulting in non-homogeneous static electrical field around elements of the sample holder. In certain configurations electron beam can be strongly deflected by this local field, that may distort the low magnification image. A remarkable fact is that this strong image distortion occurs in low magnification (M or LM) TEM modes, whereas imaging by higher magnification mode (SA mode) lens current configuration is distorted minimally. The reason is that in low magnification M and LM modes the illumination conditions of the sample are such, that the electron beam intensity is higher, which produce intenser disturbing charge effect.

The ways to improve used bending method

From considerations mentioned in previous section the following can be concluded for the application of discussed method:

1. It is important to pay careful attention to the determination of the second moment of area of type II nanowires. Because of the peculiar cross section of type II nanowires, an additional error in determination of the second moment of area and the diameter can occur. Therefore to improve the current approach one can use the following method to measure the diameter.

   The method is based on the determination of the orientation of the nanowire with respect to the electron beam. Hereafter, one should bring the nanowire in the $\langle 110\rangle$ zone axis to make possible the measurement of diameter d_1 (see figure 4.3). The electron diffraction of the nanowire can give complete information about current nanowire orientation. Also this information can be obtained without the acquisition of a diffraction pattern. Instead of that, one can take into account the effect of rotational twinning in type II nanowires with growth direction $\langle 111\rangle$. If one looks along the $\langle 110\rangle$ zone axis, then according to [26] one observes the zig-zag pattern of rotation twin defects as depicted in figure 2.13 (d) on page 32 or a stripe-like pattern by low magnification TEM (see figure 3.15 (d) on page 57). Planes $\{112\}$ are distinct facets of type II nanowires as shown in figure 4.3. If one rotates the nanowire 30° around the $\langle 111\rangle$ growth direction then the zone axis turns to $\langle 112\rangle$ and no more stacking faults pattern is observed. Hence, the crystallographic direction $\langle 110\rangle$ and corresponding crystallographic planes $\{110\}$ can serve as reference directions. Thus, if one pronouncedly observes the pattern of stacking faults or observes the diffraction pattern, which corresponds to $\langle 110\rangle$ direction, then the wire is oriented along the $\langle 110\rangle$ zone axis, and the diameter d_1 is equal to the width of the two-dimensional projection.

2. Force measurements should be performed with regard to the fact that the AFM-cantilever is calibrated to measure the components only normal to the sample holder tilt axis. By several geometrical configurations of the beam and parts of the sample holder it is possible to perform the low magnification

imaging without strong image distortions. Measurement at low magnification is required to image the nanowire and cantilever edge at the same TEM-micrograph. Typically this imaging succeeds when the electron beam is far from the holder parts, so that the nanowire is somewhere near to the holder tilt axis. As discussed earlier in this case one should measure the angle α between the projection of cantilever edge (which is normal to sample holder tilt axis) and nanowire long axis to extract the full acting force using the simple equation $|\vec{F}| = |\vec{F_{\perp}}|/sin\alpha$ in accordance with figure 4.4.

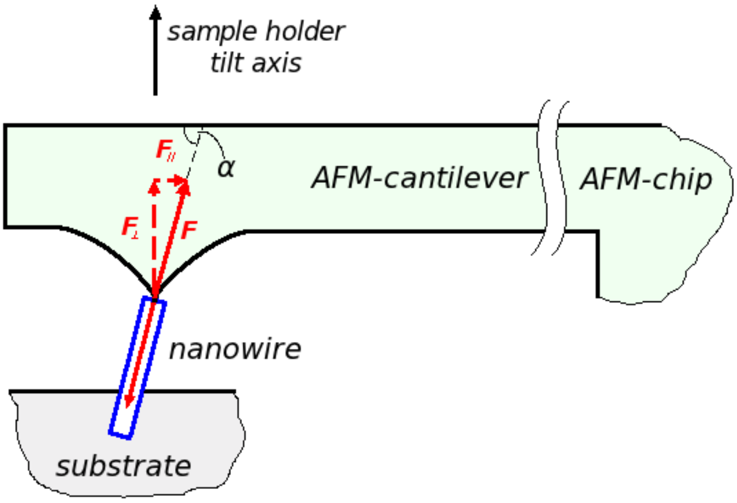

Figure 4.4: Schematic of the low magnification TEM image for determination of full force acting on the nanowire during AFM-test.

3. Figure 3.20 on page 63 depicts the bent nanowire lying in the image plane. The dispersion of radius R of curvature and, consequently, E-modulus are caused essentially by uncertainty of bisecant value l' and nanowire length l. This problem can be minimized using longer nanowires. In fact, from geometrical considerations the longer is the wire, the larger is the quantity $\triangle = l - l'$ for the same load. It results in smaller relative errors of l and l' and more confident Young's modulus values in the sense of error.

4. Since Young's modulus error is very strong depend on quantity $\triangle = l - l'$, the method of measurement of length l' should be revised. Thus, the length l' is measured in this work, almost without exception, from video snapshots, recorded by maximal sample displacement. Unfortunately video capturing device used in conjunction with FEI Tecnai F20 TEM instrument performs the stretching of video signal. Therefore the reconstruction of natural aspect ratio is required for each snapshot as it described in section 3.4.1. Moreover, as discussed earlier the quality of snapshots is not sufficient enough to result in

measurement values with small error. For this reason it would be recommended to measure the length l' on the TEM-micrographs acquired by maximal sample displacement instead of video snapshots which can drastically diminish the measuring uncertainty and, therefore, increase the method reliability.

5. To minimize the image distortion introduced by charge effects by TEM low magnification imaging, it is recommended to use the objective aperture during the imaging, which reduce charge effects. Furthermore, one can engineer discharge mechanisms in the sample holder setup.

Non-linearity and other features of experimental force-displacement curves.

Since the force-displacement plots are used to extract the acting force, they play a key role in the work. Hence, it is required to understand effects, which can undesirably influence measured forces. Even after correction procedure described in section 3.4.1 the typical FD-plot has a complicated form which differs from an simulated one (see figure 2.5 on page 23). Possible reasons for this discrepancy and how it can influence measured force values are analyzed here.

Experimental FD-plots shows typically hysteresis: load and unload curves are not coincide. Therefore, slopes of linear approximation calculated for forward (load) and backward (unload) regions are not equal, i.e. for the same substrate displacement the force on backward curve appears to be larger than on the forward curve. This hysteresis actually does not influence our results since load/unload curves are coincide at the maximal sample displacement and corresponding force value is taken for further calculations. The physical reasons for the experimentally observed hysteresis will be discussed later together with non-linearity effects.

The load/unload regions of experimental FD-plots are non-linear. Only in narrow region of sample displacement the FD-curve can be regarded as a linear. Let us estimate the value of ”linearity range” as follows. A FD-plot of a load/unload test is shown in figure 4.5 (a). One splits the load/unload regimes in regions of equal length and performs the linear approximation on set of points for each region. Resulting slopes of regions are shown in figure 4.5 (b) as a function of substrate displacement. As one can see at substrate displacements ranging from 0 up to $80\,nm$ the values of calculated slopes are equal within error bars. That means within this region the FD-plot is approximately linear.

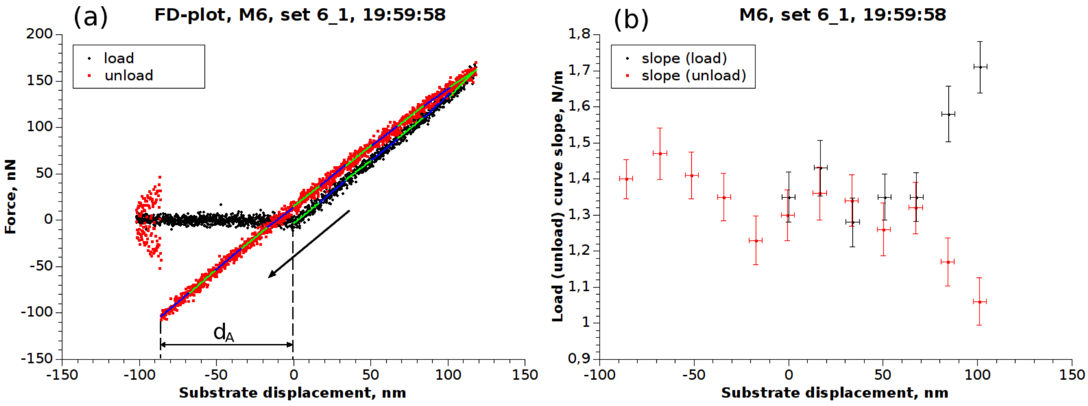

Figure 4.5: (a) A force-displacement plot. Load/unload parts are approximated with set of fragments of linear approximation fit. (b) Slopes of fragments as function of substrate displacement are shown.

The choice of another sampling interval may cause broadening or narrowing of linear range. On the other hand, very small or very large sampling interval results in non-reliability of the estimation. Small sampling interval gives rise to large statistical error due to the small number of measured points involved in the calculation. While a very large sampling interval produces too few points to make a conclusion about the value of linearity range. For samples M6 and M7, the linearity range of $(35 \pm 11)\,nm$ is estimated from analysis of 13 times repeated FD-plot measurements.

The non-linearity of FD-curves is a complex feature, which has number of reasons. The hysteresis effect mentioned above is closely related to the non-linearity of the FD-curve, so that reasons of these features can not be treated separately. Possible reasons for hysteresis and non-linearity of FD-curves are following.

1. Interface effects between the nanowire and AFM-tip may play an important role. It is known, due to decomposition of residual gases an electron beam irradiation in TEM generates contaminations (mostly carbon). Moreover, the electron beam illumination can lead to amorphization of a surface of InAs nanowire, that degrades its mechanical properties. Besides that, contaminations on the nanowire might be deposited during sample preparation by dielectrophoresis. Thus, the surface of the AFM-tip and nanowire are always covered with amorphous layers of decomposition and amorphization products. Since the nanowire and AFM-tip during the load/unload test are in mechanical contact, amorphous interface is involved in force response. Indeed, the nanowire tip can be pressed into the amorphous layer during load resulting non-linearity of the curve.

2. Heating of the nanowires during bending can lead to non-linearity of FD-curves. Temperature dependence of Young's modulus gives rise to force response resulting in deviation of force-displacement dependence from linear regime.

3. For the actual understanding, however, all reasons listed above are not significant in comparison with the following one. This reason referred as "force determination problem" was already discussed earlier. Therefore, only the influence of this problem on experimental FD-plots will be pointed out. Consider the bending of the nanowire during the AFM-test (see figure 4.8). The nanowire bended with the AFM-tip directs the full releasing force generally not in the sensing direction of the AFM-cantilever. Hence, only the component of the force is detected. Increasing displacement results in higher load and the force direction changes. The higher is the load, the smaller is the curvature radius so that the angle of nanowire inclination α increases (see 4.4). Then, even if the total force response $\vec{F}$ of the nanowire would be linear, the detected component $\vec{F_\perp}$ becomes smaller since angle α is increased. This can be the main reason for observed non-linearity at high loads.

An interesting effect is observed when one consider the whole set of recorded FD-plots for a particular nanowire. Consider the unload part of FD-plot depicted in figure 4.5 (a). The sample is displaced backwards through the point of zero force as denoted with the arrow. Change of force sign in unload curve corresponds to the transition between repulsive and attractive forces acting in nanowire-tip system. Let us call the *detaching displacement* the distance d_A on displacement axis between the point of contact ($d = 0$) and point where the cantilever looses contact with nanowire. As noted in section 2.2.3 in this region of FD-plot the cantilever undergoes attractive adhesive forces between the nanowire and the tip. For each sample the set of measurements with increasing sample displacement are carried out. Dependences of detaching displacement d_A on the maximal sample displacement after contact event for nanowire M6 and M7 are shown in figure 4.6.

Detaching displacement icreases with increasing load. Hence, the quantity d_A is a measure of the efficiency of adhesion between the nanowire and the tip. The adhesion depends on the contact area. Load/unload tests at higher loads produce deeper imprinting of amorphous layers of the nanowire and AFM-tip in each other. As a result, the stronger adhesion will be established and therefore the rip-off of the AFM-tip will occur at higher detaching displacement. It confirms that possible

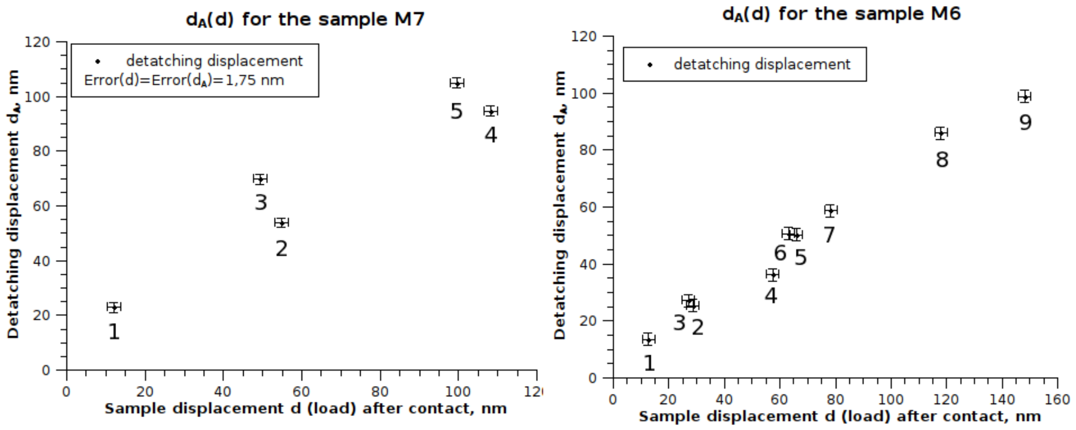

Figure 4.6: Dependences of detatching displacement d_A on the maximal sample displacement d for two nanowires. Numbers under experimental points denote the sequentional number of a measurement.

reason for non-linearity of FD-plot and their hysteresis is the change of interface between AFM-tip and nanowires.

Diffraction patterns of objects under mechanical load

Individual InAs nanowire of Type III was bent forming arcs with different radius which depends on applied forces. Bending cause atomic level strains along both radial and axial directions which manifest themselves in changing electron diffraction patterns (see figure 4.7).

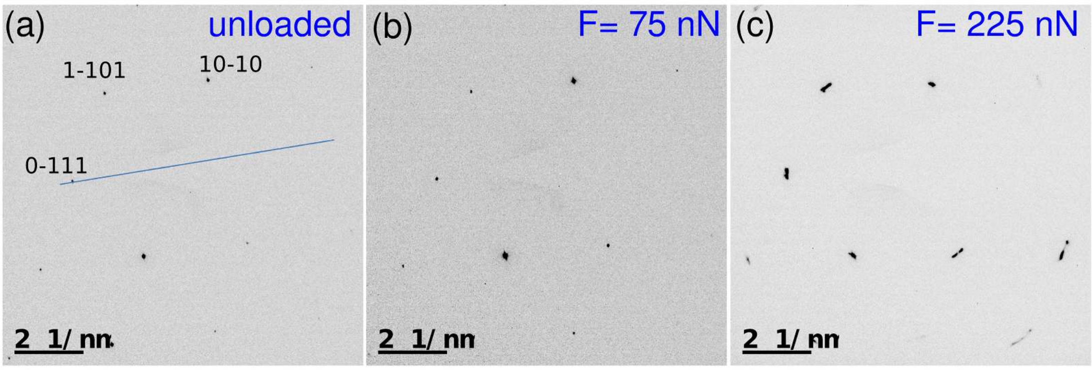

Figure 4.7: Selected area electron diffraction patterns of InAs nanowire: unloaded (a), loaded with 75 nN (b), and loaded with 225 nN (c). The pattern is indexed corresponding to hexagonal crystal symmetry along [111] zone axis. The nanowire growth direction is shown with dashed line in (a).

Regular electron diffraction pattern of fcc structure along [111] zone axis consist of three sets of $\{220\}$ reflexes with 6-fold symmetry. One aspect concerning electron diffraction should be mentioned here: type III InAs nanowire oriented with its [111] zone axis parallel to the electron beam shows an electron diffraction pattern which does not correspond to the cubic ZB structure of the wire. The reason is that by recording of electron diffraction along [111] zone axis the electron beam direction is perpendicular to the stacking fault planes. Variation of stacking order and distortion of cubic symmetry in the crystal lead to changes in electron diffraction pattern. Similar phenomena was observed by in Ag or Ag plate-like crystals [17],[20]. The electron diffraction pattern of type III InAs nanowires with a cubic ZB crystal structure and stacking faults parallel to the $\langle 121 \rangle$ growth direction looks very more like one corresponding to the electron diffraction of hcp crystal in $[1\bar{2}13]$ direction (see figure 4.7 or figure 3.27 on page 75).

Obvious changes in the diffraction patterns are observed when the nanowire undergoes mechanical load. Application of a force of $75\,nN$ leads to uniform broadening of $(10\bar{1}0)$ diffraction spot as shown in figure 4.7 (b) while the distance between the diffraction spots which are opposite to the origin does not change. It is interesting that the diffraction spots corresponding to $\{0111\}$ planes almost do not change. The diffraction pattern changes considerably if one increases the applied force up to $225\,nN$ (see figure 4.7 (c)). The intensity maxima of the opposite spots slightly shift towards each other. Now the broadening of diffraction spots occurs in directions perpendicular to lines which connect the opposite reflexes so that spreading angles can be measured.

One can propose the following model for observed phenomena. Bending of the nanowire leads to a local change in atomic position along both radial and axial directions. Tensile strains $+\delta$ appear at the upper part of the nanowire while contractive strains $-\delta$ are present at the lower part as schematically depicted in figure 4.8. These strains that are actually spread in interplane distances result in broadening of electron diffraction spots in radial direction (see figure 4.7 (b)). Since the strains are non-uniform (from $-\delta$ up to $+\delta$) in the direction perpendicular to the nanowire axis, an effective angle β between the atomic planes appears. That will manifest itself as angular splitting (or azimuthally spread) of corresponding diffraction spots (see figure 4.7 (c)). Quantitative analysis of the recorded electron diffraction patterns for evaluation of strains is possible but quite complicated. It requires simulation of electron diffraction patterns for a specifically deformed crystal structure. Theoretical modeling and computation are required.

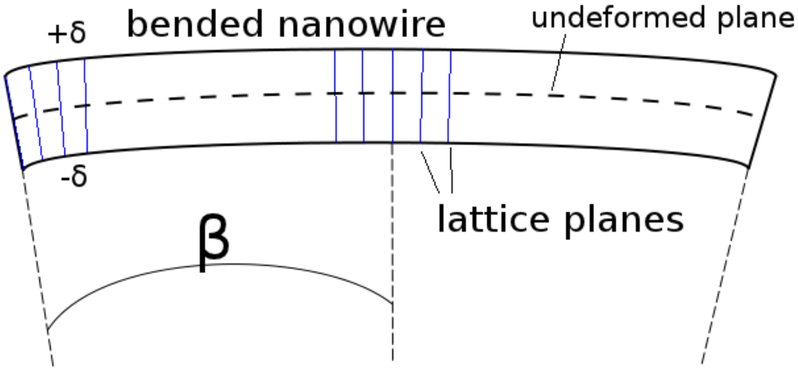

Figure 4.8: Schematic two-dimensional model of the bended nanowire. Atomic lattice planes are shown in blue. Quantities $\pm\delta$ denote the tensile and contractive strains, respectively. Angle β is an angle between the atomic planes.

5 Summary and conclusions

In this work the study of mechanical properties of InAs nanowires was performed. Measurements were carried out using a special commercial atomic force microscope (AFM) *in situ* in transmission electron microscope (TEM). It allows static contact load/unload measurements with the capability of sensing nanonewton forces. This special sample holder gives unique possibility to measure mechanical properties of samples simultaneously with their atomic structure by high-resolution TEM (HR-TEM) or electron diffraction.

Nanowires were grown from catalytic Au nanoparticles using metal-organic vapor phase epitaxy (MOVPE). The InAs (001)B bulk was used as a substrate. The growth of single crystal nanowires occurs in three different crystallographic directions. According to this the classification is following: Type I nanowires with no planar defects and growth direction $\langle 001 \rangle$, type II nanowires with stacking faults defects perpendicular to growth direction $\langle 111 \rangle$, and type III with stacking faults defects along the growth direction $\langle 112 \rangle$. A special method based on dielectrophoretic alignment of InAs nanowires was developed for fabrication of samples suitable for AFM measurements *in situ* in TEM. This method can be extended to other semiconductor materials. Samples prepared with this method allow the observation of electron diffraction or HR-TEM of radial and axial atomic strains during nanowire bending.

Mechanical testing of InAs nanowires of two types (type II and type III of growth direction $\langle 111 \rangle$ and $\langle 112 \rangle$, respectively) was performed by bending of nanowires and measuring the force. Video capture during the load/unload testing and recording of TEM-micrographs allows to extract geometrical parameters of the nanowire, such as length, diameter, and bending curvature radius. In conjunction with the measured force and the geometrical parameters of the wire the calculation of Young's modulus was performed. For Type III nanowires ($\langle 111 \rangle$ growth direction with stacking faults) measurements show the enhancement of Young's modulus ($80\,GPa$ for diameter $84\,nm$ wire and $109\,GPa$ for $55\,nm$ wire) in comparison with the calculated bulk InAs elasticity modulus ($73\,GPa$ in $\langle 111 \rangle$). On the basis of Young's modulus values obtained in this work and values from [27] its dependence on the nanowire diameter can be explained as generally governed by planar defects density. In fact, this non-monotonic dependence has a maximum at $50\,nm$ where the stacking faults density is supposed to be the largest.

Mechanical testing of Type II nanowires (growth direction, stacking faults perpendicular to growth direction) results in overestimating Young's modulus. Measured values (app. $600 - 1700\,GPa$) are an order of magnitude larger than the bulk value ($93\,GPa$ in $\langle 111 \rangle$ direction). It is believed that the overestimation is caused by uncertainties in wire's diameter evaluation. However, ideas to the method suggested, which would minimize the uncertainty. After applying the suggested improvements the measurments of Young's modulus by the "AFM-bending method" are expected to be reliable and have a small error.

Besides that, selected area electron diffraction patterns of a bent nanowire of Type III at different load values was recorded. Broadening of diffraction spots in a peculiar way is observed for small load ($75\,nN$) as well as for larger load ($225\,nN$). At the small load one observes the nearly uniform broadening of diffraction spots in radial direction. In both cases the broadening consist of two components: radial and angular ones. The first originates from strains when interplane atomic distance increases near to the outer nanowire edge or decreases near to the inner edge. The second case, angular broadening is the direct effect of nanowire bending, when the atomic planes are inclined to each other. The effect of angular broadening is more pronounced at higher loads producing measurable angular spreading of spots.

Bibliography

[1] *Dortmunder Datenbank Online,* `http://www.ddbst.com`. (Cited on the page 45)

[2] *Learn to use TEM by John Rodenburg,* `http://www.rodenburg.org`. (Cited on the page 12)

[3] *MicroBlock 3-Axis Positioner (MBT602) Catalog Page. Available at* `http://www.thorlabs.de/catalogpages/v20/469.pdf`. (Cited on the page 37)

[4] `http://en.wikipedia.org`. (Cited on the page 25)

[5] `http://www.gnu.org/software/octave/`. (Cited on the page 64)

[6] `http://www.nanofactory.com`. (Cited on pages 10 and 47)

[7] *Tilt / Rotation Prism Stage (TRS-1) Datasheet. Available at* `http://www.opto-mechanics.co.uk/ downloads/TRS.pdf`. (Cited on the page 38)

[8] *Veeco SPM Training Notebook V3,* `https://depts.washington.edu/ntuf/facility/docs/Training_Notebook_v3.pdf`. (Cited on the page 25)

[9] M. Bordag, A. Ribayrol, G. Conache, L. E. Frödberg, S Gray, L. Samuelson, L. Montelius, and H. Petersson, *Shear Stress Measurements on InAs Nanowires by AFM Manipulation*, Small Journal **3** (2007), 1398–1401. (Cited on the page 26)

[10] B.R. Burg, V. Bianco, J. Schneider, and D. Poulikakos, *Electrokinetic framework of dielectrophoretic deposition devices*, Journal of Applied Physics **107** (2010). (Cited on the page 44)

[11] P. Caroff, K.A. Dick, J. Johansson, M.E. Messing, K. Deppert, and L. Samuelson, *Controlled polytypic and twin-plane superlattices in III-V nanowires*, Nature Nanotechnology **4** (2008), 50–55. (Cited on pages 32 and 79)

[12] P.M.F.J. Costa, P. Cachim, U.K. Gautam, Y. Bando, and D. Golberg, *The mechanical response of turbostratic carbon nanotubes filled with Ga-doped ZnS: I.Data processing for the extraction of the elastic modulus*, Nanotechnology **20** (2009). (Cited on pages 11 and 54)

[13] Q.-T. Do, K. Blekker, I. Regolin, W. Prost, and F.J. Tegude, *High Transconductance MISFET with a Single InAs Nanowire Channel*, IEEE Electron Device Letters **28** (2007), 682–684. (Cited on pages 9, 10, and 28)

[14] X. Duan, Y. Huang, Y. Cui, J. Wang, and C.M. Lieber, *Indium phosphide nanowires as building blocks for nanoscale electronic and optoelectronic devices*, Nature **409** (2001), 66–69. (Cited on the page 9)

[15] J.W. Edington, *Practical electron microscopy in materials science*, N.V. Philips' Gloeilampenfabrieken, Eindhoven, 1976. (Cited on pages 16, 74, and 75)

[16] H.D. Espinosa, Y. Zhu, and N. Moldovan, *Design and Operation of a MEMS-Based Material Testing System for Nanomechanical Characterisation*, Journal of Microelectromechanical Systems **16** (2007), 1219–1231. (Cited on the page 9)

[17] V. Germain, Jing Li, D. Ingert, Z.L. Wang, and M.P. Pileni, *Stacking faults in formation of silver nanodisks*, The Journal of Physical Chemistry B **107** (2003), 8717–8720. (Cited on the page 90)

[18] N.G. Green, A. Ramos, and H. Morgan, *AC electrokinetics: a survey of submicrometre particle dynamics*, Journal Physics D: Applied Physics **33** (2000), 632–641. (Cited on the page 44)

[19] Y. Huang, X. Duan, Y. Cui, L.J. Lauhon, K.-H. Kim, and C.M. Lieber, *Logic Gates and Computation from Assembled Nanowire Building Blocks*, Science **294** (2001), 1313–1317. (Cited on the page 9)

[20] R. Jin, Y.W. Cao, C.A. Mirkin, K.L. Kelly, G.C. Schatz, and J.G. Zheng, *Photoinduced Conversion of Silver Nanospheres to Nanoprisms*, Science **294** (2001), 1901–1903. (Cited on the page 90)

[21] M. Johansson, *AFM Sensors Datasheet. Nanofactory Instruments AB*, (2007). (Cited on the page 50)

[22] Thomas B. Jones, *Electromechanics of Particles*, Cambridge University Press, 1995. (Cited on pages 34, 35, and 36)

[23] M. Koguchi, H. Kakibayashi, M. Yazawa, K. Hiruma, and T. Katsuyama, *Crystal Structure Change of GaAs and InAs Whiskers from Zinc-Blende to Wurtzite Type*, Japan Journal of Applied Physics **31** (1992), 2061–2065. (Cited on pages 31 and 32)

[24] M. Lexholm, I. Karlsson, F. Boxberg, and D. Hessman, *Optical determination of Young's modulus of InAs nanowires*, Applied Physics Letters **95** (2009). (Cited on pages 11 and 78)

[25] X. Li, H. Gao, C.J. Murphy, and K.K. Caswell, *Nanoindentation of Silver Nanowires*, NanoLetters **3** (2003), 1495–1498. (Cited on the page 10)

[26] Zi-An Li, Ch. Möller, V. Migunov, M. Spasova, M. Farle, A. Lysov, C. Gutsche, I. Regolin, W. Prost, F.J. Tegude, and P. Ercius, *Dependence of the planar-defect characteristics and cross-sections in InAs nanowires*, (2010). (Cited on pages 11, 28, 29, 30, 32, and 84)

[27] V. Migunov, Z.-A. Li, Ch. Möller, M. Spasova, A. Lysov, I. Regolin, W. Prost, F.J. Tegude, and M. Farle, *Young's modulus of InAs nanowires*, (2011). (Cited on pages 10, 11, 26, 27, 78, 79, 80, and 93)

[28] A. Nafari, D. Karlen, C. Rusu, K. Svensson, H. Olin, and P. Enoksson, *MEMS Sensor for In Situ TEM Atomic Force Microscopy*, Journal of microelectromechanical systems **17** (2008), 328–333. (Cited on pages 10, 48, 49, 50, and 54)

[29] A. Ohtake, J. Nakamura, K. Kimura, and T. Yao, *Wurtzite-zinc-blende polytypism in ZnSe on GaAs(111)A*, Physical Review B **63** (2001). (Cited on pages 31 and 32)

[30] A. Ramos, N.G. Green, and A. Castellanos, *AC electrokinetics: a review of forces in microelectrode structures*, Journal Physics D: Applied Physics **31** (1998), 2338–2353. (Cited on the page 44)

[31] S. Raychaudhuri, S.A. Dayeh, D. Wang, and E.T. Yu, *Precise Semiconductor Nanowire Placement Through Dielectrophoresis*, Nano Letters **9** (2009), 2260–2266. (Cited on pages 44 and 45)

[32] S. Roy and Z. Gao, *Nanostructure-based electrical biosensors*, Nano Today **4** (2009), 318–334. (Cited on the page 9)

[33] R. Wiesendanger, *Scanning Probe Microscopy and Spectroscopy. methods and Applications*, Cambridge University Press, 1994. (Cited on pages 20, 23, and 25)

[34] M. Willander, Q. Zhao, and O. Nur, *Zinc oxide nanostructures at the forefront of new white light-emitting technology*, SPIE Newsroom (2007). (Cited on the page 29)

[35] D.B. Williams and C.B. Carter, *Transmission Electron Microscopy*, Plenum Press, New York, 1996. (Cited on pages 12, 13, 14, 16, and 17)

[36] R. Yan, D. Gargas, and P. Yang, *Nanowire photonics*, Nature Photonics **3** (2009), 569–576. (Cited on the page 9)

[37] Y. Zhu, C. Ke, and H.D. Espinosa, *Experimetal Techniques for the Mechanical Characterisation of One-Dimensional Nanostructures*, Experimental Mechanics **47** (2007), 7–24. (Cited on pages 9 and 10)

Appendix

Two examples of the AFM *in situ* in TEM measurements on InAs nanowires are presented as multimedia appendix on attached compact disc. Examples shows video demonstrations of load/unload tests, as well as corresponding force-displacement plots. THe first test (`M7-demonstration.avi`) is performed using nanowire M7, whereas the second test (`M6-demonstration.avi`) corresponds to nanowire M6. Detailed information about samples M7 and M6 can be found in sections 3.4.1 and 3.4.4, respectively. Please take into account that video demonstrations are two times slower than real time measurement.

Acknowledgements

I am very appreciated to persons, who helped me during my work. I am thankful for the supervising to Dr. Marina Spasova and for fruitful discussions to Vadim Migunov, Prof. Michael Farle and Dr. Zi-An Li. I would like to thank Horst Zähres for valuable discussions and great technical support. I thank Dr. Detlef Spoddig, Christian Wirtz and Dr. Miguel Comesaña-Hermo for the help by sample preparation. Andrey Lysov and the group of Prof. Franz-Josef Tegude are acknowledged for the synthesis of nanowires. And I thank my wife, Kateryna, who was carrying me along during this work.